DESIGN, FABRICATION, AND CHARACTERIZATION OF 850 nm VERTICAL-CAVITY SURFACE-EMITTING LASERS

By

GERARD DANG

A DISSERTATION PRESENTED TO THE GRADUATE SCHOOL
OF THE UNIVERSITY OF FLORIDA IN PARTIAL FULFILLMENT
OF THE REQUIREMENTS FOR THE DEGREE OF
DOCTOR OF PHILOSOPHY

UNIVERSITY OF FLORIDA

2001

ACKNOWLEDGEMENTS

Chu and Moncef Tayahi, with whom I was lucky to have met during my internship. George took many of the beautiful SEMs in this dissertation. Moncef helped with the large-signal analysis of the vertical-cavity surface-emitting lasers.

I would like to thank the members of my supervisory committee for their role in evaluating me. They are Dr. Fan Ren, Dr. Tim Anderson, Dr. Stephen Pearton, Dr. Cammy Abernathy, and Dr. Fred Sharifi.

I would like to thank everyone that has given me emotional support during my years in graduate school. In particular, my family, who has given me constant support and Dena Wrigley, who has given me unyielding encouragement and friendship.

TABLE OF CONTENTS

Abstract of Dissertation Presented to the Graduate School
of the University of Florida in Partial Fulfillment of the
Requirements for the Degree of Doctor of Philosophy

DESIGN, FABRICATION, AND CHARACTERIZATION OF 850 nm VERTICAL-
CAVITY SURFACE-EMITTING LASERS

By

Gerard Dang

December 2001

Chair: Professor Fan Ren
Major Department: Chemical Engineering

This dissertation covers details behind the design, fabrication, and
characterization of 850 nm vertical-cavity surface emitting lasers (VCSELs). The
lasers of this work have unique features that have been gradually implemented into
the VCSEL devices for high performance operation. The lasers use a shallow-
implant for forming the aperture. The bottom mirror is an AlAs/AlGaAs
semiconductor-based distributed bragg reflector (DBR) and the top light-output
mirror is an SiO_2/TiO_2 dielectric-based DBR. Intra-cavity contacts are formed on the
lasers, making them amenable for flip-chip bonding to integrated circuits. A step-by-
step treatment is given for the fabrication of the devices including how to achieve
these special features.

Complete device characterization was performed including electrical, optical,
and temperature dependence measurements were performed. Results from light-

current-voltage (LIV) measurements, optical spectra, temperature dependence measurements, and small and large-signal analysis (10 Gb/s operation was achieved) are presented and an analysis of the results is given. Some of the results from the electrical characterization of the devices were used to create a model for calculating the device series resistance. Results from the device series calculations closely agree with values obtained from experiment. The device series resistance model was used in part for a finite-difference approach in estimating the temperature profile in an operating VCSEL, because a portion of the heat generation in VCSELs is due to Joule resistive heating in the layers of the semiconductor. Good agreement between experimental and theoretical results was obtained.

Various computer simulations were performed in the design of the lasers and for predicting the performance of the lasers. Stopping and Range of Ions in Matter (SRIM) software was used to simulate the ion implantation steps of the VCSEL fabrication process that includes forming the aperture of the lasers and for capacitance reduction in the lasers. TFCalc was used to simulate the reflectivity of the high-reflectivity distributed bragg reflectors (DBRs) which are an important part of the VCSELs. TFCalc was also used, as well as SimWindows software, to calculate the electric field intensity wave in the device for verifying the high finesse of the optical cavity.

CHAPTER 1
INTRODUCTION

1.1 Historical Background

Vertical-cavity surface-emitting lasers (VCSELs) were at one time considered nothing more than laboratory device novelties. This attitude towards these devices in academia and in industry has changed largely due to the improvements in device performance, and the benefits of using VCSELs that have been realized. The device performance of the VCSEL has come a long way from the first reported surface-emitting laser in 1977, a GaInAsP/InP laser that was pulse-operated at 77 K.[1] From pulse-operated to continuous-wave operation of the present day devices, the standards on VCSEL device performance has increased. Device performance since 1977 has improved so much that it is almost expected that the devices have sub-milliampere threshold currents and a few milliwatts of output power.

Prior to the first demonstration of the VCSEL, researchers explored other methods of obtaining surface emission. Rather than using a vertical cavity, device designs that were based very close to edge-emitting laser technology directed the beam so that surface emission could be achieved.[2] It was soon realized that the cost benefits of having a surface emitting laser was diminished with these types of designs.

Researchers early on in the development of the VCSEL realized the important advantages that these devices could have. All of these advantages are in comparison to edge-emitting lasers since they were and still are in most applications the dominant diode laser being used. Namely:[2]

1) The laser device is fabricated by a fully monolithic structure.

2) A densely packed two-dimensional laser array could be fabricated.

3) The initial probe test could be performed before separation into chips.

4) Dynamic single longitudinal mode operation is expected because of its large mode spacing (=100-200 Å).

5) It is possible to vertically stack multithin-film functional optical devices on to the surface emitting laser.

6) A narrow circular beam is achievable.

The authors gave very good insight on the benefits of the VCSELs at the time, but since then even more benefits of using these devices have emerged. For example, VCSELs have been shown to have very high direct-modulation rates, can be processed so that they can easily be integrated into logic circuits, and have exhibited low operating powers.

During the early years of research on VCSELs, very high threshold currents were being reported. The gain region of a vertical cavity is much smaller in volume than that for an in-plane cavity of an edge-emitter. Critics of the developing VCSEL technology did not foresee a way of overcoming this, and did not give it the credibility for being a displacing technology for edge-emitters. Researchers learned that by using very high-reflectivity mirrors, the device performance of the VCSEL greatly improved and placed it on a competitive landscape with edge-emitters. Early

structures used alloy mirrors in the VCSEL with reflectivities of 80% and lower.[1] Present state of the art VCSELs use multi-layer distributed bragg reflectors that can obtain >95% reflectivity. The higher reflectivity increases the gain per photon created in the laser by preserving the generated photons inside the cavity, and thus reducing the threshold current of the VCSELs.

Advances in improvement of the current confinement in the VCSELs also helped in advancing reduction in the threshold current. Some early designs for current confinement used etched air-posts, mesas buried with polyimide, and buried heterostructures, which use an epitaxial regrowth step. Present state of the art 850 nm devices use an ion implantation or selective oxidation step to form the current confining aperture.

Methods in the growth of the VCSEL epitaxial structure also underwent refinement since its inception. The early device structures were grown using liquid phase epitaxy (LPE), which produces semiconductor material with poor surface morphology. The use of metal-organic vapor deposition to grow the epitaxial structure for the VCSEL was first performed in 1987.[3] The improvement of using a precise growth method with excellent uniformity and thickness control was recognized, and the majority, if not all, of the VCSEL structures grown presently are performed using high precision growth methods such as MOCVD, MBE, and GS-MBE.

In 1989, the first reported current-injected 850 nm VCSEL operating at room temperature was reported.[4] This device incorporated special features at the time, such as a short optical cavity for the time (~5.5 μm) and dielectric-based high reflectivity

mirrors (SiO$_2$/TiO$_2$). Single longitudinal mode operation over a range of more than 50 K was observed. The threshold current and maximum output power were a respectable 30 mA and 1.6 mW. The demonstration of an electrically pumped VCSEL with single-mode characteristics really generated attention towards these devices as a viable and practical laser. Following this report, the research on VCSELs grew tremendously. Device performance and innovations increased rapidly thereafter.

Although many of the early VCSELs were designed for long-wavelength emission, to date the majority of the work and the best results reported for VCSELs are for the short wavelength 850 nm VCSEL. These devices are based on the Al$_x$Ga$_{1-x}$As/GaAs materials system and benefited from the mature research foundation that was established for electronic devices based on this material system. These factors and additional advances in VCSEL processing technology helped to produce devices that were manufacturable. Presently, there are numerous companies that manufacture 850 nm VCSELs and more recently long-wavelength 1310 nm VCSELs.

1.2 Companies Manufacturing VCSELs

1.2.1 850 nm VCSELs

Emcore Corporation, originally an MOCVD equipment company for compound semiconductor crystal growth, is manufacturing VCSELs for telecommunications applications. The company included a foray into manufacturing VCSELs as part of their financial growth strategy in hopes of larger profit margins.

They gained their VCSEL expertise with their acquisition of MODE (Micro-Optical Devices), a company started by VCSEL researchers from Sandia National Laboratories. Their VCSEL technology is based on VCSELs with oxide apertures. Their current VCSEL products include 1 x 4 and 1 x 12 arrays operating at 2.5 Gb/s and 3.125 Gb/s, respectively. They also currently offer discrete devices operating up to 10 Gb/s. They have been in a three-year agreement with Agilent Technologies since November 2000 to supply parallel optical transceivers using VCSELs. Agilent is using these transceivers to build terabit-scale networking equipment.

In 1996, Honeywell Sensing and Control, a division of Honeywell International Incorporated, became the first company to manufacture VCSELs. Honeywell International Incorporated manufactures a wide range of products for the aerospace, automotive, and power generation industries to name a few. They presently claim to be the largest supplier of VCSEL devices. Their VCSELs are being used in applications that include transmitters for fiber optic links, encoders, laser printing, bar code scanning, and optical storage. Their product offering includes a wide variety of VCSEL products including high-speed arrays and discrete devices.

Gore Photonics is a division of W. L. Gore and Associates. W. L. Gore and Associates have 1 billion dollars in global sales on a variety of products that include fabrics, medical and health care equipment, and electronics. Like Emcore Corporation, they realized the potential of larger profit margins with selling VCSEL products. They bought out Optical Concept, a startup formed by researchers from the University of California, Santa Barbara, that included Dr. Larry Coldren, a pioneer in VCSEL technology and development. Gore currently is sampling parallel optical

interconnects based on its 850 nm VCSEL technology. The modules target an application in 10 Gb/s serial links and have been demonstrated successfully as a very-short-reach parallel optical interface for transmission over distances up to 300 m.

E$_2$O Communications, Incorporated was founded in 1998 and is manufacturing optical tranceivers using its own 850 nm VCSELs. Its tranceivers are capable of operating up to 2.5 Gb/s. It has teamed with 3M to manufacture some of their tranceivers. E$_2$O is using 3M's connector technology on their transceivers. It has also announced progress on the development of 1.3 μm VCSELs.

AXT, Incoporated was established with the purpose of manufacturing high performance III-V compound semiconductor substrates using its proprietary technology. AXT also realized the presence of a lucrative market in optoelectronic devices and has expanded its own business to include growing epiwafers for optoelectronic devices, as well as fabrication of optoelectronic devices. AXT's epiwafer products include VCSEL structures, and the decision to fabricate VCSELs in-house from its own material is obvious considering the value added to the epiwafers when devices are processed from them. Its current product offering at the 850 nm wavelength includes discrete as well as arrays of VCSEL devices using both oxidation and implant technologies for current confinement.

1.2.2 1310 nm VCSELs

Long-wavelength VCSELs have benefited tremendously from the technological developments that occurred from research on 850 nm VCSELs. Although work on long-wavelength VCSELs began much earlier than work on 850 nm VCSELs, advances in VCSEL technology to date have been primarily for 850 nm

VCSELs. Long-wavelength VCSEL development has had challenges such as overcoming device overheating, due to the lower thermal conductivities of the materials used, and the realization of suitable materials for high reflectivity mirrors. VCSELs emitting at 1310 nm are desirable for long-haul optical fiber communication, which requires signal transmission over a distance of at least 3 km.

Cielo, Incorporated has benefited from a heavy collaboration with Sandia National Laboratories and the VCSEL technology developed there. The company recently showcased a 1310 nm VCSEL at the National Fiber Optics Engineers Conference (NFOEC) in Baltimore that ran at 10 Gb/s over 10 km of optical fiber. Its current product offering includes 8 and 12 channel parallel array modules with aggregate speeds up to 30 Gb/s and 850 nm and 1310 nm transponders that operate up to data rates of 10 Gb/s.

Nova Crystals, Incorporated has announced 1310 nm VCSEL products. It is conjectured that the company performs its epitaxial growth using a compliant substrate to overcome stresses and strains that come about from growing InGaAs on GaAs substrates, one approach with limited success for realizing 1310 nm wavelength emission. The company has kept under wraps the details of the compliant substrates, but published papers from the company's founders shed some light on the approach it is using. The company's current product offering includes 1310 nm VCSEL chips compatible with OC-48 (2.5 Gb/s) and OC-192 (10 Gb/s) systems.

1.3 Market Projections

The VCSEL transceiver market was approximately $600 million in 1999. ElectroniCast Corporation projects this market to increase to more than $2 billion dollars by 2004. Electronicast is an independent marketing research firm specializing in forecasting technology and global market trends in fiber optics, network communications and advanced photonics. The forecast includes 850 nm and 1310 nm VCSELs. The forecast does not include VCSELs emitting at 1550 nm because these will take longer to become commercialized. In any event 1550 nm VCSELs will make an impact in wavelength division multiplexing, a separate market from VCSEL transceivers. As of 1999, the main applications for VCSEL transceivers were fibre channel, Ethernet, and intra-system links as shown in Figure 1-1. As can be seen from Figure 1-2, the intrasystem link application is projected to grow the fastest between 1999 and 2004. The market for VCSEL transceivers used in intra-system links is expected to grow almost 17 fold from 1999 to 2004 and almost 130 fold by 2009, as can be seen from Figure 1-3. This fast growth is expected to occur because more expensive 1310 nm distributed feedback lasers are being used for connections among routers, hubs, and switches in the central office and with the cost advantage of manufacturing VCSELs, they should take over this space. Cielo Communications, Inc. has already begun sampling its 1310 nm VCSELs and a few other manufacturers have announced their plans to manufacture 1310 nm VCSELs soon. We also see new markets emerging for VCSEL transceivers by 2004. These emerging markets are projected to continue their growth into 2009.
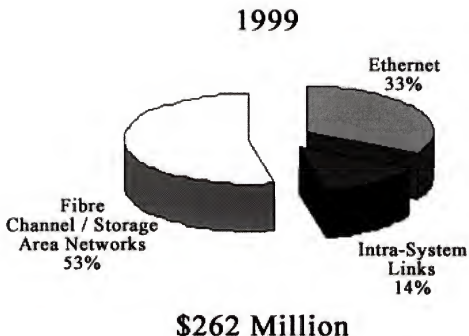
1999

Figure 1-1 The main applications, graphed by market share, for VCSEL tranceivers in 1999.

2004

$3.4 Billion
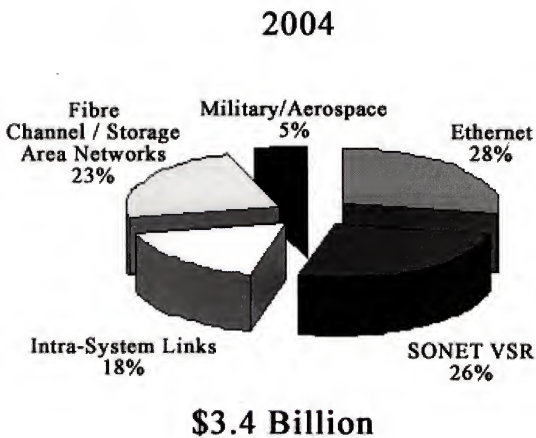
Figure 1-2 The projected main applications, graphed by market share, for VCSEL tranceivers in 2004.

2009

$14.1 Billion
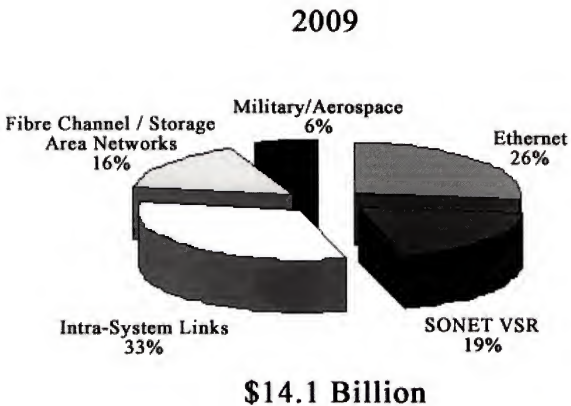
Figure 1-3 The projected main applications, graphed by market share, for VCSEL tranceivers in 2004.

1.4 Device Applications

The vertical cavity surface-emitting laser potentially has many desirable applications. Because of the VCSEL's unique properties and design, it should provide a low cost solution, rivaling edge-emitting lasers, for high-speed and high power applications.

The VCSEL is a diode laser, a category which is presently dominated by edge-emitting lasers in just about all major applications using a semiconductor laser, including applications in telecommunications, optical storage, and image recording. In order for VCSELs to displace edge-emitting lasers in these applications, the VCSEL has to be able to have sufficient operating performance and cost less to manufacture. The one area that VCSELs have begun to make inroads is at the 850 nm wavelength. These VCSELs have recently become commercialized and are being manufactured by a host of companies as covered in Section 1.2. The special design of the VCSEL gives it potential for becoming the diode laser of choice for many applications in which edge-emitting lasers are presently used as well as for new applications where using an edge-emitting laser would not suffice.

1.4.1 VCSEL Array Applications

From a cost standpoint, the VCSEL has many manufacturing advantages. The devices can be fabricated in a dense fashion similar to the fabrication of standard electronic devices. This is possible because they are surface emitting, and it follows that two dimensional arrays of VCSELs can be fabricated from a wafer. Edge-emitters require a cleaving step for creating the reflective surfaces necessary for the devices to lase. These devices require cleaves along facets normal to the direction of

lasing, and thus one dimensional rows are only possible without any special additional complicated processing or packaging to form a two dimensional array.

With the advantage of being able to process two-dimensional arrays of VCSELs, this configuration is attractive for parallel signal transmission applications. With the high direct modulation rates of VCSELs, inherent to its structure by virtue of their smaller active volumes, the number of bits that can be transmitted using these devices are higher than for edge emitting lasers.

Parallel processing would require an array of VCSELs coupled to an optical fiber bunch. This configuration is attractive because of the aggregate data transmission speeds that can be obtained. A 1 x 4 array of 2.5 Gb/s VCSELs can transmit an aggregate data transmission rate of 10 Gb/s.

Because of the VCSEL's design, it can more easily be integrated with other devices and into integrated circuits. By altering the reflectivities of the VCSEL's two mirrors, the devices can be altered to emit light from the surface or from the backside of the device. Backside emission is a necessary feature for flip-chip bonded VCSELs. Flip-chip bonding requires that the VCSELs have coplanar contacts. The device is "flipped" and bonded using deposited metal posts on the device contacts. The usefulness of this capability is made more intriguing if individually addressable VCSEL device arrays were flip-chip bonded to logic-controlled integrated circuits.

Krishnamoorthy et al. have demonstrated the feasibility and practicality of fabricating VCSEL arrays.[5] Their work focuses on flip-chip bonding VCSEL arrays to CMOS VLSI (complementary metal oxide semiconductor very-large-scale integration) circuits. This takes advantage of the VCSEL's capability of being flip-

chip bonded and integrating it into existing silicon CMOS VLSI circuit technology. Performing this with edge-emitting lasers would be a technological challenge and the cost for manufacturing such systems would be tremendous.

1.4.2 Extended Short Area Network Transmission with 850 nm VCSELs

VCSELs lasing at 850 nm were initially envisioned to be used in short area networks with maximum transmission distances of 300 m or less, but recent announcements from Lucent Technologies dispelled this notion. Lucent announced that using its LazrSPEED™ multimode fiber, signal transmission using an 850 nm VCSEL over 1.6 km was obtained. The bit error rate was less than one error in a trillion bits. With this breakthrough, the 850 nm based short-area network (SAN) becomes more attractive with the reach of the network greatly expanded. As the demand for bandwidth in the home and office increases, and the present data rates of 10 Mb/s transmission over copper lines become insufficient, the short area optical network using the 850 nm VCSEL is poised to meet these needs for migration to 10 Gb/s rates.

1.4.3 Additional Desirable Features of VCSELs

In addition to the desirable features of VCSELs that have made them so attractive for the applications already mentioned, the following details two more.

The ability to perform on-wafer testing of VCSEL devices will speed up the development of better performing VCSELs in manufacturing as well as in the research lab. Processing can be monitored and problems pin-pointed prior to any destructive cleaving that can prevent any further useful processing, as is the case for

edge-emitters. Further details on the convenience of on-wafer testing of VCSELs are covered in Chapter 4.

The output beam characteristics of a diode laser will depend on the geometry of the active region and any optical and electrical confinement in the device. For the VCSEL, the output beam will be dictated by the design of the VCSEL's current aperture, which is normally designed to be circular, while for edge-emitting lasers, an elliptical shape is obtained due to the thin active region feature and the larger width of edge-emitting lasers. A circular beam is desirable because the efficiency of coupling the beam to the circular input of optical fiber is higher than coupling an elliptical beam to it.

CHAPTER 2
DESIGN

2.1 Simulation Software

2.1.1 SimWindows

SimWindows is semiconductor device simulation software that can be used to determine useful information on VCSELs. The software simulates various characteristics of the devices with analysis in one dimension. The software has material parameters for the $Al_xGa_{1-x}As$ system, and so is suitable for simulating the VCSELs of this work without having to input additional material parameters into the program.

The structure of the cavity is input into a SimWindows device file using SimWindows' syntax. The required layer information necessary for SimWindows to perform VCSEL analysis is thickness, material type, and doping concentration. The positions of the active layers in the cavity have to be specified as well. SimWindows models the device structures as being cylindrical in shape with contacts on the ends. The actual VCSELs of this work are not entirely cylindrical in shape because of the test pad extensions on the devices. SimWindows analysis supports only mirrors of the VCSEL at discrete positions in the system and, for analysis of this work, are set to be at the ends of the cylindrical system, at the same positions as the device contacts in the SimWindows device structure. The VCSELs being analyzed use DBRs which

have an effective penetration depth of the optical mode and that add to the cavity length of the device. Although there will be some error introduced in the simulation of the device operation because the mirrors are specified to be at discrete positions and because the devices not entirely cylindrical in shape, SimWindows will nevertheless provide a good qualitative analysis.

Figure 2-1 shows the simple energy band diagram for the VCSEL cavity using SimWindows. This plot was created by connecting the bandgap energies of the materials. Figure 2-2 shows the band diagram for the VCSEL cavity at thermal equilibrium. SimWindows can also simulate the band diagram for an applied bias. Figures 2-3 to 2-6 show the band diagram at forward biases of 0.5-1.75 V. As can be seen from these figures, there is a quasi-fermi level separation for the conduction and valence bands as the device is biased. At the forward bias of 1.5 V, the quasi-fermi level for the conduction band is above the energy levels of the quantum wells. This indicates high injection of electrons into the active region. At 1.75 V, there is high injection of holes into the active region. This point marks very closely the point at which the VCSEL devices actually lase.

2.1.2 TF Calc

TF Calc is useful in the design of VCSELs. The software allows for the entry of multi-layer films and can simulate the reflectivity of distributed Bragg reflectors over a range of wavelengths. Inputting information on the layers into the software for both the top and bottom mirrors and the optical cavity, the software can also determine the cavity resonance for the structure. Refractive indices and dispersion
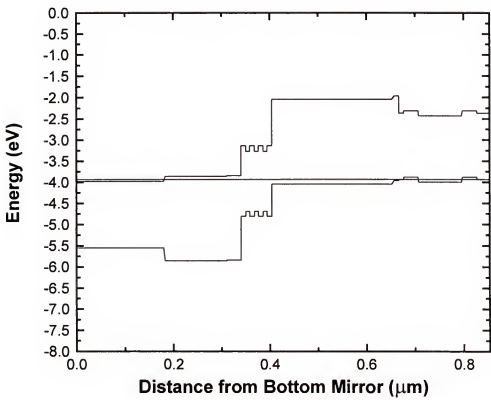
Figure 2-1 Simplified band diagram generated using SimWindows for the optical cavity of the VCSEL of this work.
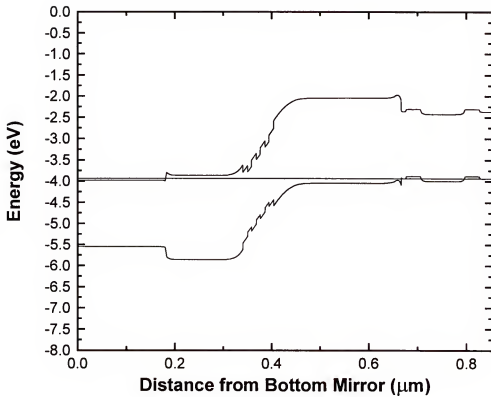
Figure 2-2 Band diagram generated using SimWindows for the optical cavity of the VCSEL of this work at thermal equilibrium.
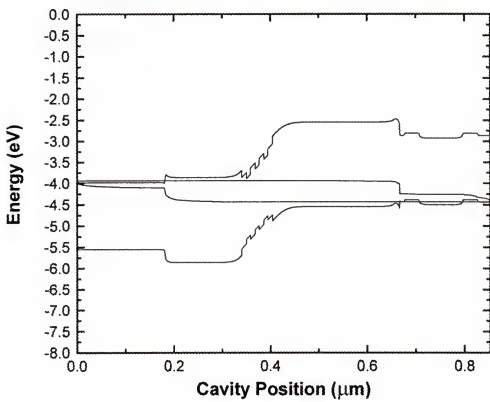
Figure 2-3 Band diagram generated using SimWindows for the optical cavity of the VCSEL of this work with a 0.5 V forward bias.
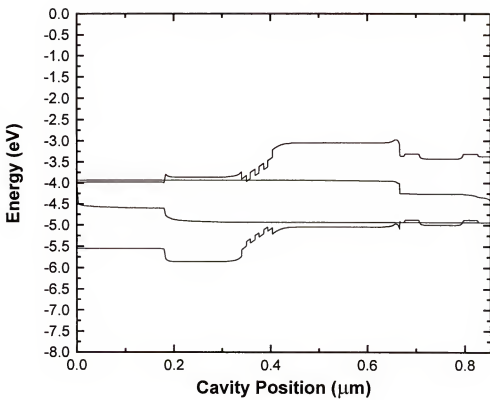
Figure 2-4 Band diagram generated using SimWindows for the optical cavity of the VCSEL of this work with a 1.0 V forward bias.
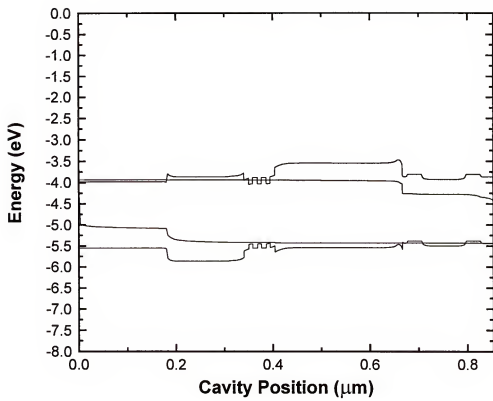
Figure 2-5 Band diagram generated using SimWindows for the optical cavity of the VCSEL of this work with a 1.5 V forward bias.
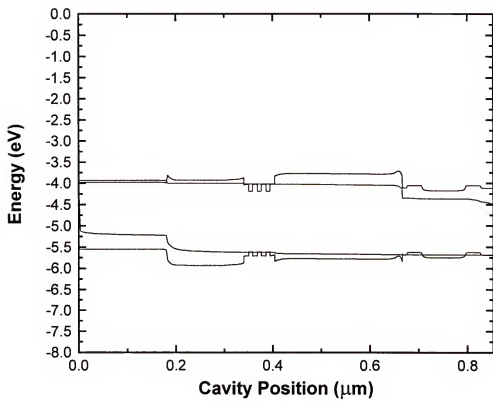
Figure 2-6 Band diagram generated using SimWindows for the optical cavity of the VCSEL of this work with a 1.75 V forward bias.

data are required for the materials being used in the simulations. Optical properties of the materials used for the VCSELs of this work were obtained from outside references.[6] The software also performs electric field intensity calculations, similar to the standing wave analysis performed by SimWindows, which aid in designing a high-finesse optical cavity that minimizes absorption.

2.2 Cavity Design

The simplest and first optical cavities using coplanar reflectors were demonstrated by Fabry and Perot and fittingly were named Fabry-Perot cavities. The two reported on this in 1899.[7] For their experiments, the cavity lengths were much greater than the wavelength of light used. It has since been determined that when using cavity lengths close to the emission wavelength of the laser, or what are called micro-cavities, an enhancement in the optical confinement factor of the cavity in the longitudinal direction is obtained. This improves the operating characteristics of the VCSEL, such as reducing the threshold current. For this reason, VCSELs are designed to take advantage of the optical confinement enhancement and normally have micro-cavities. This is the case for the VCSEL cavity of this work.

2.2.1 Epitaxial Structure of this Work

The thickness of the physical optical cavity between the top and bottom distributed bragg reflectors is ~850 nm. Figure 2-7 shows the epitaxial layer structure of this work. The layers were grown using low-pressure metalorganic chemical vapor deposition on semi-insulating GaAs substrates. The precursors used were arsine,
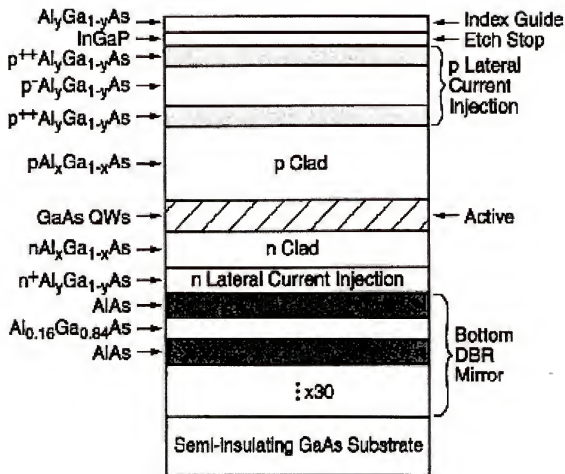
Figure 2-7 Schematic of the epitaxial structure for the VCSEL of this work.

phosphine, trimethylgallium, trimethlindium, and trimethylaluminum. The dopant precursors used for p- and n-type doping were carbon tetrabromide and disilane, respectively. The structure was grown at 760 °C except for the p-lateral current injection layers, the InGaP etch stop, and the index guide layer. A reduced temperature was used for these layers to enhance the carbon incorporation into these layers and for achieving the high doping concentration necessary for the p-lateral current injection layers. Secondary ion mass spectroscopy analysis was performed to confirm the doping concentrations levels and to confirm that low oxygen concentrations were present in the layers grown at the lower temperatures. The presence of oxygen can create deep level carrier traps and degrade the carrier concentrations in the doped semiconductor layers.

The VCSEL cavity essentially has a p-i-n structure where the intrinsic region is the active region of the laser. The active region consists of several GaAs quantum wells with $Al_{0.2}Ga_{0.8}As$ barriers. The bottom mirror is semiconductor-based and is grown in a single run prior to the growth of the cavity layers of the VCSEL.

It is important to note the lateral current injection layers incorporated into this structure. Lateral current injection has been investigated previously on earlier work with VCSELs.[8,9] On both the p- and n-layers of the cavity, the layers were engineered to efficiently inject current uniformly into the aperture region of the VCSELs. Without the lateral current injection layers, current would inefficiently crowd along the periphery of the VCSEL aperture and preferentially pump higher order modes. Lateral current injection is achieved by using a contrast in the doping levels of semiconductor layers so that current is initially directed with less resistance

laterally and then vertically through the aperture of the device. In the case of the n-side of the epitaxial structure, contacts are formed to a highly doped n-type layer. On top of this layer going towards the aperture, a lower doped layer prevents the carriers from flowing vertically, and instead spread along the more heavily doped layer and then more uniformly in the vertical direction as it conducts through the aperture. The same type of idea is use on the p-side as well, but a stack of two high and low doped pairs are used to enhance lateral current injection.

The p-side is thicker than the n-side of the VCSEL cavity so that there is enough material for formation of the aperture using ion implantation with minimal damage to the active region. Excessive damage to the active region of the device can lead to reduced radiative recombination efficiency and long-term reliability problems.

The two top outermost layers of the cavity are for formation of the index guide. These layers are a thin InGaP layer followed by a thin $Al_yGa_{1-y}As$ layer. The index guide is formed from the $Al_yGa_{1-y}As$ layer using a highly selective wet etch solution with the InGaP layer acting as the etch stop, so that precise thickness of the index guide can be achieved.

2.2.2 Standing Wave Analysis

Standing wave analysis is important for designing a VCSEL cavity that is low in losses and that is capable of resonating at the wavelength of interest. Because of the multilayer structure of the VCSEL cavity, the varying index of refractions that a mode encounters makes standing wave analysis complex. Typically, software simulation programs are used for performing standing wave analysis. For this work,

standing wave analysis was performed using SimWindows and TFCalc, with good agreement.

Figures 2-8 and 2-9 show the standing wave profile generated by SimWindows plotted against the refractive index and bandgap energy profiles. As can be seen from the plots, a maximum of the standing wave is positioned at the gain regions of the cavity. This enhances the gain in the laser emission of the devices. It is also desired for the nodes of the standing wave to be positioned at regions of high carrier concentration to minimize absorption losses.

The standing wave profile was also generated using TFCalc. The profile is shown in Figure 2-10. The profile obtained using TFCalc is in good agreement with the profile obtained using SimWindows.

2.3 Mirror Design

Due to the shorter gain length present in VCSELs, the gain per pass in the cavity of the devices can be one percent for an active region consisting of three properly positioned quantum wells.[10] In order for the device to have a good electrical power to optical power efficiency, high reflectivity mirrors are required. Typically, mirror reflectivities of greater than 99% are necessary for good device performance. The output mirror for this work, or the mirror in which light is desired to emit from, was designed to have a reflectivity of ~99.6%. Metal films can achieve maximum reflectivities of up to about 95%, and to realize these higher reflectivity mirrors required for VCSELs, distributed Bragg reflectors are used. A DBR is a reflector
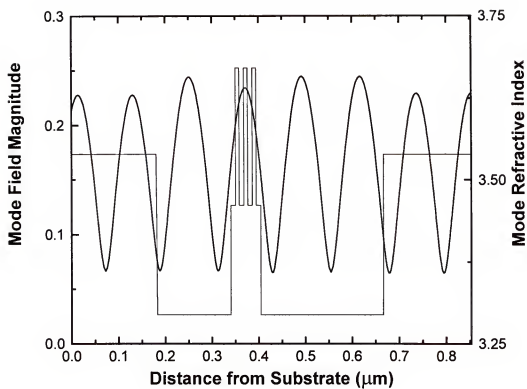
Figure 2-8 Standing wave in the optical cavity plotted against refractive index for the VCSEL of this work. Plot was generated using SimWindows.
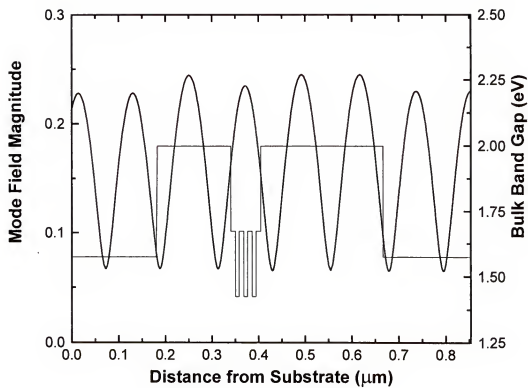
Figure 2-9 Standing wave in the optical cavity plotted against bulk bandgap energy for the VCSEL of this work. Plot was generated using SimWindows.
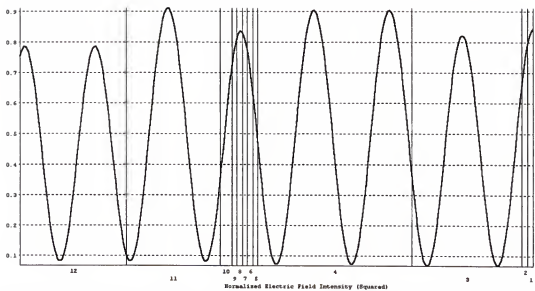
Figure 2-10 Standing wave in the optical cavity generated using TFCalc for the VCSEL of this work.

consisting of alternating layers of materials with different refractive indices. Figure 2-11 illustrates the periodic structure of the DBR. At the Bragg condition, these reflectors can achieve the requisite greater than 99% reflectivity. The reflector begins with the material with the lower refractive index and then the material with the higher refractive index. For optimal reflectivity, the thicknesses of these layers should be:

$$t = \lambda / 4n \qquad \text{Equation 1-1}$$

where n is the refractive index of the material and λ is the Bragg wavelength. This equation is valid for normal incidence of light on the reflector, as is the case in VCSELs with reflectors parallel to each other.

There are two models for quickly estimating the reflectivity of a DBR at the Bragg wavelength. The first is from M. Born and E. Wolf's seminal text:[11]

$$R = \left(\left[\frac{n_i - n_e \left(n_1 / n_2 \right)^{2N}}{n_i + n_e \left(n_1 / n_2 \right)^{2N}} \right] \right)^2 \qquad \text{Equation 1-2}$$

where n_1 and n_2 are the refractive indices of the two materials constituting the DBR layers at the Bragg wavelength, n_i is the refractive index of the incident medium, n_e is the refractive index of the exiting medium, and N is the number of periods. A period is one pair of the materials represented by the refractive indices n_1 and n_2.

Coldren et al. model the reflectivity of the DBR at the Bragg wavelength using the following relationship:[12]

$$R \approx \tanh\left(\frac{N \Delta n}{\bar{n}} \right) \qquad \text{Equation 1-3}$$

where the terms $\Delta n = n_2 - n_1$ and $\bar{n} = \frac{n_1 + n_2}{2}$, and the terms n_1, n_2, and N are the same as Born et al.'s model. The two models closely resemble one another. Both

Figure 2-11 Schematic of the periodic structure of a distributed Bragg reflector.

predict the increase in reflectivity when the ratio of n_1 to n_2 is increased or the number of periods is increased.

The width of the reflector stop band can also be estimated. The stop band is the high-reflectivity wavelength band of the reflector. The wavelength width of the stop band is given by:[13]

$$\Delta\lambda_{SB} = \frac{2\lambda\Delta n}{\pi n_{eff}}$$

Equation 1-4

where,

$$n_{eff} = 2\left(\frac{1}{n_1} + \frac{1}{n_2}\right)^{-1}$$

Equation 1-5

is the effective refractive index of the DBR.

There are two main categories for the types of distributed bragg reflectors used for VCSELs. They are semiconductor and dielectric based distributed bragg reflectors.

2.3.1 Semiconductor DBRs

Semiconductor-based DBRs normally require more pairs than dielectric based DBRs, due to the larger difference in refractive indices that are available with dielectric materials. Semiconductor based DBRs can require tens of periods to obtain reflectivities greater than 99%. Single epitaxy can be performed if the top and bottom mirror of the VCSEL are semiconductor DBRs. The requirements for choosing an appropriate pair of semiconductor materials for forming a DBR requires that alternating layers of the DBR can be grown, and that the rest of the epi-growth for the device can be performed with smooth morphology and low defects. For the 850 nm VCSEL, GaAs quantum wells are used, and if the epitaxial growth is to require one

run, the DBR materials would have to be compatible for growth with GaAs. For the VCSELs of this work, a 30 pair AlAs/Al$_{.16}$Ga$_{.84}$As DBR was used for the bottom mirror.

Semiconductor DBRs can be doped to support current conduction. These DBRs can create a large amount of series resistance though, due to the potential barriers from the alternating materials of differing bandgap. Engineering these DBRs to reduce this resistance has been a subject of intense research. Elaborate doping and compositional profiles have been engineered to optimize low-resistance current transport through the mirrors.[14,15,16,17,18] Doping the DBRs can also lead to additional free-carrier absorption losses, but this effect can be minimized if the semiconductor DBRs are designed so that the electric field is at a node where the doping is a maximum in the DBR.

2.3.2 Dielectric DBRs

Dielectric based DBRs are deposited at some point in the device fabrication sequence after the epitaxial growth has been performed. Dielectric DBRs cannot support current conduction for VCSEL operation, so intra-cavity contacts are required. Intra-cavity contacts are electrodes formed directly to layers of the optical cavity. Using intra-cavity contacts eliminate the need for designing elaborate doping and compositional profiles for low resistance semiconductor DBRs. Using intra-cavity contacts will require additional processing steps, though. Typically, the n- and p-contacts are coplanar, i.e. on the same side of the wafer. In order to form these contacts, layers have to be etched away to expose the n- and p-layers. Using intra-cavity contacts should result in higher speed devices, simply because the distance for

current transport between electrodes is shorter and have fewer potential barriers for conduction.

Dielectric DBRs in general require fewer periods than semiconductor DBRs. The dielectric materials used need to have a large difference in refractive index, Δn, if fewer pairs are desired. The stopband, or wavelength range of high reflectivity, for dielectric mirrors are also greater than for semiconductor DBRs due to the larger Δn. A wider stopband gives more flexibility in forming high reflectivity mirrors because of the DBR's sensitivity to thickness fluctuations of the DBR layers.

The use of dielectric DBRs eliminates the problems of losses associated with optical absorption in semiconductor mirrors. The problem of optical absorption in semiconductor DBRs is worse for p-type semiconductor DBRs, where optical absorption can be higher than n-type semiconductor DBRs. This is due to intraband absorption by electrons in the subbands of the valence band, i.e. heavy-hole band, light-hole band, and split-off band. Similar transitions can occur in n-type materials but are not normally observed. Because the p-type semiconductor DBR can introduce excessive optical absorption in the laser, it can be advantageous to use a dielectric DBR to minimize loss. The VCSELs of this work use a dielectric based DBR in place of a semiconductor based p-type DBR.

2.3.3 Mirrors of this Work

Figure 2-12 shows an Auger Spectroscopy depth profile plot for the dielectric TiO_2/SiO_2 DBR used as the top mirror for the VCSELs of this work. The DBR samples were prepared on blank GaAs substrates using the same deposition
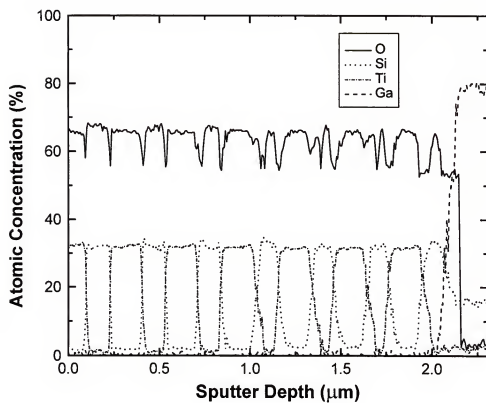
Figure 2-12 Auger depth profile of the top dielectric distributed bragg reflector of this work.

conditions as for fabricating the VCSEL devices. Prior to placing the sample in the Auger depth profiling analytical chamber, the sample was rinsed in acetone, followed by isopropyl alcohol, then dusted with dry air. The conditions used for the electron beam in this analysis were 3 keV and 0.5 c. An Ar^+ molecular beam at 3 keV and 3.2 μA was used for sputtering of the DBR material. The raster size was 2 mm x 2 mm and sample rotation was used. The area of analysis was at the sample axis of rotation. Secondary electron imaging was used to locate the axis of rotation. The angle of incidence for the molecular beam was 55° from the normal of the sample. The depth profile reveals degrading resolution deeper into the sample as the mirror layers are sputtered away. This is due to the dielectric material heating up. Heating is a common occurrence with dielectric materials because of their tendency to charge. The electron beam condition of 0.5 μA is a relatively low current and was chosen to reduce charging. Blistering of the sample due to heating was observed anyway, but acceptable resolution is obtained even at the deeper layers. Nevertheless, the profiling provides atomic concentration information on the DBR in the correct proportions for TiO_2 and SiO_2 and shows reasonable separation between the alternating layers. The sputter depth shown in Figure 2-12 is misleading because the sputtering rate is calibrated for the first layer of the DBR, and there was a difference in the sputtering rate of the SiO_2 and TiO_2 layers.

Figures 2-13 and 2-14 show the reflectivity simulations for the top and bottom distributed Bragg reflectors used in the VCSELs of this work. TFCalc was used to generate these plots. At 850 nm, the reflectivities are 99.6% and 99.9% for the top
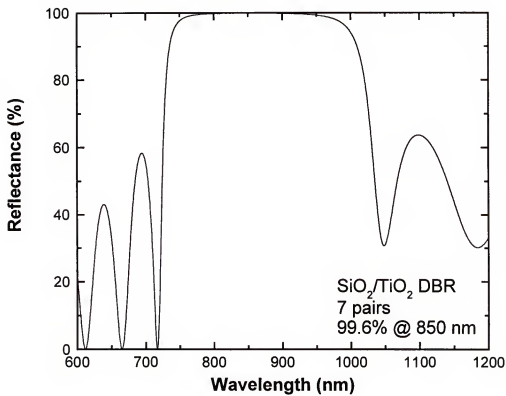
Figure 2-13 Reflectance spectrum for the top DBR used in the VCSEL of this work. Plot was generated using TFCalc.
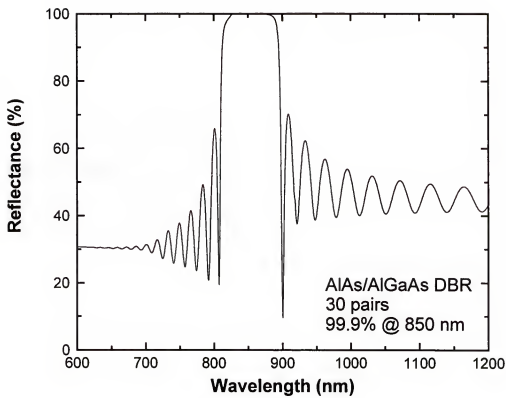
Figure 2-14 Reflectance spectrum for the bottom DBR used in the VCSEL of this work. Plot was generated using TFCalc.

and bottom DBRs respectively. The difference in the stopband widths for the top and bottom mirrors is apparent. As expected for the dielectric based top mirror, the stopband is markedly wider due to a larger difference between the refractive indices of the two materials of the DBR. The stopband widths are ~100nm and ~50 nm for the top and bottom DBRs respectively. Optical quarter-wave thickness layers for the DBR simulations were used to obtain the most optimal numbers.

Using TFCalc to simulate the reflectivity of the VCSEL structure including the cavity as well as the top and bottom mirror, the cavity resonance can be determined. As can be seen in Figure 2-16, the cavity resonance for the VCSELs of this work is ~850 nm. The cavity resonance determines the wavelength of the longitudinal mode at which the VCSEL lases.

2.4 Aperture Design

The VCSEL aperture is an important feature of the device. Its main purpose is to confine current for efficient carrier injection into the active region. There are presently two main approaches for forming the aperture in 850 nm VCSELs.

2.4.1 Oxide Apertured VCSELs

Oxide apertured VCSELs have gained tremendous acceptance from research and industry. Oxide apertures are generally formed by selectively oxidizing a high aluminum content $Al_xGa_{1-x}As$ epitaxial layer in the VCSEL cavity until the desired aperture size is obtained. Oxidation is typically performed in a steam environment at an elevated temperature. This requires a significant exercise in obtaining
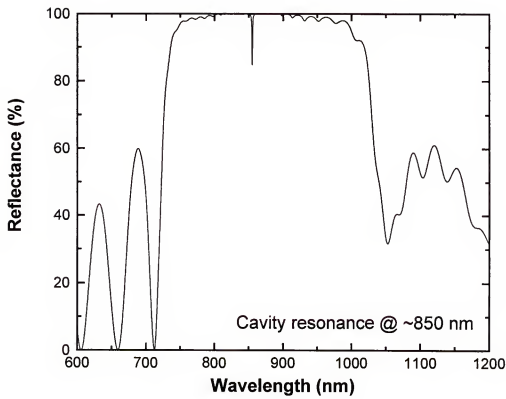
Figure 2-16 Reflectance spectrum for the VCSEL structure of this work. Plot was generated using TFCalc.

reproducible material quality and oxidation conditions because the oxidation rate is extremely sensitive to the aluminum percentage of $Al_xGa_{1-x}As$ material. For example, to illustrate the sensitivity of the $Al_xGa_{1-x}As$ wet-oxidation rate to material composition, orders of magnitude variation in oxidation rate was observed for $0.84 < x < 1$.[19]

The advantage of having an oxide aperture is that it provides a means for current and optical confinement in the VCSEL. The optical confinement that the oxide aperture provides can be used to obtain single-mode behavior of the light emission. The reported device performance on oxide-apertured VCSELs have shown excellent performance.[20,21,22]

2.4.2 Implant Apertured VCSELs

Ion implantation can be used to form the aperture in VCSELs for current confinement. Implantation creates regions of low-conductivity in the VCSEL and directs current into a small region of the active layers for high carrier injection. Ion-implantation simulation software such as Stopping and Range of Ions in Matter (SRIM) can be used to determine the energy and dose required for an acceptable implant. Photoresist is sufficient for blocking the implantation from areas where it is not wanted and typically is used as the implant mask. To prevent channeling in the sample, a 7° incline is used. Unlike the oxide aperture, the aperture formed by ion implantation does not provide useful optical confinement. Further details on the use of SRIM and on the formation of the aperture using ion-implantation for this work is given in Chapter 3.

CHAPTER 3
FABRICATION AND PROCESSING

The fabrication of the short-wavelength 850 nm VCSEL requires numerous steps to incorporate the special features of the device. This chapter discusses some related studies on VCSEL fabrication and processing and lists the steps for fabricating the VCSELs of this work.

Many of the steps in processing and fabrication of VCSELs require the use of photolithography. Photolithography is performed using various types of photoresist, depending on what is required. Positive and negative tone photoresists of varying post-spin thickness are used in the fabrication process. Mask alignment and photoresist exposure is performed using a Karl Suss MJB3 contact mask aligner. The idea behind photolithography is to "print" a pattern onto photoresist spun on a semiconductor wafer. Patterns containing the design of the devices are transferred from photomasks to the photoresist-coated wafer. Areas of the photoresist that are exposed to high energy light is subsequently removed using photoresist developer, in the case of positive tone photoresists. Areas the aren't exposed to the light are removed with photoresist developer for negative tone photoresists.

3.1 Etch Processing of the Top DBR

A dry etch process for patterning SiO_2/TiO_2 distributed Bragg reflectors (DBRs) for vertical-cavity surface-emitting lasers (VCSELs) was demonstrated. The etching was conducted using an inductively coupled plasma (ICP) system. Both SF_6/Ar and Cl_2/Ar based etching chemistries were investigated. Very slow etch rates were obtained for TiO_2 when using a Cl_2/Ar chemistry due to the low volatility of the etch products, $TiCl_x$. Using an SF_6/Ar based chemistry, similar etch rates for TiO_2 and SiO_2 were obtained, which is desired for etching through the alternating SiO_2 and TiO_2 layers of the DBR. An average etch rate of 1200 Å/min was achieved at ICP and radio frequency (rf) powers of 500 and 245W, respectively. Wet chemical etch processing was also explored using a buffered oxide etchant and diluted HF. Etch rates of 1200 and 2000 Å/min in dilute HF solution were obtained for TiO_2 and SiO_2, respectively. However, a significant etch-undercut of the DBR structure and delamination at the SiO_2/TiO_2 interfaces, due to internal stress created between these layers, were observed when these wet etchants were used.

The current approach to dielectric mirror definition is with a photoresist lift-off process, which is somewhat complicated. An alternative etching procedure could greatly simplify the mirror patterning process. The etch-back process, a dry etch technique that is widespread in silicon technology, is used for patterning metal contacts, dielectrics, and the semiconductor. The etch-back process offers advantages such as an anisotropic etch and high device fabrication yield.[23]

The layer structure of the dielectric mirror stack in our experiments consisted of seven pairs of SiO_2/TiO_2 layers (1700 Å/1140 Å) optimized for 980 nm wavelength

light, and was prepared using electron beam deposition on blank GaAs substrates at a substrate temperature of 200 °C. Although, the DBR structure is consistent with the structure that can be used for 980 nm wavelength VCSEL devices, the technology obtained from this study can be applied to SiO_2/TiO_2 DBRs for 850 nm VCSELs. AZ 1045, 1075, 4330, and 4620 positive photoresists were used as the etch masks. The plasma etch resistance of these resists was investigated. The patterned samples were hard baked at 90 °C for 20 minutes. They were then exposed to Cl_2/Ar or SF_6/Ar discharges in a Plasma Therm 790 Inductively Coupled Plasma (ICP) System. The ICP source power was varied from 300-500 W at 2 MHz. The sample chuck was also biased at different rf powers ranging from 100 to 245 W at 13.56 MHz. DC biases from −88 to 360 V were obtained for various ICP and rf power conditions. Etch rates were obtained from etch depths through at least four SiO_2/TiO_2 layers. The etch depths were measured using a Dektak II profilometer.

Wet chemical etching was conducted at room temperature using buffered oxide etchant or diluted HF solution. Photoresist was also used as the etch mask in these studies.

The photoresist liftoff approach for the patterning of dielectric mirrors limits the temperature at which the mirror layers can be deposited. Positive photoresists begin to cross-link at temperatures above 140 °C, and negative resists will begin to flow at temperatures above 200 °C. This causes a loss of edge sharpness and a degradation of the pattern. Figure 3-1 shows an SEM image of a dielectric DBR
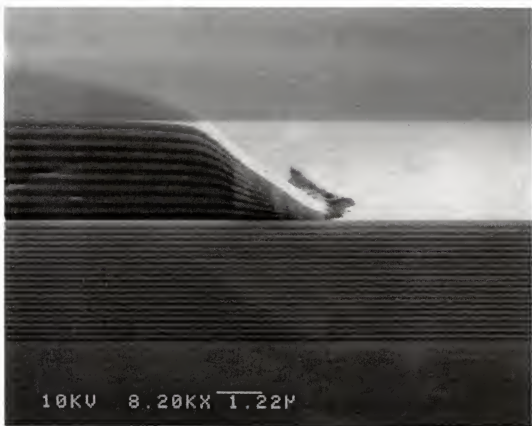
Figure 3-1 SEM of a dielectric mirror stack patterned with a negative resist lift-off process.

mirror patterned by photoresist liftoff after the photoresist was subjected to too high of a temperature during mirror deposition. The pattern size was reduced and the edge definition was poor, both due to resist flow during mirror deposition.

As commonly used in silicon device fabrication, the etch-back process can achieve better yield and more precise pattern definition, since the photoresist is applied and patterned after the material is deposited. However, the quality of the etch mask is very critical for the etch-back process. The mask must be able to maintain its integrity during the dry etch process. In other words, the etch selectivity of resist to dielectric mirror is important. Since the total thickness of the dielectric mirror is approximately 2 microns, a long dry etch time is needed (20-30 min). Therefore, a thicker resist is required as the etch mask. Four positive resists, AZ-1045, 1075, 4330, and 4260 were investigated. The resist thicknesses were 4.0, 7.1, 3.1, and 6.3 microns, respectively, applied with a 4000 rpm spin-speed coating for 30 seconds. Samples were cooled for 5 minutes after plasma etching periods of 2.5 minutes. Figures 3-2 to 3-5 illustrate the characteristics of etch resistance for these resists in Cl_2/Ar and SF_6/Ar discharges, respectively. The etch resistance to SF_6/Ar discharges of only two resists, 1045 and 4330, were examined. The etch rates of the resists are directly proportional to the ICP and rf power. Photoresist 4330 showed the best etch resistance to both plasma types. The etch resistance and spin-coat thinness is attractive for VCSEL fabrication since some VCSEL designs have pattern dimensions as small as 5 μm. Low pattern aspect ratio can be maintained with this resist for better pattern definition.
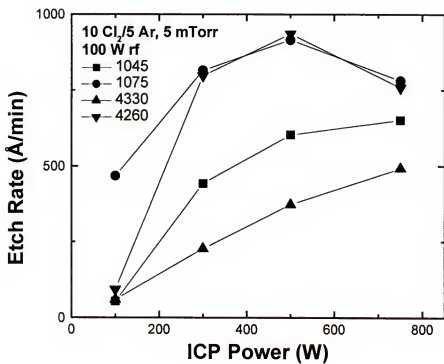
Figure 3-2 Etch rates of AZ 1045, 1075, 4620, and 4330 photoresists in Cl_2/Ar discharges plotted as a function of ICP power.
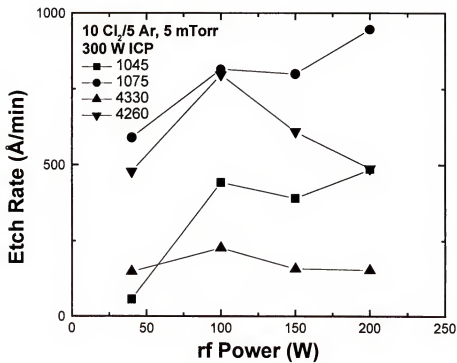
Figure 3-3 Etch rates of AZ 1045, 1075, 4620, and 4330 photoresists in Cl_2/Ar discharges plotted as a function rf sample chuck power.
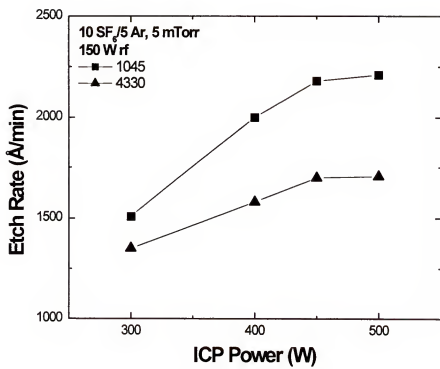
Figure 3-4 Etch rates of AZ 1045 and 4330 photoresists in SF_6/Ar discharges plotted as a function of ICP power.
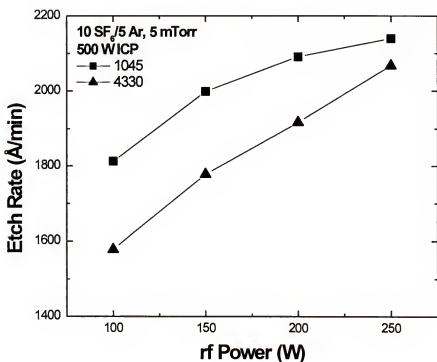
Figure 3-5 Etch rates of AZ 1045 and 4330 photoresists in SF_6/Ar discharges plotted as a function rf sample chuck power.

Cl$_2$/Ar and SF$_6$/Ar discharges were used to etch SiO$_2$/TiO$_2$ mirror samples. For the Cl$_2$/Ar chemistry, three runs were performed (500W ICP, 100W rf; 500W ICP, 150rf; and 500W ICP, 250W rf) and very low etch depths were obtained after 5 min. etches. This suggests a limiting etch rate from one of the layers. Etch experiments with single layers of SiO$_2$ only and TiO$_2$ only were performed to obtain the etch rate of the individual layers. It was found that SiO$_2$ etches ~3 times faster than TiO$_2$ in Cl$_2$/Ar at 500W ICP/250W rf. The etch rates of SiO$_2$ and TiO$_2$ were 800 and 280 Å/min., respectively. The etch product of TiO$_2$, TiCl$_x$, is not very volatile and therefore slows down the mirror etch. Etching the entire mirror stack using this chemistry would require more than 50 minutes, in which time the resist mask will have been etched through. Figures 3-6 and 3-7 show the etch rates of an SiO$_2$/TiO$_2$ mirror stack in SF$_6$/Ar and in Cl$_2$/Ar discharges as a function of ICP and rf power, respectively. The etch rates of the mirror stack in SF$_6$/Ar are around two to three times faster than in the Cl$_2$/Ar chemistry. This is due to the fact, that the TiO$_2$ etch product, TiF$_4$, in SF$_6$ is quite volatile and the etch rates of SiO$_2$ and TiO$_2$ in SF$_6$/Ar are comparable. As rf power was increased, the ion energy increased. A faster etch rate was achieved with increasing rf power. As ICP power is increased, ion density increases. The etch rate was also enhanced with increasing ICP power. The highest etch rate obtained was 1200 Å/min, and using the conditions for this etch rate, the total etch time for the entire mirror was reduced to 15 min. Figure 3-8 shows an SEM of a dry-etched mirror stack. Sharp edge definition was achieved using this process.
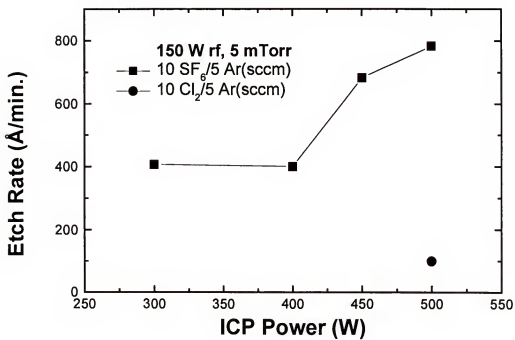
Figure 3-6 Etch rate of an SiO_2/TiO_2 DBR stack in SF_6/Ar and $Cl_2/$ Ar discharges plotted as a function of ICP power.
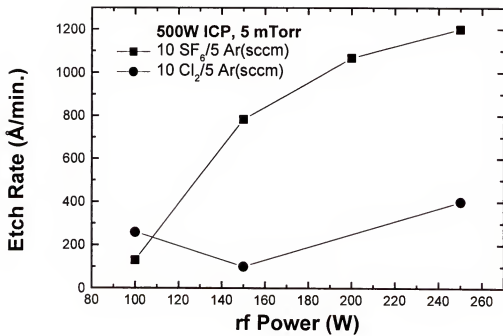
Figure 3-7 Etch rate of an SiO_2/TiO_2 DBR stack in SF_6/Ar and Cl_2/Ar discharges plotted as a function rf sample chuck power.
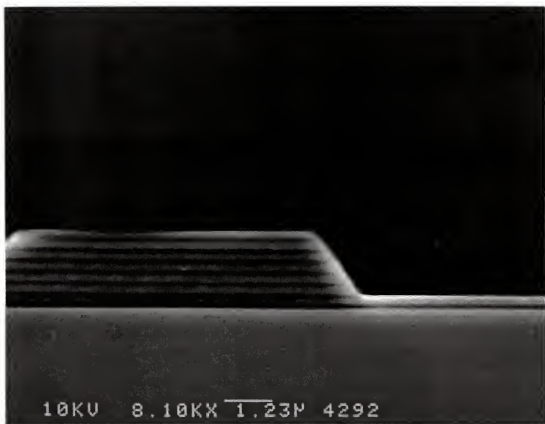
Figure 3-8 SEM of an etched SiO_2/TiO_2 DBR stack with SF_6/Ar discharge.

Wet oxide etchants HF and BOE were also used to etch the SiO_2/TiO_2 DBR mirror stacks. For wet chemical etching of the dielectric DBR, excellent adhesion of the resist to the dielectric is required to control the etch undercutting properties. Samples were patterned using photolithography and a postbake of the photoresist was done to ensure proper adhesion. Good etch rates were obtained using BOE and dilute $HF:H_2O$ (1:3). The etch rates were ~2,050 A/min and ~2.7 μm/min, respectively. However, as shown in Figures 3-9 and 3-10, significant etch undercut and delamination between SiO_2/TiO_2 interfaces were observed. This is due to internal stress between the layers of the dielectric DBR mirror. Some of the undercut observed extended more than 10-15 μm, which is larger than the dimensions of some of the mirror features. Therefore, the wet chemical process is not suitable for dielectric mirror patterning, as of now. A higher dielectric deposition temperature may help to anneal out the stress between the layers. Nevertheless, additional careful studies are needed.

In summary, a dry etch process to pattern SiO_2/TiO_2 dielectric mirrors with an ICP system using an SF_6/Ar based discharge was demonstrated. Similar etch rates of SiO_2 and TiO_2 were obtained with this chemistry. The etch resistance of positive resists was also studied and AZ-4330 and 1045 showed excellent etching resistance. Wet chemical etching with BOE and dilute HF was also explored, however, severe etch-undercut and delamination of the DBR layers were observed.
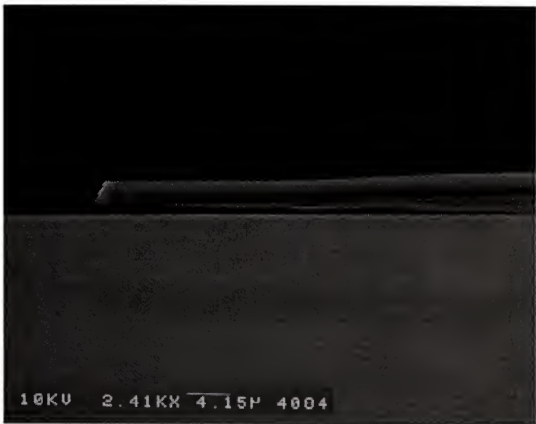
Figure 3-9 SEM image of a dielectric DBR stack patterned with HF. The photoresist
mask is present.

Figure 3-10 SEM image of a dielectric DBR stack patterned with BOE. The photoresist mask is present.

3.2 Ion Implantation

Ion implantation can be used to create regions of non-conductivity in doped semiconductors. The implantation process uses ions at high energies and doses to create damage in the crystal lattice of the semiconductor. The damage creates deep-energy levels that trap carriers in the material. With ion implantation, deep-levels can be created with good temperature stability against generation of carriers due to thermal heating of the device during operation.

Implant isolation is important in the fabrication of VCSELs because it can be used to form the current aperture. Good isolation is necessary in the formation of the aperture, because any leakage through the implanted regions will increase the amount of voltage required to obtain the current density for the devices to lase.

Ion implantation is also used to electrically isolate devices on a common wafer. For example, as in an individually addressable array with metal interconnects to the contacts of each of the VCSELs in the array. For this purpose, compensation of the near surface region is of importance to eliminate electrical crosstalk between the devices. For adequate electrical isolation between devices, typically a shallow implant using ions of heavy mass is used in conjunction with a deep implant using ions of lighter mass. The importance of the shallow implant is to compensate the near surface region.

The placement of the implantation is critical in the formation of the aperture. An aperture formed too shallow and far from the active region will lead to current spreading and inefficient current injection into the active region, while an aperture formed too deep and too far into the active region can reduce the radiative

recombination efficiency of the device and possibly create reliability problems in the devices. Devices fabricated for this work which used too high of an implantation energy showed spontaneous emission and did not lase. Lasing was not observed until the implantation energies were relaxed to an optimum level in which the active region received less damage.

W. Jiang et al. performed a reliability study on the effects of ion-implantation damage in the active region of the VCSEL.[24] The authors used two implantation conditions of differing energies. The higher energy condition was used to purposely introduce more damage into the active region of the device. The devices had a top semiconductor DBR, so a deep implantation through the top DBR was performed using H^{+} ions. The desired size of the aperture for their work was 10 μm. The implantation depths were verified by taking cross-sections and using stain etching.[25] The cross-sections show that the implant stops roughly four mirror pairs away from the active region for the shallower implant and two mirror pairs away for the deeper implant. Devices fabricated using the lower energy implant exhibited lower threshold currents than devices fabricated using the higher energy implant.

The devices fabricated from the two types of implant conditions were then tested for long-term reliability. The devices were operated at 10 mA at an elevated temperature of 110 °C to simulate the long-term operation of the devices. An optical microscope was used to monitor the light emission from the two types of devices. After 48 hours, a dark region began to form over the light-emitting region. The authors determined that the devices with the deeper implant lasted no longer than 500 hours at the accelerated conditions. Long-term reliability testing was performed on

the devices with the shallower implant and no obvious degradation was observed after 299 hours. The authors do not give the lifetime of the devices at the accelerated conditions, but estimate the devices to operate $>10^5$ hours at 10 mA and an ambient temperature of 40 °C. The degradation of the devices with the deeper implant was attributed to the propagation of point defects in the active region. The propagation of point defects have been observed in the GaAs/AlGaAs system.[26] The propagation of the point defects in the active region of the VCSELs were likely started by the heating effects which in normal operation is due to the current flow and photon generation in the active region.

Photoresist was used as the implantation mask for the VCSEL devices of this work. SRIM simulations were performed to verify that implantation does not penetrate into unwanted areas. The use of photolithography provides a precise method for forming the aperture. The benefits of photolithography on the reproducibility of the implant mask are also attractive for device fabrication. For the devices of this work, the preciseness of the aperture formation is enhanced as well because of the shallowness of the implantation performed. This is made possible by the use of a top dielectric DBR which is deposited and patterned as the final steps of the fabrication sequence.

A problem can arise with ion implantation is the channeling of ions in a semiconductor crystal. Channeling of ions occurs because of the highly ordered lattice of the target atoms in a crystal structure. Ions can travel along paths between rows of atoms and undergo fewer energy reducing collisions. The result is a significant amount of ions creating deep damage profiles that are difficult to control

and reproduce, especially with decreasing ion doses. In the case of forming apertures in VCSELs using ion implantation, the reduction in the effects of channeling is desired, to minimize damage in the active region. A narrower damage distribution is desired for aperture formation, so that the damage can be confined in the near-surface layers above the active region as much as possible. To reduce the effects of ion channeling, target samples can be tilted to remove the "rows of atoms" that implanted ions can channel between. For the ion implantation performed for this work, the samples were implanted at an angle of 7° from normal for this reason.

Isolation using implantation normally requires an activation anneal to maximize the effectiveness of the damage created. An as-implanted sample can actually show very high conductivity if not annealed. This conductivity comes from "hopping conduction", which is the conduction of trapped carriers between deep-level energy sites from damage created by the implantation process. Annealing will remove some of the damage to a level where hopping conduction is minimized and low conductivity is obtained.

3.2.1 SRIM Simulations

The stopping and range of ions in matter simulation software is used to simulate the ion distribution and vacancies created by ion implantation. The software allows for simulation of numerous implantation of ion species and for the input of multi-layer targets.

For the purposes of the fabrication of our VCSELs, simulations were performed for the photoresist implant mask and for the epitaxial structure. Shipley Corporation's AZ-1818 photoresist was used as the implantation mask for the

aperture formation step in the VCSELs of this work. The SRIM software package does not contain material parameters for this resist, so the software package's included material parameters for AZ-111 was used. The important material parameters required for the simulation are the target material's density and its constituent elements. AZ-1818's composition is a proprietary technology and the density of the photoresist will vary depending on the steps taken for preparing it for implantation, so we assume that it will be similar to the numbers included with the SRIM software for AZ-111. The density for AZ-111 in SRIM is .92 g/cm^3 and the elemental stoichiometry is $C_5H_8O_2$. Simulations were performed for the ion distribution and vacancy density in the photoresist implant mask to verify that it will not allow ions or the creation of damage to penetrate into the optical cavity. The thickness of the AZ-1818 photoresist after it is spun on the sample, patterned, and baked was measured using a profilometer and routinely was approximately 1.8 microns. This is the thickness used in the SRIM simulations.

Figures 3-11 and 3-12 show the results from the simulations for ion and vacancy distribution in AZ-1818 using the conditions for forming the aperture. The plots show that AZ-1818 sufficiently masks the high-energy O$^+$ ions from penetration into the VCSEL cavity.

The same types of simulations were performed for implantation into the optical cavity of the device. Figures 3-13 and 3-14 show the results from the simulations for ion and vacancy distribution in the optical cavity of the VCSELs of this work. The vacancy distribution is brought as close as possible to the active
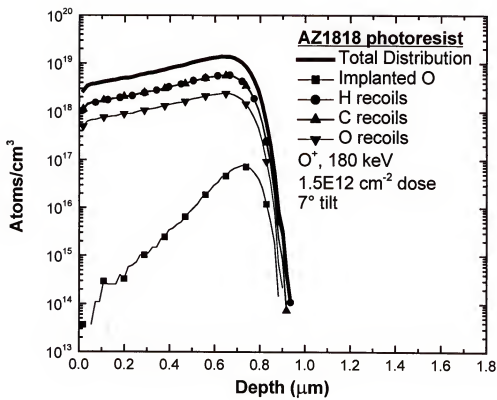
Figure 3-11 Implant distribution simulation using SRIM to evaluate the effectiveness of AZ1818 photoresist as an implant mask.
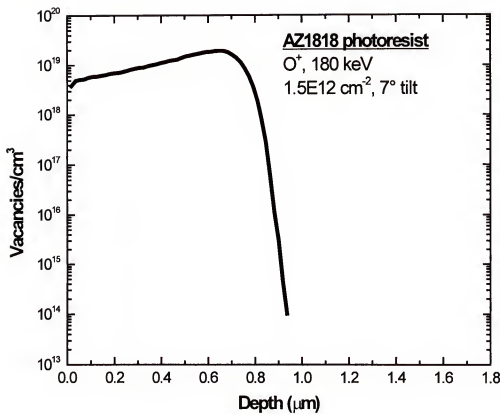
Figure 3-12 Damage distribution simulation using SRIM to evaluate the effectiveness of AZ1818 photoresist as an implant mask.
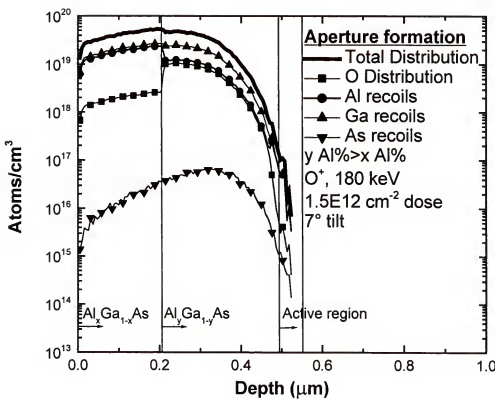
Figure 3-13 Implant distribution simulation using SRIM for aperture formation.
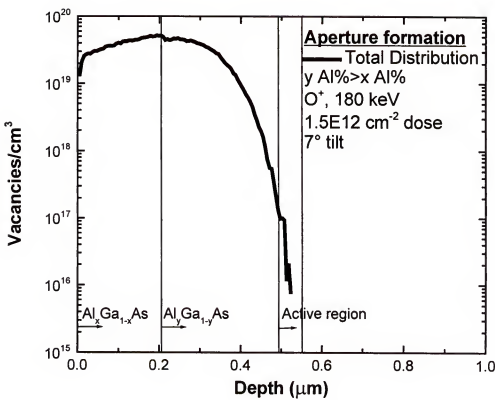
Figure 3-14 Damage distribution simulation using SRIM for aperture formation.

region of the device without introducing any significant damage or ions into it. The vacancy and implant distributions shifts by changing the ion energy for O^+ ions. Densities for the various percentages of Al in AlGaAs were calculated using the relationship:[27]

$$Al_x Ga_{1-x} As \text{ density } [g/cm^3] = 5.36 - 1.6x \qquad \text{Equation 3-1}$$

SRIM creates the distribution as vacancies/atoms per ion·Angstrom versus depth. The dose of the implant determines the density of the vacancies created and of the ions implanted into the cavity.

3.2.2 Physics of Recoil Cascades

Ions undergo energetic collisions with target atoms during ion implantation. These energetic collisions involve the transfer and loss of energy from the incident ions to the target material, until the incident ion loses its energy and stops. Nuclear and electronic stopping are the two effects that contribute to the energy loss of incident ions. Nuclear stopping involves the collision of the incident ion with nuclei of the target atoms. These collisions are elastic and involve the transfer of a large amount of energy. If the energy transferred is large enough to displace the target atom, the target atom will create a vacancy and continue to move undergoing collision processes of its own. The incident ion can continue moving until it loses enough energy to come to rest. This "chain reaction" of collision events that occur from one incident ion creates what is called a recoil cascade, where the word recoil refers to a target atom that is displaced from its original site.

Electronic stopping involves the interaction of the incident ion with bound electrons of target atoms. These interactions are largely inelastic and involve the

transfer of lower energies as compared to nuclear collisions. The transfer of energy results in the excitation of electrons of the target atoms and ionization of the atoms. These energies are dissipated into heat by the generation of phonons in the crystal lattice.

The assumptions that SRIM uses in regard to the physics of recoil cascades follow the fundamental ideas mentioned above.[28] Consider an incident atom with atomic number, Z_1, and energy E_1. This atom undergoes a collision with a target atom with atomic number, Z_2, and E_2. The target atom has some displacement energy, E_d, which is needed to move the atom from its site one atomic spacing away. It is assumed that if the target atom is not displaced by this amount, it remains in its original site. A displacement occurs then if $E_2 > E_d$. A vacancy is created if both a displacement of the target atom occurs as well as $E_1 > E_d$. If $E_1 < E_d$ and the incident atom is the same as the target atom, i.e., $Z_1 = Z_2$, then the incident ion replaces the recoiled target atom's site and no vacancy is created. If the incident atom and target atom are not the same, $Z_1 \neq Z_2$, then the incident atom becomes an interstitial atom. The energy of atom E_2 is reduced by an energy E_b, which is the binding energy of the target atom to its site. The energy E_2 that the target atom loses is assumed to go into the formation of phonons. The value for E_b is less than E_d. If $E_1 < E_d$ and $E_2 < E_d$, then the incident atom becomes an interstitial atom and the sum of E_1 and E_2 is dissipated into heat by the generation of phonons.
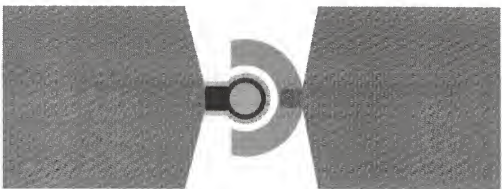
Figure 3-15 Mask design layout for one of the VCSEL device designs of this work.

3.3 Fabrication

Figure 3-15 shows the mask design layout for a VCSEL device of this work. The mask design layout contains multiple layers, each representing a layer written separately on a mask. Comparing the mask design layout to the SEM of an actual VCSEL fabricated in Figure 3-16, a very good transfer of the pattern from masks to semiconductor wafer using photolithography processing can be seen.

Many of the photolithography steps were performed on SiO_2 for fabrication of the VCSELs of this work. The SiO_2 was used to protect the region where light is emitted from the devices from processing steps that can etch away or roughen this surface. Damaging this surface can lead to degrading optical loss that can prevent the VCSEL from lasing. The SiO_2 is used effectively as a protective layer against damaging steps such as photolithography and wet-etching. The SiO_2 layer was removed prior to deposition of the top dielectric mirror. The presence of the protective SiO_2 layer requires performing photolithography on this layer. Performing photolithography on SiO_2 can lead to poor adhesion of the photoresist. To improve adhesion of photoresist to SiO_2, hexamethyldisilazane (HMDS) is used. The HMDS is spin-coated on the sample at 5000 rpm for 30 seconds prior to spin-coating of the photoresist. This allowed for sharp resolution of the patterned photoresist and prevented the lifting-off of small photoresist patterns during photoresist development. The SiO_2 was etched using buffered oxide etchant to remove it when necessary.

The following sections list the fabrication steps for the VCSELs of this work. Figures 3-18 to 3-24 show schematics for each of the steps.
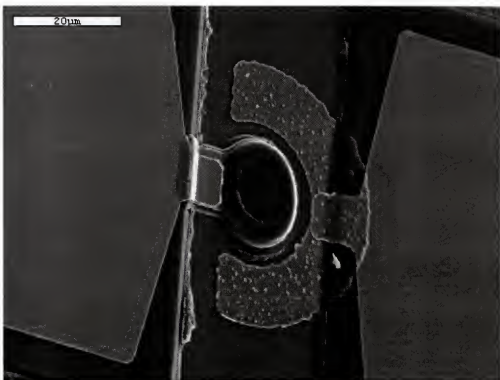
Figure 3-16 SEM image of a VCSEL of this work.
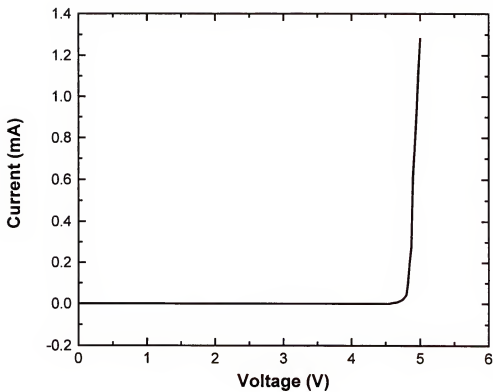
Figure 3-17 The forward-bias IV characteristic for a device fabricated without an implant mask for aperture formation showing the effectiveness of the isolation.
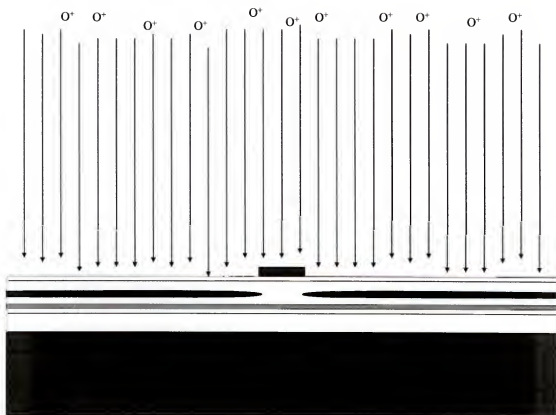
Figure 3-18 Schematic illustrating the aperture formation step of the VCSEL fabrication sequence.
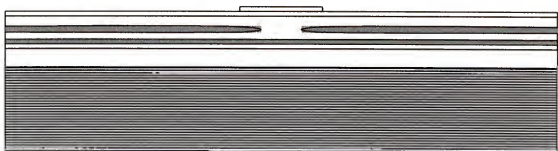
Figure 3-19 Schematic illustrating the index guide formation step of the VCSEL fabrication sequence.
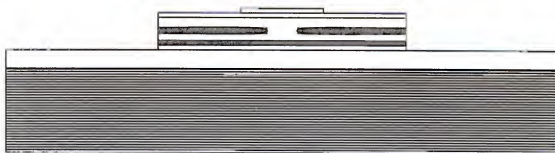
Figure 3-20 Schematic illustrating the device mesa etch step of the VCSEL fabrication sequence.

Figure 3-21 Schematic illustrating the n-contact formation step of the VCSEL fabrication sequence.

Figure 3-22 Schematic illustrating the p-contact formation step of the VCSEL fabrication sequence.

Figure 3-23 Schematic illustrating the top DBR formation step of the VCSEL fabrication sequence.

Figure 3-24 Schematic illustrating the test pad formation step of the VCSEL fabrication sequence.

3.3.1 Aperture Formation

Stopping and Range of Ions in Matter (SRIM) was used to simulate the ion implantation and damage distribution as described in the previous section. Oxygen ions were used as the implant species. Photoresist was included in the implantation simulations, and was determined to be sufficient for use as the implantation mask. The conditions used were 180 keV ion energy and $1.5e12$ cm^{-2} ion dose. Following implantation, an SiO_2 layer of about 3000 Å was deposited on the sample as an annealing cap and protection layer (see previous section). The sample was annealed at 500 °C for 30 seconds to activate the implant. Figure 3-17 shows a forward bias current-voltage characteristic for a device that received an implant on the entire area of the mesa. The plot is meant to show the effectiveness of the aperture implant.

3.3.2 Index Guide Formation

The index guide layer is the outermost layer of the optical cavity, and thus the last layer grown epitaxially in the structure. The index guide layer is a thin AlGaAs layer. The index guide layer is grown on top of a thin InGaP layer. The InGaP layer was grown into the structure to create an etch stop for precise patterning of the index guide feature. The InGaP etch stop layer helps to create reproducible index guide thicknesses. An H_3PO_4:H_2O_2:H_2O solution was used to perform the selective etch of the AlGaAs layer over the InGaP layer. Photoresist was used as the mask for patterning the index guide.

Optical confinement is achieved by the index guide mesas due to the refractive index step that is created once device fabrication is complete. The refractive index step arises from the AlGaAs material of the index guide and the first

layer deposited for the top dielectric DBR, SiO_2. The refractive indices for these two materials are 1.4 (SiO_2) and 3.5 (AlGaAs) at the 850 nm wavelength.

3.3.3 Device Mesa Etch

The device mesa etch is performed to unveil the highly doped n-contact layer in the epitaxial structure of the device. It is essential to remove completely the InGaP etch stop layer before proceeding with the device mesa etch. Not completely etching away this layer will lead to non-uniform etching that will propagate and worsen throughout the length of the etch. The result is an etch surface with rough surface morphology. A smooth etch can be obtained when the InGaP layer is properly etched away. An $HCl:H_2O$ solution was used to remove the InGaP layer. This solution has a high etch selectivity of InGaP over AlGaAs. For the device mesa etch, a phosphoric acid:hydrogen peroxide:water solution was used. This step does not have an etch stop layer to prevent over-etching, so it is critical that the etch depth is periodically monitored. The etch depth was monitored using a KLA Tencor profilometer and it was verified that the highly doped n-layer was reached by probing the surface and checking for high conductivity. Over-etching for this step can drastically degrade device performance. The n^+-layer is already relatively thin and over-etching it will create an unnecessarily high resistivity for current conduction. To add to the trickiness of this step, the etch rates of the p-, active, and n-regions varied, so care was taken so that the etch reached the desired layer.

3.3.4 n-Contact Metallization

The n-contact metallization used for the VCSEL of this work was Ge/Ni/Ge/Au/Pt/Au. The metals were deposited using electron beam evaporation. N-contacts were formed to the highly doped n-AlGaAs layer of the cavity which was unveiled by performing the device mesa etch. The n-contacts require a higher temperature anneal than is required for the p-contacts, so they were formed prior to the p-contacts. The metallization is deposited under high vacuum (~5E-8 Torr) conditions. The contacts were alloyed at 450 °C in a nitrogen ambient with the sample top face down on a GaAs blank wafer. The GaAs blank wafer was used as an annealing cap for the sample to reduce out-diffusion of arsenic from the VCSEL wafer during the high temperature process of annealing. The blank GaAs cap was etched in a phosphoric acid:hydrogen peroxide:water solution to create a fresh surface for the VCSEL wafer to contact prior to alloying. Out-diffusion of arsenic from the surface of the VCSEL wafer will create a gallium rich surface that will lead to surface current leakage in the devices. As can be seen in Figure 3-16, the n-contact has a grainy surface. The n-contact is the horseshoe shaped contact. This signifies that the metallization is reacting with the semiconductor. This reaction is important for the formation of low resistance n-contacts to AlGaAs. Very low contact resistances on the order of 1×10^{-6} Ω/cm^2 were obtained consistently.

3.3.5 p-Contact Metallization

The p-contact metallization used was AuBe/Pt/Au. The metals were deposited in the same manner as the n-contacts; using electron beam evaporation under high vacuum. The alloying condition was 280 °C for 30 seconds under a

nitrogen ambient. A blank GaAs wafer annealing cap was used and the same steps used for n-contact formation were taken to minimize contamination of the VCSEL wafer.

We noticed that an electrically insulating layer was formed on the top gold surface of the p-contact when trying to probe the devices. We had to use the probes to scratch the surface of the p-contacts with a good amount of force where a visible scratch was made on the contact in order to apply current in the devices. We believe that Be was diffusing to the top of the contact and forming an oxide during the alloying step. To test what we suspected, we removed this possible oxide layer by depositing a thin layer of titanium following the gold layer during deposition of the p-contact without breaking vacuum in the electron beam evaporator. Prior to lift-off of the metals, the titanium was etched away in dilute buffered oxide etchant. The titanium was determined to be etched away completely by observing the color change of the titanium to the contrasting color of gold. Lift-off was then performed as usual using an acetone spray. By following this method, we eliminated problems with the electrically insulating layer formed on the p-contacts. This method has greatly improved the electrical characteristics of the p-contact. Contact resistances on the order of 1×10^{-6} Ω/cm^2 were obtained consistently.

3.3.6 Top Mirror

The top mirror is patterned using Futurrex negative photoresist. This resist has the special property of being able to withstand high temperature processing. This property is necessary because the top mirror deposition process is a high temperature process. The deposition process is performed at a temperature of 200 °C. Layers of

the SiO$_2$/TiO$_2$ dielectric films are deposited using electron beam evaporation at the elevated temperature for about 2 hours. The resist is able to maintain its shape with good resiliency, so that the top mirror can be patterned for the devices. Lift-off was performed using a resist stripper, recommended by the manufacturer, heated up to 100 °C. Using acetone is ineffective for performing lift-off of this resist after it has been subjected to the high temperature top mirror deposition process.

The photoresist was patterned so that the SiO$_2$/TiO$_2$ stack was also deposited in areas for subsequent formation of test pads (next fabrication step). The dielectric material is not used as a reflector but used as a low capacitance pad support in this case.

3.3.7 Large Area Test Pads for High-Speed Testing

Devices fabricated for high-speed operation require large area test pads to support the probes for high-speed characterization. These probes have larger tips than standard probe tips and have a fixed distance between the ground and signal probes. Thus, the large area pad separation has to be designed to support the larger tips and fixed probe spacing. These design specifications are met by properly designing the photomask for patterning large area test pads.

The metallization used for the large area test pads is Ti/Pt/Au. This is a standard metallization used for adding metal to contacts or as a lead to a contact because of its good adhesion properties and low resistance. This metallization was able to adhere to the DBR dielectric material used for supporting the large area test pads and run along the dielectric material sidewall to contact to the device contacts.

CHAPTER 4
CHARACTERIZATION

4.1 Light Output Power-Current-Voltage (LIV) Measurements

The light output power-current-voltage measurement of a VCSEL is the most fundamental VCSEL characterization test that can be performed. It provides optical and electrical information on the performance of the VCSEL. From the optical and electrical information, fundamental laser parameters that describe the VCSEL's performance can be determined. The parameters that can be determined from an LIV characteristic are threshold current, slope efficiency, wall-plug efficiency, maximum output power, device series resistance, diode ideality factor, and the diode saturation current. Figures 4-1 and 4-2 show the LIV characteristics for multimode and single mode VCSELs of this work, respectively.

4.1.1 Parameters Obtained from LIV Measurements

The threshold current is the amount of current necessary for a VCSEL to lase. It marks the point where the device transitions from spontaneous emission to stimulated emission. In the spontaneous emission region, the VCSEL behaves like a light emitting diode (LED) with incoherent optical emission. In this region, there is not a high enough current density in the active region to support lasing. The wall-plug efficiency in this region is very poor as well. When the device reaches the
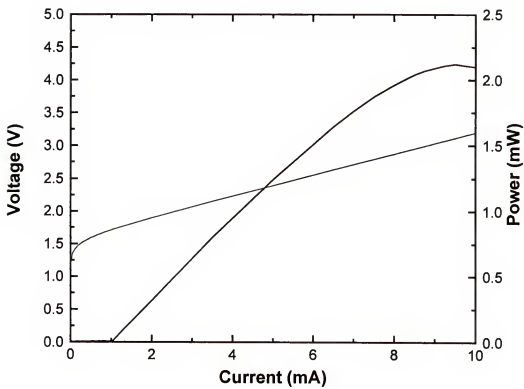
Figure 4-1 Light output power-current-voltage plot for a multimode VCSEL of this work.
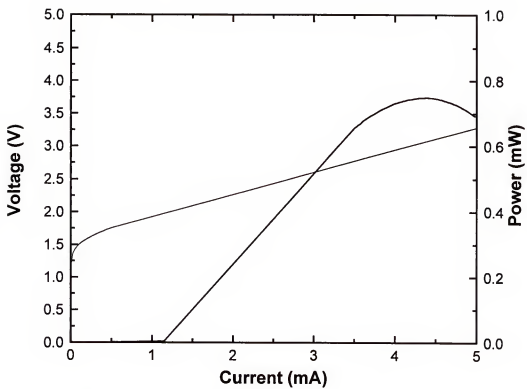
Figure 4-2 Light output power-current-voltage plot for a single-mode VCSEL of this work.

threshold current, stimulated emission begins. Light amplification and gain occur in the active region with photons generated in phase, and thus the obtainable coherent properties of the light emission. During stimulated emission, the VCSEL begins to improve dramatically in wall-plug efficiency. The power output above threshold shows a linear dependence with the drive current, until self-heating in the device is too high and thermal rollover occurs, degrading the light output power.

Slope efficiency describes how well the light output power of the VCSEL responds to increasing drive current. Its units are in watts/ampere. This parameter can be determined very simply from an LI plot. It is the slope of the LI line above threshold. A higher slope efficiency indicates that the device is more efficient at reaching a certain light output power with less drive current.

Wall-plug efficiency is a quick way of determining the performance of a VCSEL. It is the ratio between the input electrical power to the light output power. Figures 4-3 to 4-6 show plots of the wall-plug efficiency versus current against light output power and input electrical power for multimode and single-mode devices of this work.

Maximum output power occurs at the peak of the LI curve, where it no longer behaves in a linear fashion with increasing current. Device self-heating with increasing current decreases the light output power. This is due to the misalignment of the cavity resonances and the peak of the gain curve. The maximum output power is an important parameter because it describes the maximum strength of the signal transmitted by the VCSEL. For fiber optic networks, a stronger signal will travel a farther distance.
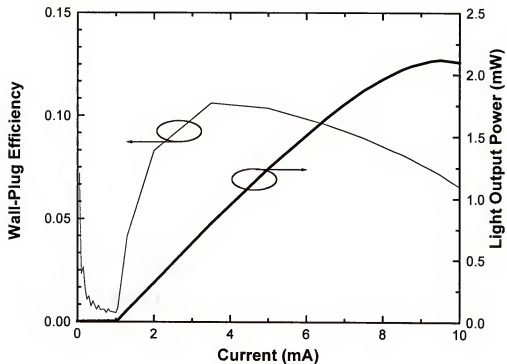
Figure 4-3 Light output power-current-wall plug efficiency plot for a multimode VCSEL of this work.
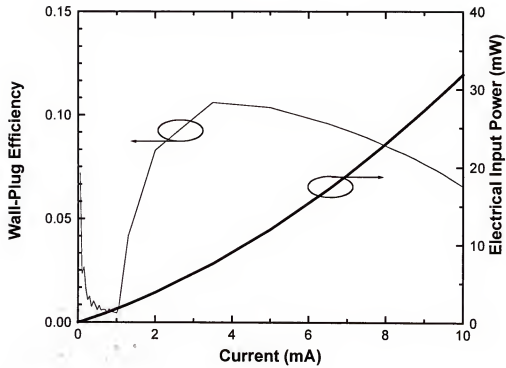
Figure 4-4 Electrical input power-current-wall plug efficiency plot for a multimode VCSEL of this work.
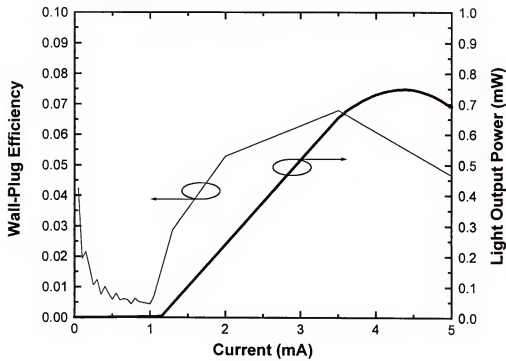
Figure 4-5 Light output power-current-wall plug efficiency plot for a single-mode VCSEL of this work.
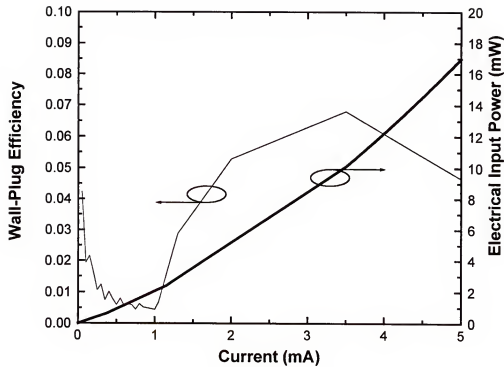
Figure 4-6 Electrical input power-current-wall plug efficiency plot for a single-mode VCSEL of this work.

As more voltage is applied to the terminals of the VCSEL, more current will increasingly flow through the device. The resistance that the current encounters will not be constant at all voltage bias levels. The current will be very small up to a certain voltage, where the device "turns-on" and a large amount of current begins to flow through the device. This voltage is the ideal diode voltage and depends on the material of the active region. Beyond this voltage, the current encounters exponentially decreasing resistance and begins to increase linearly with voltage. In this linear region the resistance has approached the series resistance of the device. The series resistance of the device will include resistance from the contacts and the semiconductor materials. From an IV curve, the device series resistance is determined from the slope of the linear IV region. Figure 4-7 shows a plot of the behavior of the differential resistance, $\frac{dV}{dI}$, with increasing current.

The diode ideality factor describes the type of current transport occurring in the diode. A value of 1 for the ideality factor describes ideal diffusion current and a value of 2 describes Shockley-Read-Hall recombination current. For the lasing VCSEL, an ideality factor of 2 is expected because the mechanism for photon generation is the recombination of electrons and holes. To determine the ideality factor, the following expression is used:

$$I_F \propto \exp\left[\frac{qV}{nkT}\right] \qquad \text{Equation 4-1}$$

where I_F is the forward current, q is the fundamental electronic charge, V is voltage, n
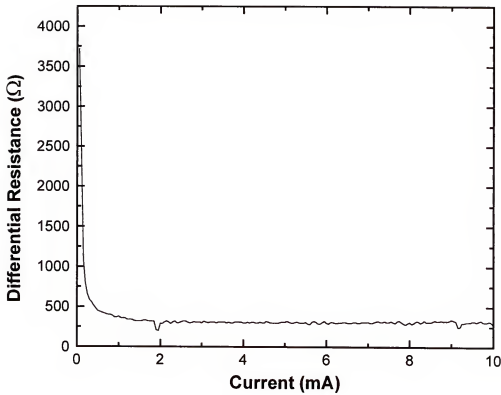
Figure 4-7 Plot showing the behavior of the differential resistance with increasing current.

is the diode ideality factor, k is Boltzmann's constant, and T is temperature. Typically, to determine the diode ideality factor, an IV curve is obtained and plotted as ln I_F vs. V. The slope of the curve is equal to $\dfrac{q}{nkT}$, and n can be determined.

Also from a ln I_F vs. V plot, the diode saturation current can be obtained. Data points for the current from small voltage intervals are required to resolve the current behavior at low voltage. An extrapolation of the IV curve to the current axis is performed, and the V=0 value for current is the diode saturation current.

4.1.2 Experimental Setup

Because VCSEL technology is relatively new and widespread acceptance is gradually occurring, there has not been a commercially available optical characterization set-up for testing surface emitting lasers. Electronic device characterization has long had the luxury and convenience of probe stations. Although, elaborate alignment systems and translation stages on an optical bench can be used to support electrical and optical VCSEL characterization, as is normally done with edge-emitting lasers, there really isn't a substitute for the ease of performing on-wafer testing using probe stations. For example, the probe station doesn't require wax or other bonding material to mount a sample for testing. Some probe stations use vacuum to hold a sample in place, but this usually is only necessary for movement sensitive rf measurements. Because of the VCSEL's unique structure, on-wafer testing is possible and a probe station can be fashioned for characterizing these devices.

Figure 4-8 shows a schematic of the setup used for performing the LIV measurements. In order to perform LI measurements, a photodetector is required for measuring the output power of the device. The current-voltage characteristic is obtained using a standard HP 4145 parameter analyzer. The photodetector converts the optical power emitted from the VCSEL to current based on the photodetector's responsivity. Since the responsivity of the detector is a function of the incident wavelength, and the VCSEL can emit a fairly broad spectrum, an appropriate value for the responsivity should be used. The VCSEL device fabricated for this work had light emission in the wavelength range of roughly 825-875 nm. In this range the responsivity doesn't change drastically, and can be assumed to be roughly 0.55 A/W, as can be seen in Figure 4-9.

A barrel-screw was machined so that it would fit into the objective lens port of the probe station microscope. A photodetector with a BNC connector is mounted in the barrel screw. The BNC connector is required to transmit the current signal from the photodetector to the HP 4145. The current is measured by the HP 4145 and the optical power is calculated based on the responsivity of the photodetector. A large area detector is used for these measurements to ensure that all of the light from the VCSEL is collected. The photodetector had an anti-reflection (AR) coating to reduce light power loss.

The HP 4145's settings were set to sweep current, measure voltage on the device terminals, and measure current from the photodetector for LIV measurements.
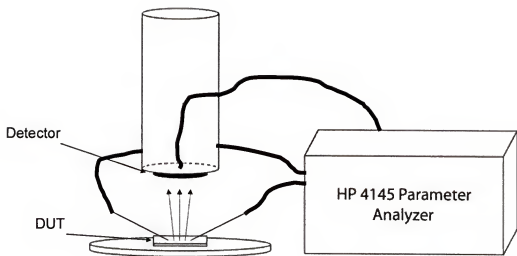
Figure 4-8 Schematic of the equipment setup for light output power-current-voltage measurements.
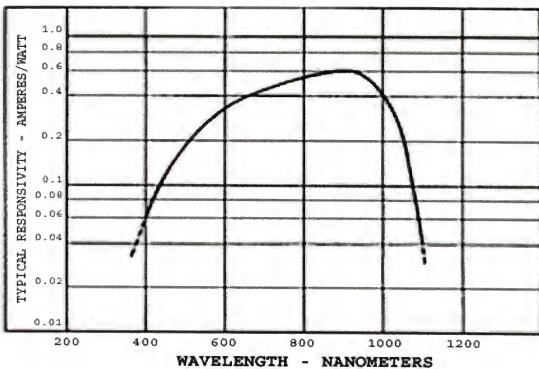
Figure 4-9 Responsivity vs. wavelength plot for EG & G's C30810 detector.

The HP 4145 is able to obtain the device voltage and photodetector current measurements simultaneously so that only a single current sweep is required to obtain an LIV curve.

Having an anti-reflection coating on the surface of the photodetector will enhance the number of photons reaching the detector and thus increase the number of photons absorbed by the detector for increased power measurement accuracy. Anti-reflection coatings are typically a dielectric film of optimal thickness for reducing reflection of a specific wavelength. The rule followed to determine the thickness of the coating is:

$$t = \frac{\lambda}{4n}$$
Equation 4-2

where λ is the wavelength of interest for reduced reflection and n is the refractive index of the AR coating at wavelength λ. For example, using SiO_2 (n=1.4) as the anti-reflective coating for 850 nm light, the thickness of the coating should be 151.79 nm.

The photodetector operates by conducting current when incident light falls on the surface of it. The light is absorbed by the device and electron-hole pairs are generated, increasing conductivity in the device. A suitable photodetector is required for light at 850 nm wavelength. Silicon-based photodetectors are suitable for detecting light at this wavelength. The bandgap energy of silicon is 1.12 eV, and the cut-off wavelength of silicon, which is the value for which wavelengths greater than it would not contribute to photoconduction, is:

$$\lambda_c = \frac{1.24x10^3}{E_g}[nm]$$
Equation 4-3

where Eg is the bandgap energy of the semiconductor in eV. For a silicon photodetector, wavelengths greater than 1107 nm would not be detected because the energy of the light would be too low in energy to create electron-hole pairs in the photodetector.

The responsivity of the detector is directly related to its quantum efficiency. The quantum efficiency of a photodetector is defined as the ratio of the number of electron-hole pairs contributing to photoconduction to the number of incident photons on the detector, or:

$$\eta = \frac{\left[\frac{I_{ph}}{q} \right]}{\left[\frac{P_i}{h\nu} \right]}$$

Equation 4-4

where I_{ph} is the current due to photoconduction, q the fundamental electronic charge, P_i is the optical power incident on the photodetector, and hv is the energy of the photon. The responsivity of the detector is a specification normally reported by photodetector vendors. The responsivity is defined as the ratio of the current due to photoconduction to the incident optical power:

$$R = \frac{I_{ph}}{P_i} = \frac{q\eta}{h\nu}$$

Equation 4-5

or in terms of the photodetector quantum efficiency:

$$R = \eta\lambda/1.24$$

Equation 4-6

Responsivity is typically reported in units of [A/W].

The photodetector used for the LIV measurements was an EG & G C30810 silicon p-i-n photodiode. This photodiode has a 400 nm to 1100nm wavelength detection range. The 1100 nm long wavelength cutoff value is expected due to the

bandgap energy of silicon, but the short wavelength cut-off at 400 nm is due to the increased optical absorption of silicon at the shorter wavelengths and thus a reduced quantum efficiency and responsivity.

4.2 Optical Spectra

An optical spectrum analyzer reveals valuable information on the characteristics of light emission from laser devices. It is used to determine the modal make-up of light and the relative intensities of the modes. The optical characteristics of a laser are desired because the wavelength is an important specification for applications such as optical fiber telecommunications. The transmission medium of optical fiber has an optical power loss, or attenuation, dependency on wavelength. For short-area networks, the wavelength specification is 850 nm where the attenuation is expected to limit signal transmission to 300 m.

4.2.1 Optical Spectrum Analyzer (OSA) Operation

An HP 70952B optical spectrum snalyzer (OSA) was used for obtaining optical spectra from the VCSELs of this work. This OSA uses a double pass monochromator to select the wavelengths of light being analyzed. The double pass monochromator uses various components to accomplish this as can be seen in Figure 4-10. First input light is focused onto a diffraction grating using various collimation and focusing optics. The light is collimated to enhance the operation of the monochromator. The light is incident on a diffraction grating that is rotatable to change the angle of light incidence on it. The diffraction grating is normally a
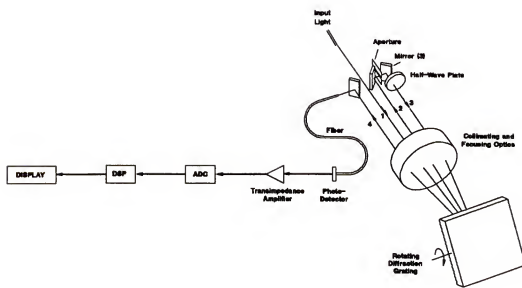
Figure 4-10 Schematic of the internal components of an optical spectrum analyzer.

polished glass-based substrate with thousands of equidistant grooves per centimeter. The diffraction grating disperses the incident light into the light's electromagnetic components based on wavelength. The characteristics of the dispersed light will depend on the groove spacing and the angle of incidence.

Following the dispersion of the light on the diffraction grating, the light is collimated and travels through an aperture slit. The aperture slit width determines the wavelengths that passes through to the detector. The narrower the aperture slit is, the narrower the wavelength band, $\Delta\lambda$, becomes. The diffraction grating is rotated to the proper position so that the desired center wavelength λ of the wavelength band $\Delta\lambda$ passes through the aperture. The half-wave plate is present after the first pass to reduce polarization sensitivity of the monochromator. When unpolarized light is dispersed by a diffraction grating, the attenuation of the light is dependent on the polarization angles of the light. The maximum and minimum attenuation levels of the light cycle every 90 degrees in the polarization angles. The half-wave plate rotates the polarization angle of the light 90 degrees, so that polarization angles receiving high attenuation on the first pass will receive a reciprocated low attenuation on the second pass. This helps to make the monochromator insensitive to polarization effects of the light. This completes the monochromator portion of the optical spectrum analyzer. The monochromator in a sense is a tunable filter that selects the wavelength band by rotation of the diffraction grating. The resolution of the monochromator is defined as:

$$\text{Res} = \frac{\Delta\lambda}{\lambda} \qquad\qquad \text{Equation 4-7}$$

The light is then directed towards a photodetector. The photodetector converts the optical signal into an electrical signal that is processed into useful information for the OSA user about the optical properties of the light, such as the optical power versus wavelength plot, through the display.

4.2.2 Experimental Setup

The required equipment needed for optical spectrum analysis of VCSELs include a probe station, optical fiber, a collimating lens and an optical spectrum analyzer. Figure 4-11 shows a schematic of the setup for performing optical spectra measurements. Similar to the setup for measuring the LIV curve for VCSELs, a barrel mount is used to contain the optical fiber. A collimating lens coupled to the optical fiber is mounted in the barrel for coupling the light from the VCSEL. The optical fiber is connected to the input port of the optical spectrum analyzer for analysis.

4.2.3 Optical Emission Spectra

VCSELs inherently have shorter cavity lengths than edge-emitting lasers. The separation between the longitudinal modes of the laser has an inverse relation to the cavity length. The VCSEL, because of its shorter cavity length, will have a larger separation between longitudinal modes than edge-emitting lasers. Figure 4-12 shows an illustration of the difference in cavity length between edge-emitting lasers and VCSELs. The cavity length of the VCSEL is on the order of one wavelength, while the cavity length of the edge-emitting laser can be hundreds of wavelengths.
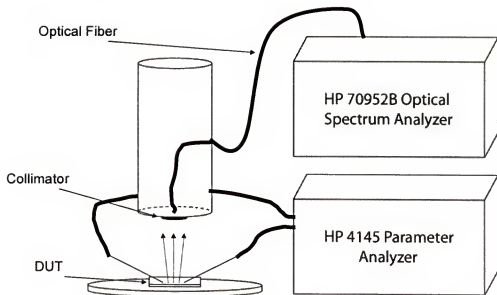
Figure 4-11 Schematic of the equipment setup for optical spectrum measurements.
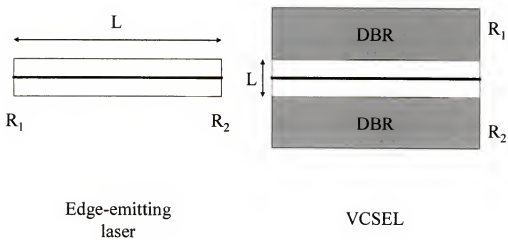
Figure 4-12 Illustration showing the difference in cavity length, L, between edge-emitting lasers and VCSELs.

In addition to the longitudinal modes supported in the cavity of the device, transverse modes can also be supported. The transverse modes are dependent on the aperture size of the device. The problem of determining the transverse modes supported by the aperture size of the VCSEL is a complex one, but a systematic experiment where the longitudinal cavity structure is the same and the aperture size varied simply by changing its size on the photomask level, will provide information on how small the aperture should be for single-mode operation. The only trade-off for reducing the aperture size is that the maximum output power will decrease as aperture size decreases. The factors contributing to this are a smaller gain region for fewer photons being generated and higher current densities, which leads to excessive heating and ultimately thermal rollover at lower drive currents.

Optical spectra for multimode and single-mode VCSELs fabricated for this work are shown in Figures 4-13 and 4-14. A single-mode VCSEL ideally will have solely the longitudinal mode with higher order modes greater than 30 dB lower in intensity. Multi-mode VCSELs would have higher order modes that are less than 30 dB lower in intensity. Higher order transverse modes gain intensity as the current injection increases in the device, so single-mode behavior is reported for a current range from threshold to some current where the fundamental mode becomes less than 30 dB in intensity than the side modes. Figure 4-15 shows optical spectra taken at various drive currents.
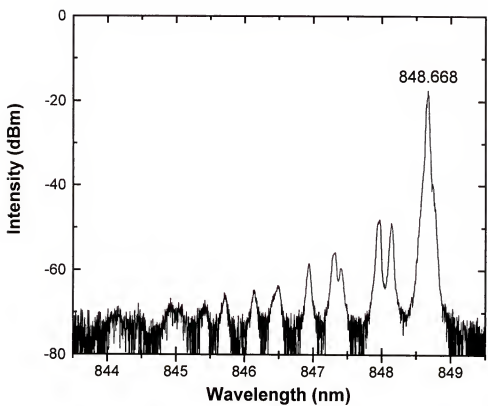
Figure 4-13 An optical spectrum for a device operating with multimode characteristics.
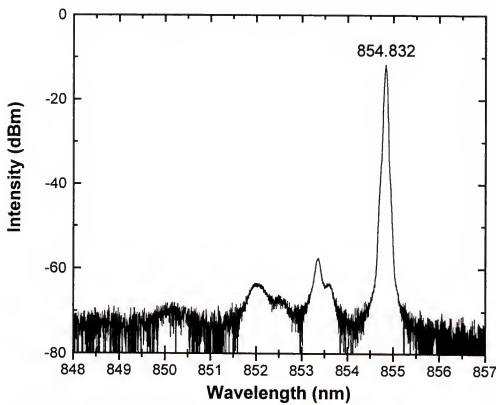
Figure 4-14 A characteristic optical spectrum for a VCSEL with single-mode operation.
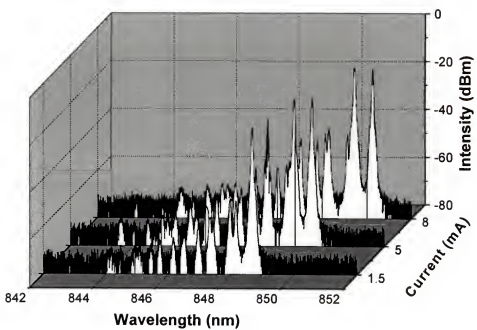
Figure 4-15 Evolution of the optical spectra versus current.

4.3 Resistance Analysis

The individual resistances arising from current transport through the semiconductor layers and the ohmic contacts in the VCSELs of this work have been calculated from theoretical and transmission line method data. The results can be used to simulate the expected VCSEL current-voltage characteristic, which shows excellent agreement with the experimental data. This process provides a simple method for predicting the effect of changes in epitaxial layer structure thicknesses, doping and materials on the dc characteristics of high performance VCSELs.

In creating new VCSEL designs or in attempting to understand the effect of contact quality on VCSEL performance, it is useful to be able to have a simple method for predicting the impact of these changes on the dc characteristics. A key parameter in this regard is the distributed resistance for the diode. Device resistance in VCSELs has contributions from the contacts and from the semiconductor. Total device resistance can be estimated by treating the device as a network of resistors. The various resistances come from the detailed growth structure of the VCSEL and depend on the current transport path in the devices. For our particular device design, we can breakup the network of resistors into categories for radial current conduction in the p- and n-layers, vertical current conduction through the device aperture, and resistance from the device contacts. A schematic of an implant-apertured, index-guided VCSEL with the individual resistance components is shown in Figure 4-16.
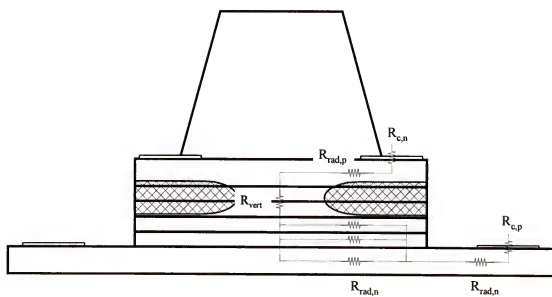
Figure 4-16 Schematic representation of the VCSEL of this work, showing individual resistance components.

4.3.1 Contact Resistance Contribution

From TLM measurements, we can obtain information on the contact resistances and their corresponding transfer length in the devices and sheet resistance of the semiconductor layers. The transfer length along with contact length gives an estimate of the area of a device contact used to transfer current from the contact to the semiconductor. This effective contact area along with specific contact resistance obtained from TLM measurements will give the resistance contribution of the contact to the total device resistance. For example, the p-contact has an annular design, with an inner radius of 6.5 microns and an outer radius of 8.5 microns. From TLM data, the transfer length for the p-contact was determined to be 1.35 μm. The effective p-contact area can be determined using the simple calculation:

$$\pi\left((6.5+1.35)\mu m\right)^2 - \pi\left(6.5\mu m\right)^2 = 60.86\mu m^2 \qquad \text{Equation 4-8}$$

This gives a p-contact resistance contribution of 17.09 Ω for a specific p-contact resistance of 1.04×10^{-5} Ω-cm^2.

The n-contact resistance contribution was calculated in a similar manner. Along with reducing the actual n-contact area of the device using the transfer length approximation to calculate the effective area of the device, 1.04 μm in this case, non-conducting areas underneath the contact where a second ion implantation step in the device fabrication process was used, are not included. The total calculated effective n-contact area is 35.97 μm^2 and for a specific contact resistance of 5.56×10^{-6} Ω-cm^2, this gives an n-contact resistance contribution of 15.46 Ω to the total device resistance. The total contribution of the p- and n-contacts to the device resistance is 32.55 Ω.

4.3.2 Resistance Due to Radial Conduction in Device

Radial conduction can be considered to be the dominant mode of current transport in the device between the device aperture and the contacts. On the p-side of the device, the layers were engineered using varying doping concentrations so that current would spread radially and then vertically through the aperture for uniform current injection into the active region. On the n-side though, the layers are very close in doping concentration, so the current would follow an oblique path as defined by the Gaussian-like distribution of the implanted ions that form the aperture. But if we recognize that the lateral distance from n-contact edge to aperture edge is ~10 μm and that the vertical distance from the contact to aperture is ~0.15 μm, we can see that resistance due to the semiconductor layers will be characterized by radial conduction.

From TLM measurements, the sheet resistance for p-radial conduction to the aperture was determined to be 570 Ω/ . The radial current conduction from the annular p-contact edge to the circular aperture edge will flow from the inner radius of the p-contact to the outer radius of the aperture. For this device design, the outer radius would be the p-contact inner radius, 6.5 μm, and the inner radius would be the radius of the aperture feature, 3.5 μm. The total resistance for lateral current flow in an annulus is:

$$R = \frac{\rho_s}{2\pi} \ln\left(\frac{R_o}{R_i}\right)$$ Equation 4-9

where ρ_s is the sheet resistance, and R_o and R_i are the outer and inner radius of the annulus. The semiconductor resistance for lateral conduction from the p-contact to the aperture is then 56.16 Ω.

Radial conduction from the n-contact to the aperture can also be handled using the above equation. The sheet resistance measured from TLM data can only be applied for lateral current conduction layers below the n-contact, though. For lateral conduction in layers of the device mesa above the n-contact, the sheet resistance is estimated using the following expression:

$$\rho_s = \frac{1}{qt(\mu_n N + \mu_p P)}$$ Equation 4-10

where q is the electronic charge, μ is the n-type or p-type carrier mobility denoted by the subscript, t is the thickness of the layer and N and P are the electron and hole concentrations, respectively. When considering n-type material (i.e., N>>P), the second term in the denominator can be ignored. The resistance due to n-lateral conduction in the device includes a resistance from the n-contact edge to the device mesa edge in series with resistances in parallel from the mesa edge to the aperture edge. The number of resistances in parallel includes the layer used for n-contact formation and any layers between it and the aperture. For the epitaxial structure of this work, there would be one resistance in series with a group of three resistances in parallel. To calculate the resistance from the contact edge to the device mesa edge, we use a modified form of the equation for radial current conduction in an annulus. The modification comes from the geometry of the n-contact. The n-contact is a truncated annulus and as mentioned earlier, there are areas of non-conductivity underneath the n-contact. The 2π term in the equation for radial conduction in an annulus has to be modified to account for the actual number of radians in the geometry of the n-contact. This was determined to be 1.26 radians, or $1/5^{th}$ a circle. So substituting 1.26 for 2π in the equation, and using R_o=13.5 μm (inner radius of the

contact) and R_i=10.5 μm (radius of circular device mesa), the resistance is calculated to be 104 Ω for a sheet resistance of 521 Ω/□, determined from TLM measurements. For the three resistances in parallel that describe the n-radial resistance from the device mesa edge to the aperture edge, which is a distance of 7μm, the unmodified form for calculating resistance for lateral current flow is used, since the current is allowed to flow from the entire circumference of the circle defined by the 2nd implantation step. The calculated resistances and pertinent information are shown in Table 4-1.

The three resistances in parallel are equivalent to 71.63 Ω. This resistance in series with the resistance for radial conduction from the n-contact to the device mesa edge gives a total radial resistance of 175.63 Ω on the n-side of the device.

4.3.3 Vertical Current Conduction

As mentioned before, resistance due to vertical conduction in our VCSEL devices will be small as compared to radial conduction. The current will travel through very thin layers for a total thickness of about ~0.3 μm. The current is assumed to conduct through a cylinder or a series of disks if you look at layers separately, with a radius of 3.5 μm, as defined by the aperture size. The equation for estimating resistance for current flow through a disk is:

$$R = \frac{\rho d}{\pi r^2} \qquad \text{Equation 4-11}$$

where ρ is resistivity, d is the thickness of the layer, and r is the radius of the aperture. This cylinder model will overestimate the resistance of vertical conduction

Table 4-1 Electrical properties of n-radial current injection layers.

Layer	Thickness	Doping	Dopant	Est. H-Mobility	Est. E-Mobility	Resistivity (W-cm)	r_a (W/sq.)	R (W)
Al_5Ga_5As	303	5.00E+17	Si	n/a	225	5.55E-02	18310.22	3.20E-03
Al_5Ga_5As	1297	1.00E+18	Si	n/a	225	2.77E-02	2138.78	373.61
$Al_{.12}Ga_{.88}As$	1803	3.00E+18	Si	n/a	225	9.25E-03	512.85	91.14

because the actual shape will be that of an hourglass as created by aperture formation using ion implantation. Table 4-2 shows a compilation of the calculated resistances due to the ohmic contacts and to the vertical and lateral current conduction.

4.3.4 I-V Characteristics

Using the calculated resistances, we were able to calculate the expected I-V characteristic from our lasers using the relation

$$I_F = I_{sat} \exp\left[q(V_F - R_T I_F)/m k_B T\right] \qquad \text{Equation 4-12}$$

where I_F and V_F are the forward bias current and voltage, I_{sat} is the saturation current density, R_T is the total series resistance in the device, and m is the diode ideality factor. The value I_{sat} was determined by extrapolating the forward I-V characteristic to the V=0 axis. This value was determined to be ~6e-16 mA. An ideality factor of 2 was used for this model. This is the value used to describe Shockley-Read-Hall recombination current, which is what we observed for our implanted VCSELs. The total device resistance was determined to be 310.9 Ω using the methods described in the previous sections.

Figure 4-17 shows a comparison of the calculated and experimental I-V characteristics. There is clearly excellent agreement, indicating the accuracy of our simple model for the resistance components.

Accounting for the distributed resistances in an implant apertured, index-guided VCSEL allows for an accurate prediction of its I-V characteristics. This method will be useful for examining the effect of layer structure changes on the dc performance of VCSELs.

Table 4-2 Compilation of calculated resistances in VCSEL structure.

$R_{c,n}$	N-contact	15.5Ω
$R_{c,p}$	P-contact	17.1Ω
$R_{rad,n}$	N-side lateral conduction	175.6Ω
$R_{rad,p}$	P-side lateral conduction	56.2Ω
R_{vert}	Vertical conduction through aperture	46.5Ω
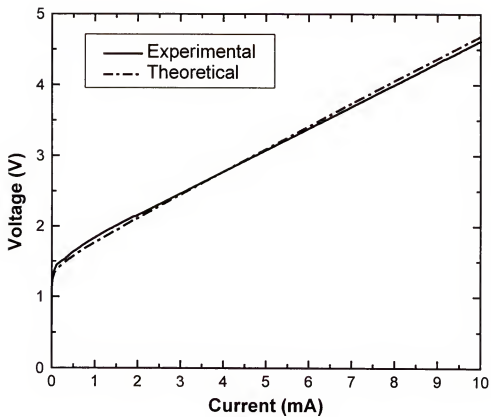
Figure 4-17 Comparison of calculated and experimental I-V characteristics from 850 nm VCSEL.

4.4 Small-Signal Analysis

Small-signal analysis is an important and helpful characterization method for gaining insight on the capabilities and limits of VCSELs. Small-signal analysis is used to obtain a host of information on the VCSEL. The most ostensible piece of information that can be obtained is the modulation bandwidth of these devices. Though it doesn't measure the modulation bandwidth of the laser using practical parameters such as bit-error rate, as is obtained from large-signal analysis, an accurate estimate of the large-signal modulation bandwidth can be obtained from the 3 dB frequency of the device using small-signal analysis (-3 dB from the laser's low frequency response). In this respect, small-signal analysis can serve as a useful preliminary test on how well the device will perform under large-signal modulation.

Figures 4-18 and 4-19 show the small-signal frequency responses for multimode and single-mode VCSELs of this work, respectively. The dashed lines mark the low frequency response and 3 dB below it. As can be seen from the plot, the maximum 3 dB bandwidth obtained for this device is greater than 10 Ghz. The bandwidth was limited by the speed of the detector used for these measurements.

The modulation conversion efficiency factor (MCEF) is a figure of merit that is used to describe the small-signal frequency response of a laser above threshold with increasing drive current.[29] Originally the MCEF was proposed for edge-emitting lasers, but the figure applies equally well to VCSELs. The MCEF is defined as:

$$MCEF = \frac{f_{3dB}}{\sqrt{(I - I_{th})}} \qquad \text{Equation 4-13}$$

where f_{3dB} is the 3 dB frequency, I is the drive current above threshold, and I_{th} is the

3.00 dB/ DIV

START 10.0 MHz   STOP 16.00 GHz
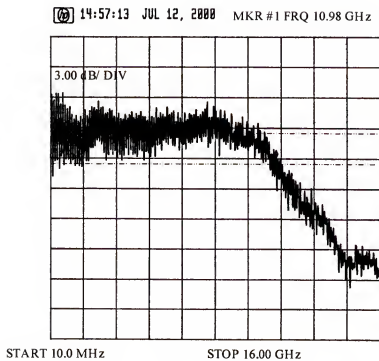
Figure 4-18 Small-signal frequency response for a multimode VCSEL of this work exhibiting greater than 10 GHz operation.
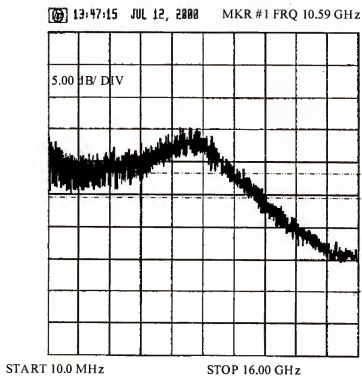
Figure 4-19 Small-signal frequency response for a single-mode VCSEL of this work exhibiting greater than 10 GHz operation.

laser threshold current. The MCEF is valid only for describing lasers modulated above threshold. From the equation it is obvious that a high value for the MCEF is desired. A high MCEF is accomplished by lasers with large 3 dB bandwidths and low threshold currents. To determine the MCEF for a laser, the 3 dB bandwidth of the laser is plotted versus $\sqrt{(I - I_{th})}$, and the slope of this plot is the MCEF.

Figures 4-20 and 4-21 show MCEF plots for a multimode and single-mode VCSELs of this work. The MCEFs are 3.97 $GHz/\sqrt{mA}$ for the multimode device and 6.59 $GHz/\sqrt{mA}$ for the single-mode device.

4.5 Large-Signal Analysis

Large-signal analysis is the more practical high-speed VCSEL characterization method, as compared to small-signal analysis, for determining the modulation bandwidth of VCSELs. This test determines how fast a VCSEL can transmit data over optical fiber and the rate for the number of errors it makes. The device is pre-biased at a current level where the VCSEL is lasing. A digital signal is applied to the DC bias to modulate the device. The signal from the VCSEL is transmitted over optical fiber into a bit-error rate tester where it is compared to the original digital signal for errors. The digital signal follows a pseudorandom bit sequence (PRBS) and simulates a real life practical data signal.
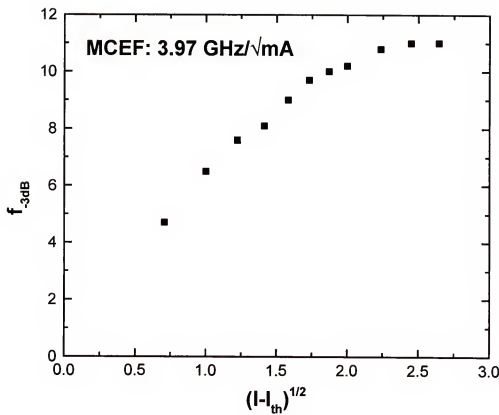
Figure 4-20 Modulation conversion efficiency factor plot for a multimode VCSEL of this work.
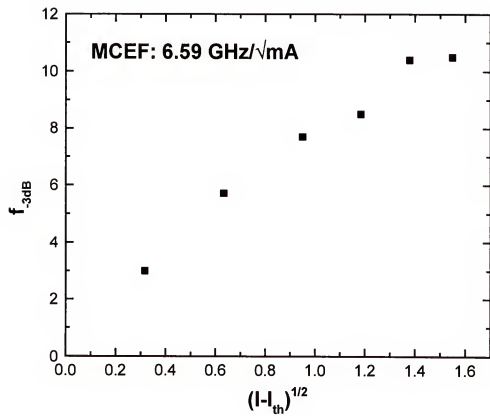
Figure 4-21 Modulation conversion efficiency factor plot for a single-mode VCSEL of this work.

Figure 4-22 shows a 10 Gbit/s eye diagram for a multimode VCSEL of this work using a pseudorandom bit sequence of 2^{31}-1. The eye diagram was obtained with a bias current of 6 mA, i.e. six times threshold. Bit error rates in the mid-10^{-10} range were obtained at 10Gbit/s. Using a PRBS of 2^{23}-1, the BER improved to <10^{-11}. Figure 4-23 shows a 10 Gbit/s eye diagram single-mode VCSEL of this work using a pseudorandom bit sequence of 2^{10}-1. The eye diagram was obtained with a bias current of 4 mA. Bit error rates in the low 10^{-10} range were obtained at 10Gbit/s. These large-signal analysis results were obtained using the same photodetector that was used for small-signal analysis, and thus are limited by the response of the photodetector.

Figure 4-24 shows an eye diagram for 11.5 Gbit/s operation of a multimode VCSEL of this work. A 12 GHz photodetector was used for these measurements. The transmission was over 300 m of Lucent's LazrSpeed multimode optical fiber and exhibited bit-error rates of less than 10^{-13} for a PRBS of 2^{31}-1.

The characteristics compare well with oxide–confined VCSELs and emphasize the promise of the shallow implant process for aperture formation.

10 Gbit/s
PRBS: $2^{31}-1$
BER~6×10^{-10}
6 mA

50.0 ps/div   47.0000 ns
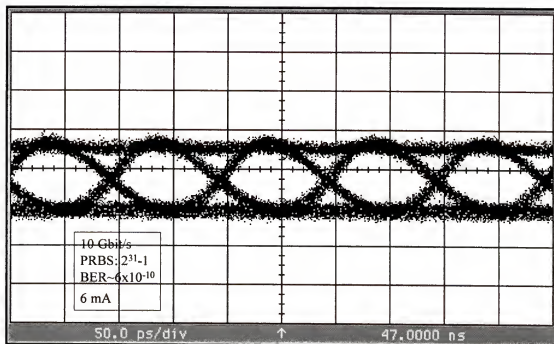
Figure 4-22 Eye diagram for a multi-mode VCSEL of this work operating at 10 Gbit/s.

10 Gbit/s
PRBS: 2^{10}-1
BER~2×10^{-10}
4 mA

50.0 ps/div ↑ 47.0000 ns
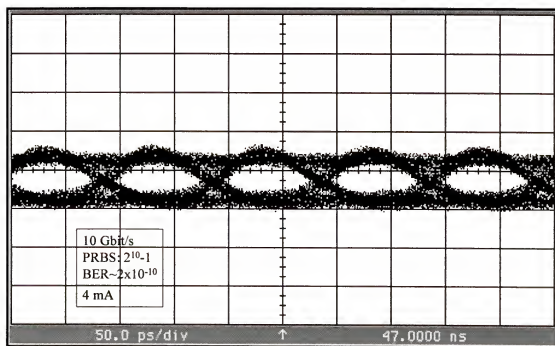
Figure 4-23 Eye diagram for a singlemode VCSEL of this work operating at 10 Gbit/s.
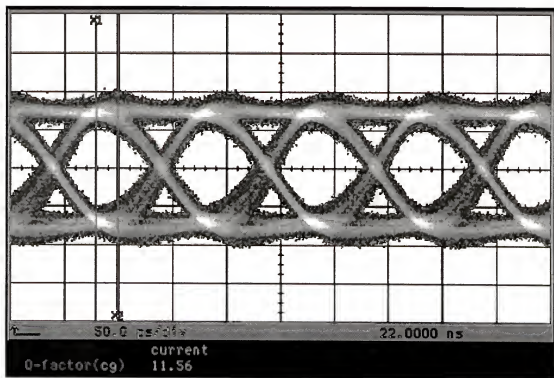
Figure 4-24 Eye diagram for a multi-mode VCSEL of this work operating at 11.5 Gbit/s over 300 m of Lucent's LazrSpeed optical fiber.

CHAPTER 5
TEMPERATURE ANALYSIS

5.1 Temperature Dependence Measurements

Short wavelength VCSELs have not had the self-heating problems that have impeded long wavelength VCSEL development because of the higher thermal conductivity materials used in short wavelength VCSELs. Device heating does play a significant role though in the performance of short wavelength VCSELs though. Temperature changes in the devices will lead to changes in the threshold current, slope efficiency, maximum output power, and the optical spectra.

Bonded 850 nm VCSELs with 15 micron apertures have shown to have thermal resistances between 1.170 and 1.240 K/mW.[30] The thermal resistance for unbonded 850 nm VCSELs were not reported and to the best of our knowledge have not been reported elsewhere. The following section details the temperature dependence characteristics of unbonded 850 nm VCSELs for this work.

5.1.1 Thermal Resistance Measurements

Thermal resistance measurements provide a way for estimating how much a device heats for increasing input electrical power. The thermal resistance of the device is determined by finding the wavelength shift of the device light output as a function of temperature and of input electrical power. To determine the output light wavelength shift as a function of temperature, a temperature-controlled chuck is used

to heat the device. Optical spectra are taken over a range of temperatures, and the wavelength position of the fundamental mode is tracked. To determine the output light wavelength shift as a function of input electrical drive power, fundamental mode wavelength position tracking is done with varying current. Input electrical power, P_e, is just the current-voltage product obtained from the IV characteristic obtained by a parameter analyzer. The following equation gives the thermal resistance of the device:

$$R_{Th} = \frac{\Delta T}{\Delta \lambda} \cdot \frac{\Delta \lambda}{\Delta P_e} \qquad \text{Equation 5-1}$$

The relationships between the shift in wavelength versus temperature and input electrical power are linear, as is shown in Figures 5-1 to 5-4 for multimode and single mode VCSELs of this work. The thermal resistances are 1.95 and 4.23 °C/mW for multimode and single-mode VCSELs, respectively. The higher thermal resistance of the single-mode VCSELs is expected because of their smaller apertures.

5.1.2 Characteristic Temperature

The characteristic temperature is an important characteristic of the VCSEL. It describes the dependence of the threshold current of the laser with respect to temperature. The threshold current is approximately modeled by:

$$I_{th} = I_0 e^{\frac{T}{T_0}} \qquad \text{Equation 5-2}$$

where I_{th} is the threshold current, I_0 is a constant with units of current, T is the heat chuck temperature, and T_0 is the characteristic temperature. By rearranging the
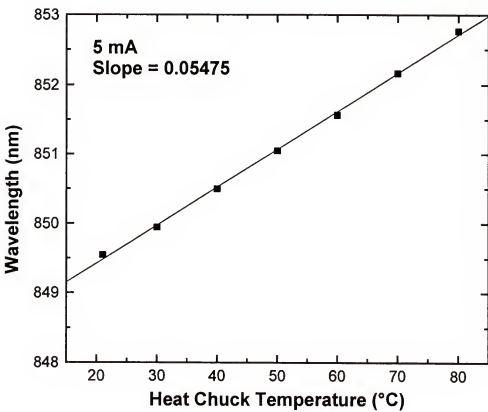
Figure 5-1 Fundamental mode wavelength versus heat chuck temperature plot for a multimode VCSEL of this work.
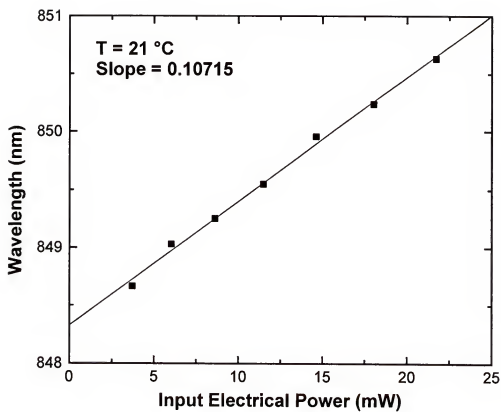
Figure 5-2 Fundamental mode wavelength versus input electrical power for a multimode VCSEL of this work.
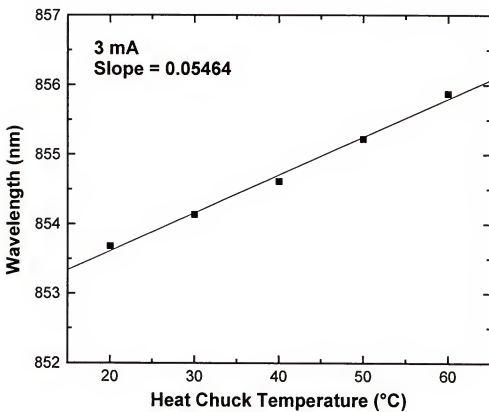
Figure 5-3 Fundamental mode wavelength versus heat chuck temperature plot for a single-mode VCSEL of this work.
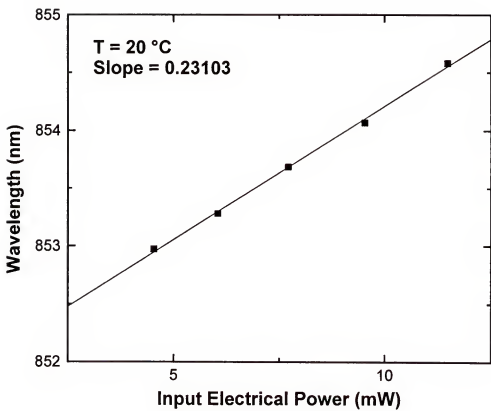
Figure 5-4 Fundamental mode wavelength versus input electrical power plot for a single-mode VCSEL of this work.

equation so that we have:

$$\ln I_{th} = \frac{T}{T_0} + \ln I_0 \qquad \text{Equation 5-3}$$

we see that a plot of $\ln I_{th}$ versus T will have a slope of $1/T_0$ and a y-intercept of $\ln I_0$. It can be seen that a large T_0 describes a laser with a lower dependence on temperature. Figure 5-5 shows a plot of $\ln I_{th}$ versus T for a multimode VCSEL of this work with a 7 μm diameter aperture. The characteristic temperature for that device is 77.88 °C. Figure 5-6 shows a plot for determining the characteristic temperature of a single-mode VCSEL of this work with a 4 μm diameter aperture. This device has a characteristic temperature of 47.08 °C, meaning the smaller diameter apertured VCSEL has a greater threshold current dependence on temperature. This is expected because the smaller aperture generates a higher current density and thus more heating. The VCSELs characteristic temperatures in comparison to edge-emitting lasers is also lower for the same reason. The edge-emitting lasers have a broad active region area that contributes to the generation of photons. Typical characteristic temperature values for edge-emitting lasers are between 100 and 200 °C for AlGaAs/GaAs laser diodes.

Figure 5-7 shows light output power-current-voltage characteristics over a temperature range of 20 to 80 °C in increments of 10 °C for a multimode VCSEL of this work. The LI curves exhibit decreasing maximum output power with increasing temperature. There is virtually no change in the IV characteristics of the VCSELs with increasing temperature. The maximum output power decreases from 1.65 to 0.35 mW over this temperature range. The decrease in the maximum output power is
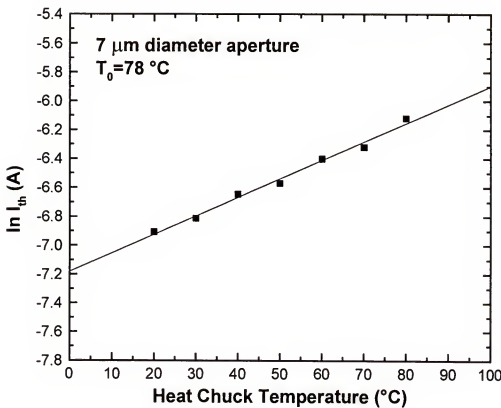
Figure 5-5 Characteristic temperature plot for a multimode VCSEL of this work.
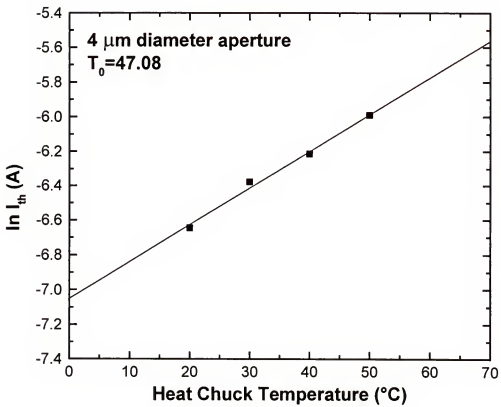
Figure 5-6 Characteristic temperature plot for a single-mode VCSEL of this work.
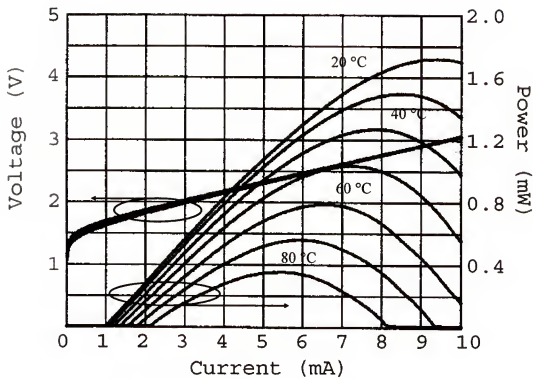
Figure 5-7 LIV plot for multimode VCSEL of this work over the temperature range of 20 °C to 80 °C.

due to the spectral misalignment between the cavity resonance and the gain curve. The effect of temperature on the maximum output power is more pronounced than on threshold current so a reduction in the slope efficiency is seen with increasing temperature, as shown in the plot of Figure 5-8. The slope efficiency of the devices decreases from 0.29 to 0.20 W/A as the temperature is increased from 20 to 80 °C. The decrease in slope efficiency with increasing temperature is approximated with a linear fit. Using the linear fit, the slope efficiency decreases -0.00152 °C^{-1}.

Figure 5-9 shows light output power-current-voltage characteristics over a temperature range of 20 to 50 °C in increments of 10 °C for a single-mode VCSEL of this work. The maximum output power decreases from 0.62 to 0.15 mW over this temperature range. The decrease in the maximum output power is due to the spectral misalignment between the cavity resonance and the gain curve. The effect of temperature on the maximum output power is more pronounced than on threshold current so a reduction in the slope efficiency is seen with increasing temperature, as shown in the plot of Figure 5-10. The slope efficiency of the devices decreases from 0.26 to 0.16 W/A as the temperature is increased from 20 to 50 °C. The slope efficiency decreases -0.00152 °C^{-1} using a linear fit.
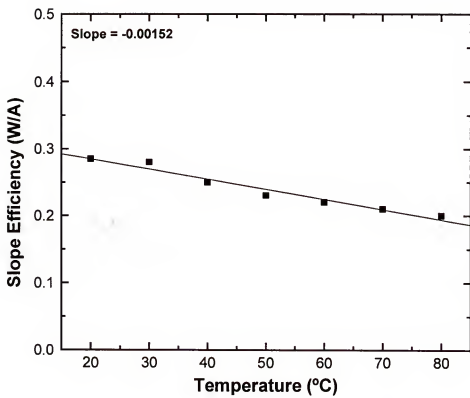
Figure 5-8 Plot of slope efficiency versus heat chuck temperature for a multimode VCSEL of this work.
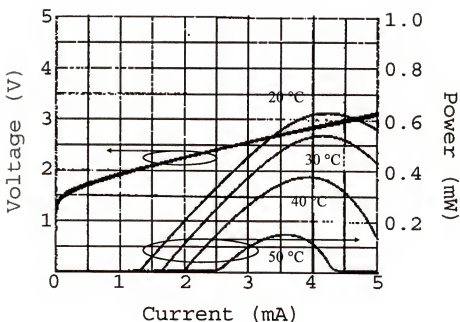
Figure 5-9 LIV plot for single-mode VCSEL of this work over the temperature range of 20 °C to 50 °C.
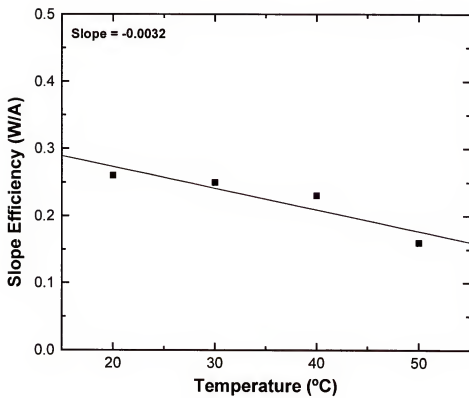
Figure 5-10 Plot of slope efficiency versus heat chuck temperature for a single-mode VCSEL of this work.

5.2 Finite Difference Analysis

Heating in the VCSEL leads to performance degradation and has been a hindrance in part to the development of long wavelength VCSELs. Because of the large current densities required for lasing in VCSELs, heating becomes more of an issue as compared to in-plane lasers. Heating leads to thermal rollover, or a degradation of the light output power as the drive current is increased in VCSELs. There are temperature dependent processes inside the VCSEL that lead to changes in the optical characteristics of the devices. These include changes in the bandgap energy and the index of refraction of the materials of the devices with changes in temperature.

There has been a lot of work done on the thermal analysis of semiconductor lasers. The range of the work that has been done ranges from being very simple to very elaborate models. Coldren et al. gives a very simple relation for estimating the temperature rise in VCSELs[31]. The temperature rise in the operating device is:

$$\Delta T = P_D Z_T \qquad \text{Equation 5-4}$$

where P_D is the dissipated power in the laser and Z_T is the thermal impedance. The power dissipated in the laser is:

$$P_D = P_e - P_{out} = P_e[1 - \eta] \qquad \text{Equation 5-5}$$

where P_{out} is the power emitted from the laser and η is the wall-plug efficiency, which is just the ratio of the light output power to the input electrical power.

The thermal impedance is estimated for heat generated in a disk source with diameter d in a VCSEL on top of a thick substrate using the relation:

$$Z_T \approx \frac{1}{2kd} \qquad \text{Equation 5-6}$$

where k is thermal conductivity. The heat generation source in a VCSEL with a circular aperture will have a disk shape, because the active region layers are very thin compared to the diameter of the aperture.

Kobayashi et al. examined the temperature distributions in GaAs-AlGaAs double heterostructure lasers.[32] The authors were interested in examining the temperature distribution in the double heterostructure laser below and above the threshold current of the laser. Device temperature distributions were measured experimentally using a Thermal Plotter and compared to a theoretical model. The model that the authors use include heat generation from absorption, non-radiative recombination, and Joule heating. For operation above threshold, heating in the active region is equal to:

$$V_b(I - I_{th})(\eta_i - \eta_{ext}) + V_b I_{th}\eta_{spon}(1-f) +$$
$$V_b(I - I_{th})(1-f)\eta' \eta_{spon} + V_b I_{th}(1-\eta_{spon}) + \qquad \text{Equation 5-7}$$
$$V_b(I - I_{th})(1-\eta_{spon})\eta'$$

where V_b is the junction voltage, η_{spon} and η_{ext} are the internal quantum efficiency of the spontaneous emission and the external differential quantum efficiency of the lasing, respectively. η_i is the internal efficiency of the lasing and $\eta'=1- \eta_i$. Joule heating simply follows the equation $I^2 R_s$, where R_s is the device series resistance. The variable f is the fraction of the spontaneous emission from the active region absorbed in the device. This fraction is approximated by the authors using the relation:

$$f = 1 - \sqrt{1 - (n_1/n_0)^2} \qquad \text{Equation 5-8}$$

where n_0 and n_1 are the refractive indices of the active region and the clad layers, respectively.

The temperature distribution is then determined using the continuity equation for heat flow:

$$\nabla \cdot (K \nabla \Delta T) = -Q \qquad \text{Equation 5-9}$$

where K is the thermal conductivity of the semiconductor material, T is temperature, and Q is the heat generation.

Using this method requires knowledge of factors that require extensive experiments to determine, in particular the η efficiency terms. The authors used approximations for these efficiency factors to validate the theoretical model.

An alternative to determining the η efficiency terms is to take current-voltage measurements of the VCSEL, and estimating the heat generation in the active region from:

$$P_e = I^2 R_S + IV_b + IV_s \qquad \text{Equation 5-10}$$

where P_e is the electrical input power, I is the current, R_s is the series resistance of the device, V_b is the ideal diode voltage of the device, V_d is the series voltage in the device due to material band offsets, and P_{out} is the power of the light emitted from the device.

The ideal diode voltage is the voltage at which the diode current "turns-on". When a diode is forward biased, there initially is a blocking voltage that prevents current conduction. At a critical voltage, the diode can no longer support the current blocking and the device begins to conduct current. This critical voltage in an ideal case is known as the ideal diode voltage. The ideal diode voltage can be approximated as:

$$V_i = \frac{E_g}{q}$$
<div align="right">Equation 5-11</div>

where E_g is the band gap energy of the active layers and q is the fundamental electronic charge. To calculate the ideal diode voltage for the VCSELs being examined, we use the bandgap energy of GaAs, which is 1.42 eV, since the majority of the recombinations take place in the GaAs quantum well layers. Converting this into Joules, we get 2.275E-19 J and dividing by 1.602E-19 C for q, the ideal diode voltage is 1.42 V. This agrees well with the current "turn-on" voltage observed from experimental IV characteristics of the devices.

The series voltage in Equation 5-10 can be neglected if their aren't numerous band offsets between varying semiconductor layers that can create potential barriers for current to conduct, as is the case for contacts formed on semiconductor DBRs, and the device epitaxy structure doesn't contain materials with widely varying energy bandgaps. The temperature profile of a lasing VCSEL can be obtained using a finite-difference analysis. Results from the simulation for the VCSELs of this work are in good agreement with experimental thermal resistance measurements on the devices.

A three-dimensional finite-difference simulation was used for obtaining the temperature profile of the operating VCSEL. The device was separated into regions that will be able to account for varying characteristics in the structure, i.e., active region heating, changes in thermal conductivity, etc. Cylindrical coordinates were used to generate the mesh of the device. Figure 5-11 shows the geometry and the cylindrical coordinate axes of the VCSEL device used for the finite-difference temperature analysis. Because of the symmetry of the device, there is no azimuthal
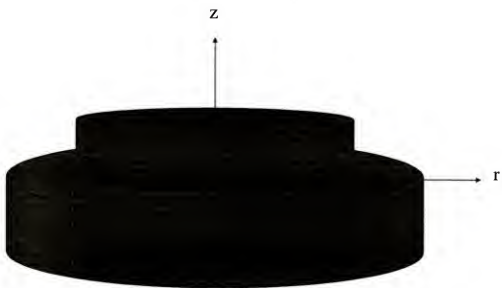
Figure 5-11 Schematic showing the geometry and cylindrical coordinate axes for finite-difference temperature analysis of the VCSEL devices of this work.

dependence of the temperature profile and so the device is divided into regions that will contain an inner cylindrical core, surrounded by rings as shown in Figures 5-12 to 5-14. The size of the inner core is chosen to be the size of the device aperture. This will simulate the heating of the aperture region in the active layers. More nodes are used in the active region area of the device to improve the temperature profile resolution in this region. The active region in the device has alternating GaAs and AlGaAs layers that form the quantum wells of the VCSEL. The thicknesses of the nodes in the active region are chosen to be the same as the actual thicknesses of the GaAs and AlGaAs layers to show detail in the temperature profile in this region.

Each of the regions has a thermal resistance element that depends on the geometry and thermal conductivity of the region. The thermal resistance of each of the regions will determine how heat is dissipated in the device and ultimately give a steady-state temperature profile of the device.

The steady-state temperature profile in the VCSEL can be determined by treating the heat flow in the structure as being subjected to resistances between nodes.[33] If we designate the node of interest with the subscript i and adjoining nodes with the subscript j, the general heat flow system subjected to resistances is illustrated in Figure 5-15. At steady state the net heat input into node i is:

$$q_i + \sum_j \frac{T_j - T_i}{R_{ij}} = 0 \qquad \text{Equation 5-12}$$

where q_i is the heat generated in node i, T is the temperature of the node, and R_{ij} is the resistance element between nodes i and j.
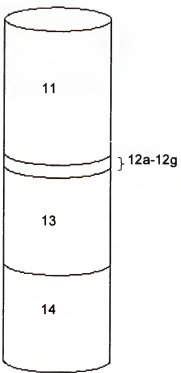
Figure 5-12 Schematic of the inner core of the VCSEL system used in the finite-difference temperature analysis.
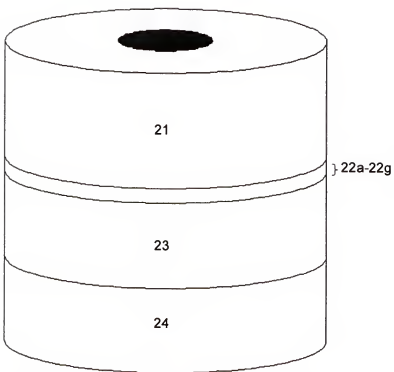
Figure 5-13 Schematic of the cladding to the inner core of the VCSEL system used in the finite-difference temperature analysis.
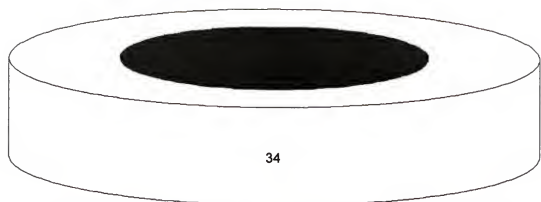
Figure 5-14 Schematic of the cladding to node 24 of the VCSEL system used in the finite-difference temperature analysis.
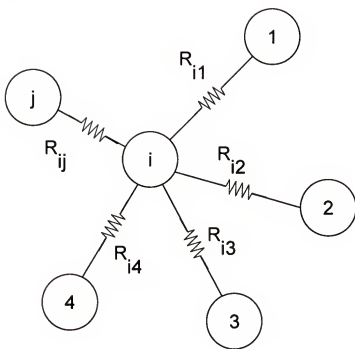
Figure 5-15 Schematic showing the general heat flow system for finite-difference temperature analysis.

We choose a cylindrical coordinate system for generating the mesh of the VCSEL device. The VCSEL devices are symmetric along the z-axis. Temperature varies only along the z and radial direction. The resistance elements between nodes have units of K/mW. Because there is no azimuthal dependence of temperature in the VCSEL, the nodes are connected only in the radial and axial direction. It is convenient to now define the variable r_m as:

$$r_m = \frac{r_o + r_i}{2}$$ Equation 5-13

where r_0 and r_i are the outer and inner radii of the node. For resistance elements between nodes above and below each other in the z direction:

$$R_z = \frac{\Delta z}{r_m \Delta \phi \Delta r k}$$ Equation 5-14

where the Δ terms are from the center of node i to the center of the adjacent node j and k is the thermal conductivity of the material. For nodes that had different thermal conductivities, an average was taken between the two thermal conductivities and weighted by their thicknesses. This is written as:

$$k_{avg} = \frac{k_1 t_1 + k_2 t_2}{t_1 + t_2}$$ Equation 5-15

where t is the thickness of node 1 or 2. For example, the average thermal conductivity used for the resistance element between a node 200 Å thick with k_1=4e-2 $\frac{mW}{\mu m - K}$ and a node 100 Å thick with k_2=2e-2 $\frac{mW}{\mu m - K}$ would be:

$$k_{avg} = \frac{8e-4\dfrac{mW}{K} + 2e-4\dfrac{mW}{K}}{3e-2\mu m}$$

$$= 3.33e-2\frac{mW}{\mu m - K}$$

<div align="right">Equation 5-16</div>

For resistance elements adjacent to nodes in the radial direction with $r_{m,j} < r_{m,i}$:

$$R_{r-} = \frac{\Delta r}{(r_m - \Delta r/2)\Delta\phi\Delta z k}$$

<div align="right">Equation 5-17</div>

For resistance elements adjacent to nodes in the radial direction with $r_{m,i} < r_{m,j}$:

$$R_{r+} = \frac{\Delta r}{(r_m + \Delta r/2)\Delta\phi\Delta z k}$$

<div align="right">Equation 5-18</div>

For nodes that border convection surfaces the resistance element is:

$$R_{conv} = \frac{1}{hA}$$

<div align="right">Equation 5-19</div>

where h is the convection coefficient and A is the area of the convection surface. For the analysis of this work, we assume that convection surfaces are subjected to free convection and it is assumed that the convection coefficient is equal to 1e-8 $\dfrac{mW}{\mu m^2 - K}$. The ambient temperature of the convection environment is taken to be 298 K.

Using Equation 5-12 a series of linear equations are generated for each node. The solution to the linear set of equations can be solved using linear algebra. It should be noted that the finite-difference method becomes increasingly more accurate with an increasing number of nodes in the system. Increasing the number of nodes in the system increases the number of equations that need to be generated and thus the complexity of the problem. One consolation is that the equations generated when put

into matrices form will contain many zeroes. The equations generated will have the form:

$$a_{11,1}T_{11} + a_{12,1}T_{12} + \cdots + a_{kl,1}T_{kl} = C_{11}$$
$$a_{11,2}T_{11} + a_{12,2}T_{12} + \cdots + a_{kl,2}T_{kl} = C_{12}$$
$$a_{11,3}T_{11} + a_{12,3}T_{12} + \cdots + a_{kl,3}T_{kl} = C_{13} \qquad \text{Equation 5-20}$$
$$\vdots \qquad \vdots \qquad \qquad \vdots \;\; = \;\; \vdots$$
$$a_{11,n}T_{11} + a_{12,n}T_{12} + \cdots + a_{kl,n}T_{kl} = C_{kl}$$

where a and C values are constants, and n is the number of nodes in the system. The subscripts kl are simply index labels for the nodes, and thus T_{kl} is the temperature of node kl. The values for the constants a will be equal to values or combinations of values of the resistance elements. For the characteristic equation written for the node of interest, node kl, the coefficient for T_{kl} is:

$$a_{kl} = -\sum \frac{1}{R_{ij}} \qquad \text{Equation 5-21}$$

where R_{ij} is the resistance element between the node of interest and its surrounding borders, be it another node, a convection environment or a heat sink. The system is approximated as being surrounded by a heat sink in the n-radial conduction layer area. The region bordering the n-radial conduction region is considered to be 298 K. This assumption isn't a bad assumption because the area of the wafer is much larger than the area of the device. The coefficient for all other nodal temperatures in the same characteristic equation is:

$$a_{kl} = \frac{1}{R_{ij}} \qquad \text{Equation 5-22}$$

The values for the C constants depend on the heat generation in the node of interest and whether the node of interest has a surface exposed to convection. For no heat generation in the node and no surfaces exposed to convection or a heat sink:

$$C_{kl} = 0 \qquad \text{Equation 5-23}$$

For a node with heat generation and no surface exposed to convection or to a heat sink:

$$C_{kl} = -q \qquad \text{Equation 5-24}$$

For a node with heat generation and surfaces exposed to convection or to a heat sink:

$$C_{kl} = -\left(q + T_{amb} \cdot \sum \frac{1}{R_{ij}} \right) \qquad \text{Equation 5-25}$$

where q is the total heat generation in the node, T_{amb} is the temperature of the surrounding convection environment or heat sink, and the resistance element terms are between the node of interest and the convection or heat sink environment.

Putting the linear set of equations into matrix notation, we have the matrix:

$$[A] = \begin{bmatrix} a_{11,1} & a_{12,1} & \cdots & a_{kl,1} \\ a_{11,2} & a_{12,2} & \cdots & a_{kl,2} \\ a_{11,3} & a_{12,3} & \cdots & a_{kl,3} \\ \vdots & \vdots & \ddots & \vdots \\ a_{11,n} & a_{12,n} & \cdots & a_{kl,n} \end{bmatrix} \qquad \text{Equation 5-26}$$

We can also write:

$$[T] = \begin{bmatrix} T_{11} \\ T_{12} \\ T_{13} \\ \vdots \\ T_{kl} \end{bmatrix} \qquad \text{Equation 5-27}$$

and:

$$[C] = \begin{bmatrix} C_{11} \\ C_{12} \\ C_{13} \\ \vdots \\ C_{kl} \end{bmatrix} \qquad \text{Equation 5-28}$$

The linear set of equations can be expressed as:

$$[A][T] = [C] \qquad \text{Equation 5-29}$$

Obtaining the inverse of matrix A and multiplying it by matrix C will give the solution to the nodal temperatures, or:

$$[T] = [A]^{-1}[C] \qquad \text{Equation 5-30}$$

Heat generation due to Joule heating throughout the semiconductor layers and in the contacts of the device and non-radiative recombination and absorption in the active region is accounted for in the simulation. Joule heating in the device is determined using the following well-known expression:

$$Q = I^2 R \qquad \text{Equation 5-31}$$

where I is device drive current and R is the resistance. Joule heating in each of the layers of the device can be determined for a specified drive current. The resistance of the semiconductor layers and contact resistance were determined using the transmission line method and theoretical methods discussed in Section 4.3.

Heating in the active region of the device requires knowledge of how efficient the VCSEL is at converting electrical power into optical power. Non-radiative recombination in the VCSEL generates heat in the active region and since the active region is absorbing, heat is generated from optical absorption as well.

The total input power of the VCSEL can be determined by the IV product obtained from current-voltage measurements. This total input power is dissipated in the device either through heat generation or radiatively through light emission.

The amount of heat generated in the active region can be estimated from equation 5-10. If we assume that the series voltage is negligible, which is not a bad assumption for VCSEL of this work, since intracavity contacts are used and the materials of the laser cavity don't vary significantly in bandgap energy, we are left with:

$$P_e = I^2 R_S + IV_b \qquad \text{Equation 5-31}$$

The first term on the right hand side of equation 5-31 will be from resistance in the semiconductor layers and the heating in the active region will be approximately:

$$Q_{gen,act} = IV_b - P_{out} \qquad \text{Equation 5-32}$$

For a multimode VCSEL of this work at 9.5 mA drive current:

$$Q_{gen,act} = 9.5\,\text{mA} \cdot 1.42\,\text{V} - 2.1\,\text{mW} = 11.4\,\text{mW} \qquad \text{Equation 5-33}$$

A linear set of equations was generated for analysis of a multimode VCSEL of this work using Equations 5-12 and the heat generation terms calculated using the methods of this section. The matrices for the finite-difference temperature analysis are shown in Figures 5-16 to 5-19. Visual Basic was used to generate the matrices. The Visual Basic code for performing finite-difference temperature analysis on the VCSELs of this work is listed in Appendix A. Figure 5-20 shows the temperature solutions for each of the nodes. The maximum temperature is 344.9 K, which is in good agreement with the 354 K temperature obtained from the thermal resistance determined from the previous section.

$$A=$$

-0.54	0.53	0.00	0.00	0.00	0.00	0.00	0.00	0.00	0.00	0.00	0.00	0.00	0.00	0.00	0.00	0.00	0.00	0.00	0.00	0.00	0.00	0.00
0.53	-39.16	38.63	38.63	0.00	0.00	0.00	0.00	0.00	0.00	0.00	0.00	0.00	0.00	0.00	0.00	0.00	0.00	0.00	0.00	0.00	0.00	0.00
0.00	38.63	-77.26	0.00	38.63	0.00	0.00	0.00	0.00	0.00	0.00	0.00	0.00	0.00	0.00	0.00	0.00	0.00	0.00	0.00	0.00	0.00	0.00
0.00	38.63	38.63	-77.26	0.00	38.63	0.00	0.00	0.00	0.00	0.00	0.00	0.00	0.00	0.00	0.00	0.00	0.00	0.00	0.00	0.00	0.00	0.00
0.00	0.00	38.63	0.00	-77.26	0.00	38.63	0.00	0.00	0.00	0.00	0.00	0.00	0.00	0.00	0.00	0.00	0.00	0.00	0.00	0.00	0.00	0.00
0.00	0.00	0.00	38.63	0.00	-77.26	38.63	0.00	0.00	0.00	0.00	0.00	0.00	0.00	0.00	0.00	0.00	0.00	0.00	0.00	0.00	0.00	0.00
0.00	0.00	0.00	0.00	38.63	38.63	-40.15	1.52	-2.61	1.09	0.00	0.00	0.00	0.00	0.00	0.00	0.00	0.00	0.00	0.00	0.00	0.00	0.00
0.00	0.00	0.00	0.00	0.00	0.00	1.52	-2.61	1.09	1.52	0.00	0.00	0.00	0.00	0.00	0.00	0.00	0.00	0.00	0.00	0.00	0.00	0.00
0.00	0.00	0.00	0.00	0.00	0.00	0.00	1.09	-3.73	0.00	-12.72	12.71	0.00	0.00	0.00	0.00	0.00	0.00	0.00	0.00	0.00	0.00	0.00
0.00	0.00	0.00	0.00	0.00	0.00	0.00	0.00	0.01	0.00	12.71	-939.83	12.71	0.00	0.00	0.00	0.00	0.00	0.00	0.00	0.00	0.00	0.00
0.00	0.00	0.00	0.00	0.00	0.00	0.00	0.00	0.00	0.00	939.83	12.71	-939.83	927.12	0.00	0.00	0.00	0.00	0.00	0.00	0.00	0.00	0.00
0.00	0.00	0.00	0.00	0.00	0.00	0.00	0.00	0.00	0.00	12.71	927.12	927.12	-1854.24	927.12	0.00	0.00	0.00	0.00	0.00	0.00	0.00	0.00
0.00	0.00	0.00	0.00	0.00	0.00	0.00	0.00	0.00	0.00	0.00	-1854.24	-1854.24	927.12	-1854.24	927.12	0.00	0.00	0.00	0.00	0.00	0.00	0.00
0.00	0.00	0.00	0.00	0.00	0.00	0.00	0.00	0.00	0.00	0.00	927.12	927.12	927.12	927.12	-1854.24	927.12	0.00	0.00	0.00	0.00	0.00	0.00
0.00	0.00	0.00	0.00	0.00	0.00	0.00	0.00	0.00	0.00	0.00	0.00	0.00	-1854.24	927.12	927.12	-1854.24	927.12	0.00	0.00	0.00	0.00	0.00
0.00	0.00	0.00	0.00	0.00	0.00	0.00	0.00	0.00	0.00	0.00	0.00	0.00	927.12	927.12	927.12	927.12	-1854.24	927.12	0.00	0.00	0.00	0.00
0.00	0.00	0.00	0.00	0.00	0.00	0.00	0.00	0.00	0.00	0.00	0.00	0.00	0.00	0.00	0.00	927.12	927.12	-870.85	834.41	0.00	0.00	0.00
0.00	0.00	0.00	0.00	0.00	0.00	0.00	0.00	0.00	0.00	0.00	0.00	0.00	0.00	0.00	0.00	0.00	-1854.24	-870.85	-854.24	36.44	0.00	0.00
0.00	0.00	0.00	0.00	0.00	0.00	0.00	0.00	0.00	0.00	0.00	0.00	0.00	0.00	0.00	0.00	0.00	927.12	834.41	36.44	-42.53	26.08	0.00
0.00	0.00	0.00	0.00	0.00	0.00	0.00	0.00	0.00	0.00	0.00	0.00	0.00	0.00	0.00	0.00	0.00	0.00	0.00	-42.53	26.08	-89.35	0.03
0.00	0.00	0.00	0.00	0.00	0.00	0.00	0.00	0.00	0.00	0.00	0.00	0.00	0.00	0.00	0.00	0.00	0.00	0.00	0.00	26.08	0.03	82.48

Figure 5-16 Matrix A for finite-difference temperature analysis

$$T = \begin{matrix} T11 \\ T12a \\ T12b \\ T12c \\ T12d \\ T12e \\ T12f \\ T12g \\ T13 \\ T14 \\ T21 \\ T22a \\ T22b \\ T22c \\ T22d \\ T22e \\ T22f \\ T22g \\ T23 \\ T24 \\ T34 \end{matrix}$$

Figure 5-17 Matrix T for finite-difference temperature analysis.

$$C = \begin{matrix} -6.50 \\ 0.00 \\ -3.80 \\ 0.00 \\ -3.80 \\ 0.00 \\ -3.80 \\ 0.00 \\ 0.00 \\ -785.09 \\ -6.60 \\ 0.00 \\ 0.00 \\ 0.00 \\ 0.00 \\ 0.00 \\ 0.00 \\ 0.00 \\ -3.25 \\ -18845.53 \\ -24580.11 \end{matrix}$$

Figure 5-18 Matrix C for finite-difference temperature analysis.

$$A^{-1} =$$

-3.81	-2.01	-1.99	-1.96	-1.94	-1.91	-1.89	-1.86	-1.24	-0.37	0.00	0.00	0.00	0.00	0.00	0.00	0.00	0.00	0.00
-2.00	-2.05	-2.02	-2.01	-1.97	-1.95	-1.92	-1.90	-1.26	-0.37	0.00	0.00	0.00	0.00	0.00	0.00	0.00	0.00	0.00
-1.95	-2.02	-2.02	-2.00	-1.97	-1.95	-1.92	-1.90	-1.26	-0.37	0.00	0.00	0.00	0.00	0.00	0.00	0.00	0.00	0.00
-1.93	-1.97	-2.00	-2.00	-1.97	-1.95	-1.92	-1.90	-1.26	-0.37	0.00	0.00	0.00	0.00	0.00	0.00	0.00	0.00	0.00
-1.90	-1.97	-1.97	-1.97	-1.97	-1.95	-1.92	-1.90	-1.26	-0.37	0.00	0.00	0.00	0.00	0.00	0.00	0.00	0.00	0.00
-1.88	-1.97	-1.95	-1.95	-1.95	-1.95	-1.92	-1.90	-1.26	-0.37	0.00	0.00	0.00	0.00	0.00	0.00	0.00	0.00	0.00
-1.86	-1.92	-1.92	-1.92	-1.92	-1.92	-1.92	-1.90	-1.26	-0.37	0.00	0.00	0.00	0.00	0.00	0.00	0.00	0.00	0.00
-1.85	-1.90	-1.90	-1.90	-1.90	-1.90	-1.90	-1.90	-1.26	-0.37	0.00	0.00	0.00	0.00	0.00	0.00	0.00	0.00	0.00
1.23	1.28	1.28	1.26	1.26	1.25	1.28	1.26	1.27	0.37	0.00	0.00	0.00	0.00	0.00	0.00	0.00	0.00	0.00
0.38	0.37	0.37	0.37	0.37	0.37	0.37	0.37	0.37	0.38	0.00	0.00	0.00	0.00	0.00	0.00	0.00	0.00	0.00
-0.01	0.00	0.00	0.00	0.00	0.00	0.00	0.00	0.00	0.00	-0.16	-0.08	-0.08	-0.08	-0.08	-0.08	-0.08	-0.07	0.00
0.00	0.00	0.00	0.00	0.00	0.00	0.00	0.00	0.00	0.00	-0.08	-0.08	-0.08	-0.08	-0.08	-0.08	-0.07	-0.07	-0.02
0.00	0.00	0.00	0.00	0.00	0.00	0.00	0.00	0.00	0.00	-0.08	-0.08	-0.08	-0.08	-0.08	-0.08	-0.07	-0.05	-0.02
0.00	0.00	0.00	0.00	0.00	0.00	0.00	0.00	0.00	0.00	-0.08	-0.08	-0.08	-0.08	-0.08	-0.08	-0.07	-0.05	-0.02
0.00	0.00	0.00	0.00	0.00	0.00	0.00	0.00	0.00	0.00	-0.08	-0.08	-0.08	-0.08	-0.08	-0.08	-0.07	-0.05	-0.02
0.00	0.00	0.00	0.00	0.00	0.00	0.00	0.00	0.00	0.00	-0.08	-0.08	-0.08	-0.08	-0.08	-0.08	-0.07	-0.05	-0.02
0.00	0.00	0.00	0.00	0.00	0.00	0.00	0.00	0.00	0.00	-0.07	-0.07	-0.07	-0.07	-0.07	-0.07	-0.07	-0.05	-0.02
0.00	0.00	0.00	0.00	0.00	0.00	0.00	0.00	0.00	0.00	-0.05	-0.05	-0.05	-0.05	-0.05	-0.05	-0.05	-0.05	-0.02
0.00	0.00	0.00	0.00	0.00	0.00	0.00	0.00	0.00	0.00	0.01	0.01	0.01	0.01	0.01	0.01	0.01	0.01	0.00
0.00	0.00	0.00	0.00	0.00	0.00	0.00	0.00	0.00	0.00	0.00	0.00	0.00	0.00	0.00	0.00	0.00	0.00	-0.01

Figure 5.19 Inverse of matrix A for finite-difference temperature analysis

T11	=	344.90
T12a	=	333.52
T12b	=	333.37
T12c	=	333.11
T12d	=	332.86
T12e	=	332.51
T12f	=	332.16
T12g	=	331.71
T13	=	320.33
T14	=	304.51
T21	=	299.38
T22a	=	298.81
T22b	=	298.81
T22c	=	298.80
T22d	=	298.79
T22e	=	298.78
T22f	=	298.78
T22g	=	298.77
T23	=	298.59
T24	=	298.21
T34	=	298.13

Figure 5-20 Solution matrix for nodal temperatures.

CHAPTER 6
OPTICAL MODEL

The generation of photons in a VCSEL takes place in its active region, and is a phenomena that involves radiative electron-hole pair recombination. Electron-hole recombination can be either non-radiative or radiative. Only radiative recombination creates photons. The following sections discuss the rate equations involved and an analysis of what is necessary for photon generation and lasing in VCSELs.

6.1 Carrier Rate Equation

The rate of carrier generation in the active region of the VCSEL can generically be written as:[34]

$$\frac{dN}{dt} = N_{gen} - R_{rec} \qquad \text{Equation 6-1}$$

where N is the carrier density [carriers/cm^3], t is time [seconds], N_{gen} is the number of carriers generated in the active region, and R_{rec} the number of carriers recombining in the active region. Since there will be current leakage mechanisms that will prevent all of the current from flowing into the active region, the leakage has to be accounted for, and so will be included in the N_{gen} term. To correct for the leakage current, an internal quantum efficiency term is used, η_i, which is the fraction of the total current in the device that flows in the active region. The total number of carriers in the device is the current I divided by the fundamental electronic charge, q. To get the

expression for the carrier density in the active region when current is flowing in the device, we multiply by η_i, and divide by the volume of the active region, V. We have:

$$N_{gen} = \frac{\eta_i I}{qV}$$ Equation 6-2

A number of recombination processes contribute to the total recombination term of Equation 6-1. We need to include four mechanisms. They are spontaneous recombination, non-radiative recombination, carrier leakage in the active region, and stimulated recombination.

Spontaneous recombination contributes to the generation of photons, but spontaneous recombination occurs prior to carrier population inversion in the active region, so that there is no lasing action in the device. This region is below threshold for the device and the optical spectra of light emission due to spontaneous recombination is incoherent and broad. The light is incoherent because electron-hole recombination is occurring randomly through many processes including band to impurity level, impurity level to band, and impurity level to impurity level transistions.

Non-radiative recombination does not contribute to photon generation. These recombination processes include direct recombination of electrons and holes from the conduction and valence bands that do not generate photons as well as recombination through recombination centers in energy levels between the conduction and valence bands. Non-radiative recombination leads to phonon generation, which is dissipated as heat in the semiconductor crystal.

Carrier leakage is not a recombination mechanism per se, but serves to reduce the number of carriers in the active region that can lead to photon generation. In this sense it is similar to non-radiative recombination, but the mechanism is different. Carrier leakage in the active region is primarily due to potential barriers not being large enough in the cladding layers of the active region. Carriers that aren't sufficiently confined by the potential barriers of the higher bandgap material of the cladding layers contribute to carrier leakage.

Stimulated recombination takes place with the generation of photons. This region on the light output-current curve is after the device has reached threshold. Carrier population inversion has been attained above threshold and photons in the active region interact with electrons relaxing from the conduction band to the valence band so that light emission is in the same phase and frequency as the incident photons. This phenomenon explains the coherent nature of light emitting from the laser above threshold and gain of the incident light created.

The first three recombination processes, spontaneous recombination, non-radiative recombination, and carrier leakage take place regardless of whether photons are present or not. These processes can be grouped together and their decay can be described by a time constant, τ. The rate of carriers decaying by any of these three processes can then be written as, N/τ. The carrier rate equation in the active region of the laser is now:

$$\frac{dN}{dt} = \frac{\eta_i I}{qV} - \frac{N}{\tau} - R_{stim} \qquad \text{Equation 6-3}$$

It remains for R_{stim} to be evaluated. Stimulated recombination takes place in the presence of incident photons and some type of pump to create population

inversion in the active region, be it optically or electrically. This phenomenon amplifies light in the active region of the laser. For a photon density, N_p, incident on a gain region of short length Δz, the photon density is amplified, so that the increase in the photon density is, ΔN_p. In actuality, the gain of photons increases exponentially along length Δz so that:

$$N_p + \Delta N_p = N_p e^{g\Delta z} \qquad \text{Equation 6-4}$$

where g is the gain per unit length in the active regions. But for small Δz, the exponential term can be approximated as:

$$e^{g\Delta z} \cong 1 + g\Delta z \qquad \text{Equation 6-5}$$

Also, recognizing that:

$$\Delta z = v_g \Delta t \qquad \text{Equation 6-6}$$

where v_g is the group velocity of the light in the active region, we can obtain an expression for the photon gain:

$$\Delta N_p = N_p g v_g \Delta t \qquad \text{Equation 6-7}$$

The group velocity is used because the photons in the active region will have a range of different frequencies. To relate this to the stimulated recombination rate, we write:

$$\frac{\Delta N_p}{\Delta t} = R_{stim} \qquad \text{Equation 6-8}$$

This is true because electrons recombining for stimulated emission will be equal to the number of photons generated due to stimulated emission. Therefore,

$$R_{stim} = v_g g N_p \qquad \text{Equation 6-9}$$

The final form of the carrier density rate equation can be written as:

$$\frac{dN}{dt} = \frac{\eta_i I}{qV} - \frac{N}{\tau} - v_g g N_p \qquad \text{Equation 6-10}$$

6.2 Photon Density Rate Equation

A similar treatment to the carrier density rate equation can be applied for photons in the cavity of the laser for the lasing mode:

$$\frac{dN_p}{dt} = N_{p,gen} - N_{p,loss} \qquad \text{Equation 6-11}$$

where N_p is the photon density in the laser cavity, and the two terms on the right hand side of the equation represent the photon generation and loss.

It is useful to define the confinement factor for photons, Γ. The confinement factor, in a general sense, is the ratio between the *active* region volume occupied by electrons to the *cavity* volume occupied by photons. Gain material does not completely fill the optical cavity volume, so to calculate the number of photons generated in the cavity volume the confinement factor is used. To determine this value accurately requires a rigorous examination of the properties and structure of the laser cavity, so that waveguide analysis can be performed for calculation of the mode overlap with the active layers of the cavity. The actual confinement factor may differ by a factor of 2 for active region lengths less that or equal to the wavelength of the mode of interest. With the definition for the photon confinement factor, the photon density generation due to stimulated emission in the laser cavity is then:

$$N_{p,stim} = \Gamma R_{stim} \qquad \text{Equation 6-12}$$

There is also a photon density generation contribution from spontaneous emission as well. For stimulated emission, we assume that the majority of the photons generated are of the same mode due to the coherent nature of the light from stimulated emission, but the case is not true for spontaneous emission. To evaluate the contribution of the photon density generation due to spontaneous emission, we have to use a correction factor for determining the amount of photons due to spontaneous emission that contributes to the mode of interest. We call this factor the spontaneous emission factor, β_{spon}, and multiply this by the confinement factor and the spontaneous recombination rate to get:

$$N_{p,spon} = \beta_{spon} \Gamma R_{spon}$$
Equation 6-13

The spontaneous emission factor is simply the inverse of the number of modes present in the spectral bandwidth of the spontaneous emission if we assume that all modes are coupled evenly or that the same number of photons contribute to each mode evenly to reduce complexity.

Finally, the loss term for the photon density rate equation has to be evaluated. There are a number of mechanisms that can contribute to loss. These include losses due to absorption, scattering, and mirror losses. Scattering is due to nonuniformities in the material of the laser cavity and roughness at layer interfaces. Mirror losses can include scattering losses at the DBR interfaces, but also include losses due to the less than 100% reflectivity of the mirrors. Similar to the carrier lifetime used for carrier losses in the carrier density rate equation, a photon lifetime, τ_p, is used for photon losses in the laser cavity. For photon losses in the optical cavity, we use:

$$N_{p,loss} = \frac{N_p}{\tau_p} \qquad \text{Equation 6-14}$$

The final form for the photon density rate equation with the expression for R_{stim} evaluated for the carrier density rate equation is:

$$\frac{dN_p}{dt} = \Gamma v_g g N_p + \beta_{spon} \Gamma R_{spon} - \frac{N_p}{\tau_p} \qquad \text{Equation 6-15}$$

6.3 Threshold Condition

Threshold in the VCSEL occurs when the roundtrip photon gain in the device is equal to the losses in the laser. Photons are generated in the active region of the VCSEL, and propagate between the two mirrors. Gain occurs in the active layers of the VCSEL and loss occurs inside the cavity, at layer interfaces, and in the VCSEL mirrors. The loss in the cavity of the VCSEL per unit length is called the loss coefficient, α_i. We use an average value for this loss coefficient because the loss will vary as the light propagates through the various layers of the laser cavity and notate this as, $\langle \alpha_i \rangle$. We can get a better understanding of the average cavity loss coefficient by looking at its definition:

$$\langle \alpha_i \rangle = \frac{\alpha_{act} L_{act} + \alpha_{pass} L_{pass}}{L} \qquad \text{Equation 6-16}$$

where L_{act} and L_{pass} are the lengths of the active region and the passive region of the laser cavity, and α_{act} and α_{pass} are the loss coefficients of the active and passive regions of the laser cavity. Passive regions in the cavity are regions that do not produce gain. Loss mechanisms in the active region are mainly due to absorption. Losses in the passive regions can include absorption as well as scattering. For one roundtrip in the cavity, the power of the light, P_i, decreases by the factor:

$$R_t R_b \exp(-2\langle \alpha_i \rangle L) \qquad \text{Equation 6-17}$$

where R_t and R_b are the reflectivities of the top and bottom VCSEL mirrors and L is the length of the cavity.

Since gain is only exhibited in the active layers of the laser, the power of the light increases due to gain in the cavity by a factor:

$$\exp(2gL_{act}) \qquad \text{Equation 6-18}$$

After one roundtrip, the light is changed by a factor due to loss and gain in the cavity of:

$$R_t R_b \exp 2(gL_{act} - \langle \alpha \rangle_i L) \qquad \text{Equation 6-19}$$

Using Equation 6-16 this equation can be expanded to:

$$R_t R_b \exp 2(gL_a - (\alpha_{act} L_{act} + \alpha_{pass} L_{pass})) \qquad \text{Equation 6-20}$$

Threshold occurs when the loss and the gain in the cavity are equivalent after a roundtrip by the light. This condition requires that the initial power of the light be equal to its power after a round trip in the cavity:

$$P_i R_t R_b \exp 2(g_{th} L_a - (\alpha_{act} L_{act} + \alpha_{pass} L_{pass})) = P_i \qquad \text{Equation 6-21}$$

Rearranging this equation, and solving for the gain at threshold, g_{th}:

$$g_{th} = \alpha_{act} + \frac{\alpha_{pass} L_{pass}}{L_{act}} + \frac{1}{2L_{act}} \ln \frac{1}{R} \qquad \text{Equation 6-22}$$

where R represents the $R_1 R_2$ product. Multiplying this equation by L_{act}/L, we obtain:

$$g_{th} \frac{L_{act}}{L} = \frac{\alpha_{act} L_{act}}{L} + \frac{\alpha_{pass} L_{pass}}{L} + \frac{1}{2L} \ln \frac{1}{R} \qquad \text{Equation 6-23}$$

this simplifies to:

$$g_{th} \frac{L_{act}}{L} = \frac{\alpha_{act} L_{act} + \alpha_{pass} L_{pass}}{L} + \frac{1}{2L} \ln \frac{1}{R} \qquad \text{Equation 6-24}$$

The value on the left hand side of the equation is equal to the threshold gain normalized over the entire length of the cavity. We denote this normalized threshold gain as $\langle g_{th} \rangle$. The first term on the right hand side of the equation is equal to the average cavity loss coefficient as mentioned in Equation 6-16. The second term is given the notation, α_m, and is the distributed mirror loss coefficient. This term depends on the reflectivity of the VCSEL mirrors as well as the cavity length. The mirror loss coefficient is dependent on the cavity length because for a longer cavity, the light will stay in the cavity longer for one roundtrip and thus reducing the effect of the mirror loss.

The final general form of the normalized threshold gain is:

$$\langle g_{th} \rangle = \langle \alpha_i \rangle + \alpha_m \qquad \text{Equation 6-25}$$

Noting that the losses in the cavity multiplied by the group velocity is equal to the inverse of the photon lifetime, we have:

$$v_g \left(\langle \alpha_i \rangle + \alpha_m \right) = \frac{1}{\tau_p} \qquad \text{Equation 6-26}$$

6.4 Longitudinal Mode Phase Condition

In addition to the gain in the device being equal to the loss for lasing, a phase condition has to be satisfied. The phase condition requires that the propagating wave be in phase after a round trip in the cavity. This ensures that the waves will not interfere destructively. The phase condition requires that:

$$n\lambda = 2L_c \qquad \text{Equation 6-27}$$

where n is the mode number (n=1,2,3,…), λ is the wavelength of the mode in the cavity, and L_c is the cavity length. The wavelength of the mode in the cavity is dependent on refractive index and depending on the material of the cavity, the wavelength of the mode in the cavity can be written in terms of the wavelength in vacuum using the relation:

$$\lambda = \lambda_0 / n_r \qquad\qquad \text{Equation 6-28}$$

The waves that interfere constructively in the cavity become standing waves and determine the longitudinal modes that are possible for lasing.

6.5 Spontaneous Emission Operation

Spontaneous emission operation occurs below threshold for the VCSEL. It is necessary to evaluate the light power generated in this region for later analysis of light power above threshold in the VCSEL. In the spontaneous emission region below threshold, the device behaves like an LED. The spectral characteristics of the light are incoherent and the photons generated in the device receive no amplification. From the carrier density rate equation at steady-state operation,

$$\frac{dN}{dt} = 0 \qquad\qquad \text{Equation 6-29}$$

There is also no term for stimulated recombination, because the device is below threshold:

$$R_{stim} = 0 \qquad\qquad \text{Equation 6-30}$$

The carrier density rate equation for the VCSEL operating below threshold at steady state becomes:

$$\frac{\eta_i I}{qV} = R_{spon} + R_{nr} + R_l \qquad \text{Equation 6-31}$$

To obtain the power of the light below threshold, this equation is multiplied by hv and the volume of the active region in the device, V. The equation transforms to:

$$\frac{\eta_i I h\nu}{q} = P_{spon} + h\nu V(R_{nr} + R_l) \qquad \text{Equation 6-32}$$

We can then obtain an expression for P_{spon}:

$$P_{spon} = \frac{\eta_i I h\nu}{q} - h\nu V(R_{nr} + R_l) \qquad \text{Equation 6-33}$$

Rearranging the equation:

$$P_{spon} = \frac{\eta_i I h\nu}{q}\left(1 - \frac{qV(R_{nr} + R_l)}{\eta_i I}\right) \qquad \text{Equation 6-34}$$

We can now define the terms in the large parentheses as a spontaneous recombination fraction, η_{spon}. This term is more readily apparent by rearranging the terms in the large parentheses and substituting Equation 6-31 into it:

$$\eta_{spon} = \frac{R_{spon} + R_{nr} + R_l}{R_{spon} + R_{nr} + R_l} - \frac{R_{nr} + R_l}{R_{spon} + R_{nr} + R_l} \qquad \text{Equation 6-35}$$

Simplifying this equation, we can see that it is the fraction of the total non-stimulated recombination mechanisms due to spontaneous recombination:

$$\eta_{spon} = \frac{R_{spon}}{R_{spon} + R_{nr} + R_l} \qquad \text{Equation 6-36}$$

The final form of the equation for the light power of the VCSEL below threshold is:

$$P_{spon} = \eta_i \eta_{spon} \frac{h\nu}{q} I \qquad \text{Equation 6-37}$$

This equation gives the total light output power out of the diode and does not include emission losses in the device. We include a light coupling efficiency, η_c, to account for this. With the emission loss factor, we have:

$$P_{spon} = \eta_i \eta_{spon} \eta_c \frac{h\nu}{q} I \qquad \text{Equation 6-38}$$

The emission loss factor can be evaluated in detail by beginning with the photon density rate equation and evaluating in the spontaneous emission region at steady-state. From Equation 6-15:

$$0 = \Gamma \beta_{spon} R_{spon} - \frac{N_p}{\tau_p} \qquad \text{Equation 6-39}$$

Rearranging and solving for N_p, we have:

$$N_p = \Gamma \beta_{spon} R_{spon} \tau_p \qquad \text{Equation 6-40}$$

Similar to what was done earlier for expressing the equation as a light output power, we multiply by $h\nu$ and the volume of the cavity this time, because the photon density rate equation was written for photons in the laser cavity. We now also multiply the equation by a factor that accounts for mirror loss, $\nu_g \alpha_m$, which is the product of the group velocity and the mirror loss coefficient. We have:

$$P_{out} = \nu_g \alpha_m \Gamma \beta_{spon} R_{spon} \tau_p h\nu V_{cav} \qquad \text{Equation 6-41}$$

The value for $\nu_g \tau_p$ is related to the losses in the cavity and was derived in Equation 6-26. Substituting this into Equation 6-41, we have:

$$P_{out} = \left(\frac{\alpha_m}{\langle \alpha_i \rangle + \alpha_m} \right) \Gamma \beta_{spon} R_{spon} h\nu V_{cav} \qquad \text{Equation 6-42}$$

The expression for R_{spon} is obtained by dividing P_{spon} in Equation 6-37 by hvV. We obtain:

$$R_{spon} = \frac{\eta_r \eta_i I}{q V_{cav}}$$

Equation 6-43

Substituting this into equation 6-42, we have:

$$P_{out} = \left(\frac{\alpha_m}{\langle \alpha_i \rangle + \alpha_m} \right) \frac{\Gamma \beta_{spon} \eta_r \eta_i I h \nu V_{cav}}{q V_{act}}$$

Equation 6-44

Using the approximate expression for the confinement factor, $\Gamma = \frac{V_{act}}{V_{cav}}$, we obtain the final form for the light output power out for a laser operating below threshold:

$$P_{out} = \left(\frac{\alpha_m}{\langle \alpha_i \rangle + \alpha_m} \right) \frac{\beta_{spon} \eta_r \eta_i I h \nu}{q}$$

Equation 6-45

Comparing this to Equation 6-38, we have an expression for the light coupling efficiency, η_c:

$$\eta_c = \frac{\alpha_m \beta_{spon}}{\langle \alpha_i \rangle + \alpha_m}$$

Equation 6-46

6.6 Stimulated Emission Operation

For stimulated emission, we analyze the VCSEL operation above threshold. Again we begin with the carrier density rate equation and consider the device operating at right about threshold but not to the point where stimulated emission has begun. From the carrier density rate equation, we obtain just below threshold:

$$\frac{\eta_i I_{th}}{qV} = (R_{spon} + R_{nr} + R_l)_{th} = \frac{N_{th}}{\tau} \qquad \text{Equation 6-47}$$

Substituting this into the general carrier density rate equation, we can obtain an expression for operation above threshold:

$$\frac{dN}{dt} = \frac{\eta_i I}{qV} - \frac{\eta_i I_{th}}{qV} - v_g g N_p \qquad \text{Equation 6-48}$$

It is important to note that the gain and the carrier density clamp to a constant value at and above threshold. At current levels above threshold, the gain saturates and additional carriers injected into the active region recombine to form coherent light, keeping the carrier density constant at the threshold value. With these rules, an expression for the photon density, N_p, at steady state and above threshold is obtained:

$$N_p = \frac{\eta_i (I - I_{th})}{q v_g g_{th} V} \qquad \text{Equation 6-49}$$

Similar to the analysis performed for deriving the output power in the spontaneous emission region, we multiply this equation by hv and the volume occupied by photons in the device, V. The output power also needs to be multiplied by a factor that represents the loss per length through the mirrors. This loss will be equal to the product of the group velocity and the mirror loss coefficient, $v_g \alpha_m$. For the total output power through the mirrors:

$$P_0 = v_g \alpha_m N_p h \nu V \qquad \text{Equation 6-50}$$

Substituting Equations 6-25, 6-26, and 6-49 we obtain:

$$P_0 = \left(\frac{\alpha_m}{\langle \alpha_i \rangle + \alpha_m} \right) \eta_i \frac{h\nu}{q} (I - I_{th}) \qquad \text{Equation 6-51}$$

The differential quantum efficiency of the laser is:

$$\eta_d = \eta_i \left(\frac{\alpha_m}{\langle \alpha_i \rangle + \alpha_m} \right) \qquad \text{Equation 6-52}$$

and Equation 6-51 is simplified to:

$$P_0 = \eta_d \frac{h\nu}{q} (I - I_{th}) \qquad \text{Equation 6-53}$$

This equation represents the total ouput power emitted from both mirrors of the VCSEL. If the mirrors had equal reflectivities, the output power would be distributed evenly between the top and bottom mirror. If one of the mirrors were perfectly reflecting, i.e. 100% reflectivity, the equation would describe the total light output power out the other mirror. Calculating the light output power out of mirrors with different reflectivities isn't a trivial problem and is detailed in literature.[5]

To make sense of what the differential quantum efficiency is, we can take the derivative of P_0 with respect to current, I. We have:

$$\frac{dP_0}{dI} = \eta_d \frac{h\nu}{q} \qquad \text{Equation 6-54}$$

Rearranging, we have:

$$\eta_d = \frac{q}{h\nu} \frac{dP_0}{dI} \qquad \text{Equation 6-55}$$

This relation was derived for above threshold operation and shows that the differential quantum efficiency tells us how well the laser converts injected carriers into photons. Another useful parameter for characterizing lasers is the slope efficiency. This value is equal to the derivative, $\frac{dP_0}{dI}$, and is simply the slope of the L-I curve above threshold.

The slope efficiency of the LIV characteristic shown in Figure 4-1 is 0.31 mw/mA. At the 850 nm wavelength, the differential quantum efficiency can be determined using Equation 6-55. The equation for the 850 nm wavelength becomes:

$$\eta_d = 0.68 \frac{dP_0}{dI} \qquad \text{Equation 6-56}$$

The value of the differential quantum efficiency for a slope efficiency of 0.31 mW/mA is 0.21.

CHAPTER 7
FUTURE WORK AND CONCLUSIONS

The results described for the VCSEL devices of this work leave open many paths of progression on the research of VCSELs. An enormous amount of work has been done on 850 nm VCSELs to date, but there remains many areas that can be explored with these devices.

This dissertation revealed some areas of improvement for the VCSELs of this work. The series resistance analysis performed brought attention to the levels of resistance for current conduction in the radial direction. Further work can be done with the cavity design to reduce the radial current resistance, while being mindful that losses are minimized using the cavity design methods discussed.

There hasn't been any reports on the device characteristics of wire-bonded 850 nm VCSELs. It would be a valuable exercise to do this and demonstrate VCSEL operation without significant degradation in device performance. Heating analysis could be performed using the methods outlined in this dissertation for the wire bonded VCSELs. It is expected that wire bonding a VCSEL would lower its thermal resistance similar to the heat dissipation benefits realized when the VCSELs are flip-chip bonded.

Figure 7-1 shows a schematic of a flip-chip bonded VCSEL. Flip-chip bonding could be performed with the devices of this work to determine the benefits of

heat dissipation in the device and the expected improvement in the thermal resistance. Arrays of VCSELs could be flip-chip bonded as well. This is certain to add increasing complexity to bonding of the devices, but would be a very beneficial demonstration for lower thermal resistance operation in applications such as parallel data transmission.

More thorough transmission experiments can be performed using optical fiber from different manufacturers. The transmission experiments can include increasing the distance of the optical fiber over which the signal travels and determining the maximum distance that can support 10 Gb/s operation.

The technology developed for 850 nm VCSELs can be applied to developing high-performance long-wavelength VCSELs emitting at 1.3 and at 1.55 micron wavelengths. These two wavelengths are for long-haul signal transmission. The long-wavlength VCSELs will present a new set of challenges, but the progress that has been reported is very encouraging.

The possibilities seem endless for continued research on the VCSELs. These devices have come a long way from the first demonstrated devices. They are now making progress on deployment into the infrastructure of the telecommunications networks of the world. Continued research will push the limits of device performance and this in turn will improve the systems used in optical networks. But, there undoubtedly will be many challenges to come.
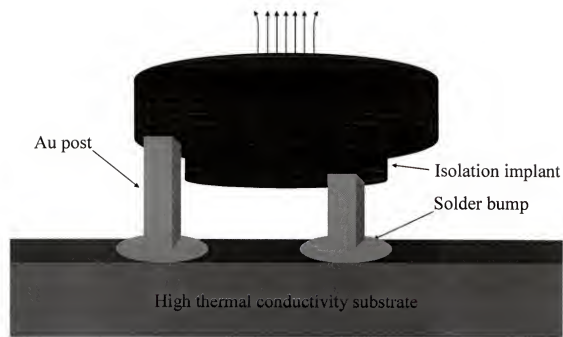
Figure 7-1 Schematic of a flip-chip bonded VCSEL.

```
Dim X As Integer, T As Integer
Dim h As Double
Dim Tinf As Double
Dim k1 As Double, k2a As Double, k2b As Double, k3 As Double, k4 As Double
Dim delz1 As Double, delz2a As Double, delz2b As Double, delz3 As Double, delz4
As Double
Dim delr1 As Double, delr2 As Double, rm1 As Double, rm2 As Double
Dim Invrmp As Double, Invrmm As Double, Invrkm As Double, Invrkp As Double
Dim Rmm As Double, Pi As Double, delphi As Double
Dim qgen As Double

Sub Radial()

Pi = 4 * Atn(1)
Tinf = 298
k1 = 0.01
k2a = 0.0146        '20 percent AlGaAs
k2b = 0.044         'GaAs quantum well
k3 = 0.01
k4 = 0.0189
h = 0.00000001
delz1 = 0.4691
delz2a = 0.01       '20 percent AlGaAs
delz2b = 0.008      'GaAs quantum well
delz3 = 0.16
delz4 = 0.1803
delr1 = 2
delr2 = 10 - delr1
delr3 = 5
rm1 = delr1 / 2
rm2 = (2 * delr1 + delr2) / 2
rm3 = ((delr1 + delr2) + (delr1 + delr2 + delr3)) / 2
delphi = 2 * Pi
qgen = 11.4 / 3
T = 23
```

```
Range("A2:U22").Clear
Range("A2:U22") = 0

kz12a = (k1 * delz1 + k2a * delz2a) / (delz1 + delz2a)
kz2a2b = (k2a * delz2a + k2b * delz2b) / (delz2a + delz2b)
kz2a3 = (k2a * delz2a + k3 * delz3) / (delz2a + delz3)
kz34 = (k3 * delz3 + k4 * delz4) / (delz3 + delz4)

Rem Node 11 surface

Invrmp = (rm1 + delr1 / 2) * delphi * delz1 * k1 / (rm2 - rm1)
Invrmm = 0
Invrkp = 0
Invrkm = rm1 * delphi * delr1 * kz12a / (delz1 / 2 + delz2a / 2)

Cells(2, 1).Value = -(Invrmp + Invrmm + Invrkp + Invrkm)
Cells(2, 10).Value = Invrmp
Cells(2, 2).Value = Invrkm
Cells(2, T).Value = -6.5

Rem Node 12 interior

Invrmp = (rm1 + delr1 / 2) * delphi * delz2a * k2a / (rm2 - rm1)
Invrkp = rm1 * delphi * delr1 * kz12a / (delz2a / 2 + delz1 / 2)
Invrkm = rm1 * delphi * delr1 * kz2a2b / (delz2a / 2 + delz2b / 2)

Cells(3, 2).Value = -(Invrmp + Invrmm + Invrkp + Invrkm)
Cells(3, 11).Value = Invrmp
Cells(3, 1).Value = Invrkp
Cells(3, 3).Value = Invrkm
Cells(3, T).Value = 0

For X = 0 To 4 Step 2

Invrmp = (rm1 + delr1 / 2) * delphi * delz2b * k2b / (rm2 - rm1)
Invrkp = rm1 * delphi * delr1 * kz2a2b / (delz2a / 2 + delz2b / 2)
Invrkm = rm1 * delphi * delr1 * kz2a2b / (delz2a / 2 + delz2b / 2)

Cells(X + 4, X + 3).Value = -(Invrmp + Invrmm + Invrkp + Invrkm)
Cells(X + 4, X + 12).Value = Invrmp
Cells(X + 4, X + 2).Value = Invrkp
Cells(X + 4, X + 4).Value = Invrkm
Cells(X + 4, T).Value = -qgen

If X = 4 Then Exit For
```

```
Invrmp = (rm1 + delr1 / 2) * delphi * delz2a * k2a / (rm2 - rm1)
Invrkp = rm1 * delphi * delr1 * kz2a2b / (delz2a / 2 + delz2b / 2)
Invrkm = rm1 * delphi * delr1 * kz2a2b / (delz2a / 2 + delz2b / 2)

Cells(X + 5, X + 4).Value = -(Invrmp + Invrmm + Invrkp + Invrkm)
Cells(X + 5, X + 13).Value = Invrmp
Cells(X + 5, X + 3).Value = Invrkp
Cells(X + 5, X + 5).Value = Invrkm
Cells(X + 5, T).Value = 0

Next X

Invrmp = (rm1 + delr1 / 2) * delphi * delz2a * k2a / (rm2 - rm1)
Invrkp = rm1 * delphi * delr1 * kz2a2b / (delz2a / 2 + delz2b / 2)
Invrkm = rm1 * delphi * delr1 * kz2a3 / (delz2a / 2 + delz3 / 2)

Cells(9, 8).Value = -(Invrmp + Invrmm + Invrkp + Invrkm)
Cells(9, 17).Value = Invrmp
Cells(9, 7).Value = Invrkp
Cells(9, 9).Value = Invrkm
Cells(9, T).Value = 0

Rem Node 13 surface

Invrmp = (rm1 + delr1 / 2) * delphi * delz3 * k3 / (rm2 - rm1)
Invrkp = rm1 * delphi * delr1 * kz2a3 / (delz3 / 2 + delz2a / 2)
Invrkm = rm1 * delphi * delr1 * kz34 / (delz3 / 2 + delz4 / 2)

Cells(10, 9).Value = -(Invrmp + Invrmm + Invrkp + Invrkm)
Cells(10, 19).Value = Invrmp
Cells(10, 8).Value = Invrkp
Cells(10, 10).Value = Invrkm
Cells(10, T).Value = 0

Rem Node 14

Invrmp = (rm1 + delr1 / 2) * delphi * delz4 * k4 / (rm2 - rm1)
Invrmm = 0
Invrkp = rm1 * delphi * delr1 * kz34 / (delz3 / 2 + delz4 / 2)
Invrkm = rm1 * delphi * delr1 * k4 / (delz4 / 2)

Cells(11, 10).Value = -(Invrmp + Invrmm + Invrkp + Invrkm)
Cells(11, 20).Value = Invrmp
Cells(11, 9).Value = Invrkp
Cells(11, T).Value = -Tinf * Invrkm
```

```
Rem Node 21 surface

Invrmp = h * delphi * (delr1 + delr2) * delz1
Invrmm = (rm2 - delr2 / 2) * delphi * delz1 * k1 / (rm2 - rm1)
Invrkp = 0
Invrkm = rm2 * delphi * delr2 * kz12a / (delz1 / 2 + delz2a / 2)

Cells(12, 11).Value = -(Invrmp + Invrmm + Invrkp + Invrkm)
Cells(12, 1).Value = Invrmm
Cells(12, 12).Value = Invrkm
Cells(12, T).Value = -Tinf * (Invrmp) - 6.6

Rem Node 22 interior

Invrmp = h * delphi * (delr1 + delr2) * delz2a
Invrmm = (rm2 - delr2 / 2) * delphi * delz2a * k2a / (rm2 - rm1)
Invrkp = rm2 * delphi * delr2 * kz12a / (delz2a / 2 + delz1 / 2)
Invrkm = rm2 * delphi * delr2 * kz2a2b / (delz2a / 2 + delz2b / 2)

Cells(13, 12).Value = -(Invrmp + Invrmm + Invrkp + Invrkm)
Cells(13, 2).Value = Invrmm
Cells(13, 11).Value = Invrkp
Cells(13, 13).Value = Invrkm
Cells(13, T).Value = -Tinf * (Invrmp)

For X = 0 To 4 Step 2

Invrmp = h * delphi * (delr1 + delr2) * delz2b
Invrmm = (rm2 - delr2 / 2) * delphi * delz2b * k2b / (rm2 - rm1)
Invrkp = rm2 * delphi * delr2 * kz2a2b / (delz2b / 2 + delz2a / 2)
Invrkm = rm2 * delphi * delr2 * kz2a2b / (delz2b / 2 + delz2a / 2)

Cells(X + 14, X + 13).Value = -(Invrmp + Invrmm + Invrkp + Invrkm)
Cells(X + 14, X + 3).Value = Invrmm
Cells(X + 14, X + 12).Value = Invrkp
Cells(X + 14, X + 14).Value = Invrkm
Cells(X + 14, T).Value = -Tinf * (Invrmp)

If X = 4 Then Exit For

Invrmp = h * delphi * (delr1 + delr2) * delz2a
Invrmm = (rm2 - delr2 / 2) * delphi * delz2a * k2a / (rm2 - rm1)
Invrkp = rm2 * delphi * delr2 * kz2a2b / (delz2a / 2 + delz2b / 2)
Invrkm = rm2 * delphi * delr2 * kz2a2b / (delz2a / 2 + delz2b / 2)

Cells(X + 15, X + 14).Value = -(Invrmp + Invrmm + Invrkp + Invrkm)
```

```
Cells(X + 15, X + 4).Value = Invrmm
Cells(X + 15, X + 13).Value = Invrkp
Cells(X + 15, X + 15).Value = Invrkm
Cells(X + 15, T).Value = -Tinf * (Invrmp)

Next X

Invrmp = h * delphi * (delr1 + delr2) * delz2a
Invrmm = (rm2 - delr2 / 2) * delphi * delz2a * k2a / (rm2 - rm1)
Invrkp = rm2 * delphi * delr2 * kz2a2b / (delz2a / 2 + delz2a / 2)
Invrkm = rm2 * delphi * delr2 * kz2a3 / (delz2a / 2 + delz3 / 2)

Cells(19, 18).Value = -(Invrmp + Invrmm + Invrkp + Invrkm)
Cells(19, 8).Value = Invrmm
Cells(19, 17).Value = Invrkp
Cells(19, 19).Value = Invrkm
Cells(19, T).Value = -Tinf * (Invrmp)

Rem Node 23 surface

Invrmp = h * delphi * (delr1 + delr2) * delz3
Invrmm = (rm2 - delr2 / 2) * delphi * delz3 * k3 / (rm2 - rm1)
Invrkp = rm2 * delphi * delr2 * kz2a3 / (delz2a / 2 + delz3 / 2)
Invrkm = rm2 * delphi * delr2 * kz34 / (delz3 / 2 + delz4 / 2)

Cells(20, 19).Value = -(Invrmp + Invrmm + Invrkp + Invrkm)
Cells(20, 9).Value = Invrmm
Cells(20, 18).Value = Invrkp
Cells(20, 20).Value = Invrkm
Cells(20, T).Value = -Tinf * (Invrmp) - 3.25

Rem Node 24 surface

Invrmp = (rm2 + delr2 / 2) * delphi * delz4 * k4 / (rm3 - rm2)
Invrmm = (rm2 - delr2 / 2) * delphi * delz4 * k4 / (rm2 - rm1)
Invrkp = rm2 * delphi * delr2 * kz34 / (delz3 / 2 + delz4 / 2)
Invrkm = rm2 * delphi * delr2 * k4 / (delz4 / 2)

Cells(21, 20).Value = -(Invrmp + Invrmm + Invrkp + Invrkm)
Cells(21, 21).Value = Invrmp
Cells(21, 10).Value = Invrmm
Cells(21, 19).Value = Invrkp
Cells(21, T).Value = -Tinf * (Invrkm) - 3.25

Rem Node 34
```

```
Invrmp = (rm3 + delr3 / 4) * delphi * delz4 * k4 / (delr3 / 2)
Invrmm = (rm3 - delr3 / 2) * delphi * delz4 * k4 / (rm3 - rm2)
Invrkp = h * Pi * ((delr1 + delr2 + delr3) ^ 2 - (delr1 + delr2) ^ 2)
Invrkm = rm3 * delphi * delr3 * k4 / (delz4 / 2)

Cells(22, 21).Value = -(Invrmp + Invrmm + Invrkp + Invrkm)
Cells(22, 20).Value = Invrmm
Cells(22, T).Value = -Tinf * (Invrmp + Invrkp + Invrkm) - 10.8

End Sub
```

REFERENCES

[1] H. Soda, K. Iga, C. Kitahara, and Y. Suematsu, "GaInAsP/InP Surface Emitting Injection Lasers," Japn. J. Appl. Phys., vol. 18, no. 12, pp. 2329-2330, 1979.

[2] K. Iga, F. Koyama, S. Kinoshita, "Surface Emitting Semiconductor Lasers," IEEE Journ. of Quant. Electron., vol. 24, no. 9, pp. 1845-1855, 1988.

[3] F. Koyama, H. Uenohara, T. Sakaguchi, and K. Iga, "GaAlAs/GaAs MOCVD Growth for Surface Emitting Laser," Japn. J. Appl. Phys., vol. 26, no. 7, pp. 1077-1081, 1987.

[4] F. Koyama, S. Kinoshita, K. Iga, "Room-Temperature Continuous Wave Lasing Characteristics of a GaAs Vertical Cavity Surface-Emitting Laser," Appl. Phys. Lett., vol. 55, no. 3, 1989.

[5] A.V. Krishnamoorthy, K.W. Goossen, L.M.F. Chirovsky, R.G. Rozier, P. Chandramani, W.S. Hobson, S.P. Hui, J. Lopata, J.A. Walker, and L.A. D'Asaro, "16x16 VCSEL Array Flip-Chip Bonded to CMOS VLSI Circuit," Technical Digest, OSA Topical Meeting On Optics in Computing, Post Deadline paper, March 1999.

[6] E. Palik, Handbook of Optical Constants of Solids, Academic Press, San Diego, 1998.

[7] G. Fabry and A. Perot, Ann. Chim. Phys., vol. 16, p. 115, 1899.

[8] L.M.F. Chirovsky, W.S. Hobson, R.E. Leibenguth, S.P. Hui, J. Lopata, G.J. Zydzik, G. Giaretta, K.W. Goossen, J.D. Wynn, A.V. Krishnamoorthy, B.J. Tseng, J.M. Vandenberg, and L.A. D'Asaro, "Implant-Apertured and Index-Guided Vertical-Cavity Surface-Emitting Lasers (I^2-VCSELs)," IEEE Photon. Tech. Lett. vol. 11, no. 5, pp. 500-502, 1999.

[9] A.V. Krishnamoorthy, L.M.F. Chirovsky, W.S. Hobson, J. Lopata, J. Shah, R. Rozier, J.E. Cunningham, and L.A. D'Asaro, "Small-Signal Characteristics of Bottom-Emitting Intracavity Contacted VCSEL's," IEEE Photon. Tech. Lett. vol. 12, no. 6, pp. 609-611, 2000.

[10] L. Coldren and E.R. Hegblom, "Fundamental Issues in VCSEL Design," in Vertical-Cavity Surface-Emitting Lasers, C. Wilmsen, H. Temkin, L. Coldren (editors), Cambridge University Press, New York, 1999.

[11] M. Born and E. Wolf, Principles of Optics, 5th edition, Pergamon Press, New York, 1975.

[12] L.A. Coldren, "Lasers and Modulators for OEICs", in Integrated Optoelectronics, M. Dagenais, R.F. Leheny, and J. Crow (editors), Academic Press, New York, 1994.

[13] A. Yariv, Quantum Electronics, 3rd edition, Wiley, New York, 1989.

[14] K. Tai, L. Yang, Y.H. Wang, J.D. Wynn, and A.Y. Cho, "Drastic Reduction of Series Resistance in Doped Semiconductor Distributed Bragg Reflectors for Surface-Emitting Lasers," Appl. Phys. Lett., vol. 56, no. 25, pp. 2496-2498, 1990.

[15] M. Hong, J.P. Mannaerts, J.M. Hong, R.J. Fischer, K. Tai, J. Kwo, J.M. Vanderberg, Y.H. Wang, and J. Gamelin, "A Simple Way to Reduce Series Resistance in p-Doped Semiconductor Distributed Bragg Reflectors," Journ. Crystal Growth, vol. 111, pp. 1071-1075, 1991.

[16] S.A. Chalmers, K.L. Lear, and K.P. Killeen, "Low Resistance Wavelength-Reproducible p-Type (Al,Ga)As Distributed Bragg Reflectors Grown by Molecular Beam Epitaxy," Appl. Phys. Lett., vol. 62, no. 14, pp. 1585-1587, 1993.

[17] R.P. Schneider, Jr., J.A. Lott, K.L. Lear, K.D. Choquette, M.H. Crawford, S.P. Kilcoyne, and J.J. Figiel, "Metalorganic Vapor Phase Epitaxial Growth of Red and Infrared Vertical-Cavity Surface-Emitting Lasers," Journ. Crystal Growth, vol. 145, pp. 838-845, 1994.

[18] K.L. Lear and R.P. Schneider, Jr., "Uniparabolic Mirror Grading for Vertical Cavity Surface-Emitting Lasers," Appl. Phys. Lett., vol. 68, no. 5, pp. 605-607, 1996.

[19] K.D. Choquette, R.P. Schneider, Jr., K.L. Lear, K.M. Geib, "Low Threshold Voltage Vertical-Cavity Lasers Fabricated by Selective Oxidation," Electron. Lett., vol. 30, no. 24, pp. 2043-2044, 1994.

[20] M. Webster, R.V. Penty, I.H. White, M.R.T. Tan, S.W. Corzine, "Performance of 10 Gbit/s VCSELs Operating at 85 ℃" Conference on Lasers and Electro-Optics, 2000 (CLEO 2000), pp. 201 -202, 2000.

[21] F. Mederer, M. Grabherr, F. Eberhard, I. Ecker, R. Jager, J. Joos, C. Jung, M. Kicherer, R. King, P. Schnitzer, H. Unold, D. Wiedenmann, K.J. Ebeling, "High Performance Selectively Oxidized VCSELs and Arrays for Parallel High-Speed Optical Interconnects," Electronic Components & Technology Conference, 2000. 2000 Proceedings. 50th, pp. 1242 -1251, 2000.

[22] M. Kicherer, R. Jager, R. King, F. Mederer, H.J. Unold, K.J. Ebeling, "Single- and Multi-Mode VCSELs for 12.5 Gb/s Data Links," Conference on Lasers and Electro-Optics Europe, 2000. Conference Digest, p. 1, 2000.

[23] Proceedings of the 3rd International IEEE VLSI Multilevel Interconnection Conference, June 9-10, Santa Clara, CA 1986.

[24] W. Jiang, C. Gaw, P. Kiely, B. Lawrence, M. Lebby, and P. R. Claisse, "Effect of Proton Implantation on the Degradation of GaAs/AlGaAs Vertical Cavity Surface Emitting Lasers," Electron. Lett., vol. 33, no. 2, pp. 137-139, 1997.

[25] G. H. Olsen and M. Ettenberg, "Universal Stain/Etchant for Interfaces in III-V Compound," J. Appl. Phys., vol. 45, no. 11, pp. 5112-5114, 1974.

[26] P. M. Petroff, "Device Degradation and Recombination Enhanced Defect Processes in III-V Semiconductors," Semiconductors and Insulators, vol. 5, no. 307, 1983.

[27] S. Adachi, "GaAs, AlAs, $Al_xGa_{1-x}As$: Material Parameters for use in Research and Device Applications," J. Appl. Phys., vol. 58, no. 3, pp. R1-R29,1985.

[28] The Stopping and Range of Ions in Matter, Manual, version 96.xx.

[29] T.R. Chen, B. Zhao, L. Eng, Y.H. Yuang, J. O'Brien, and A. Yariv, "Very High Modulation Efficiency of Ultralow Threshold Current Single Quantum Well InGaAs Lasers," Electron. Lett., vol. 29, no. 17, pp. 1525-1526, 1993.

[30] R. Pu, C.W. Wilmsen, K.M. Geib, and K.D. Choquette, "Thermal Resistance of VCSEL's Bonded to Integrated Circuits," IEEE Photon. Tech. Lett., vol. 11, no. 12, pp. 1554-1556, 1999.

[31] L.A. Coldren and S.W. Corzine, Diode Lasers and Photonic Integrated Circuits, section 2.8.3, John Wiley & Sons, Inc., New York, 1995.

[32] T. Kobayashi and Yoshitaka Furukawa "Temperature Distributions in the GaAs-AlGaAs Double-Heterostructure Laser Below and Above the Threshold Current," Japn. J. Appl. Phys., vol. 14, no. 12, pp. 1981-1986, 1975.

[33] J.P. Holman, Heat Transfer, 8th edition, McGraw Hill, Inc., New York,1997.

[34] L.A. Coldren and S.W. Corzine, Diode Lasers and Photonic Integrated Circuits, John Wiley & Sons, Inc., New York, 1995.

BIOGRAPHICAL SKETCH

Gerard Tu Dang was born November 10th, 1975, and was the first Vietnamese boy born in the city of Ripon, CA. He is the son of refugees from Vietnam. His parents fled Vietnam in 1975 while pregnant with Gerard. Gerard was named after Gerard Fondse of Ripon, CA. Gerard and Betty Fondse were the sponsors for the Dang family when they immigrated to the United States.

Gerard grew up in Stockton, CA. He graduated high school in Stockton, spring of 1993. That fall, he relocated to Los Angeles to attend the University of California, at Los Angeles. He graduated from UCLA in March of 1998 with a B.S. in chemical engineering. During the final two years of his undergraduate studies, Gerard became deeply interested in the semiconductor industry. This developing interest was strongly influenced by his uncle, Manh An, an engineer with Intel Corporation. Gerard had tailored his undergraduate coursework as much as he could to prepare him for entering a career as a chemical engineer in the semiconductor field after graduation, but decided instead on furthering his education in a research environment and specializing in an emerging technology of semiconductor devices. Gerard enrolled in graduate school at the University of Florida, Department of Chemical Engineering in fall 1998, where he joined Professor Fan Ren's research group to work on state of the art compound semiconductor devices.

He has designed, fabricated, and characterized an assortment of III-V based devices including GaN based electronic devices, such as hi-power rectifiers, HEMTs, HBTs and GaAs quantum-well 850 nm vertical-cavity surface-emitting lasers.

I certify that I have read this study and that in my opinion it conforms to acceptable standards of scholarly presentation and is fully adequate, in scope and quality, as a dissertation for the degree of Doctor of Philosophy.
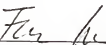
Fan Ren, Committee Chairman
Professor of Chemical Engineering

I certify that I have read this study and that in my opinion it conforms to acceptable standards of scholarly presentation and is fully adequate, in scope and quality, as a dissertation for the degree of Doctor of Philosophy.
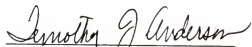
Timothy J. Anderson
Professor of Chemical Engineering

I certify that I have read this study and that in my opinion it conforms to acceptable standards of scholarly presentation and is fully adequate, in scope and quality, as a dissertation for the degree of Doctor of Philosophy.

Stephen J. Pearton
Professor of Materials Science and Engineering

I certify that I have read this study and that in my opinion it conforms to acceptable standards of scholarly presentation and is fully adequate, in scope and quality, as a dissertation for the degree of Doctor of Philosophy.
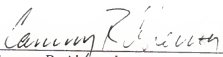
Cammy R. Abernathy
Professor of Materials Science and Engineering

This dissertation was submitted to the Graduate Faculty of the College of Engineering and to the Graduate School and was accepted as partial fulfillment of the requirements for the degree of Doctor of Philosophy.

December 2001
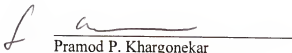
Pramod P. Khargonekar
Dean, College of Engineering
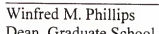
Winfred M. Phillips
Dean, Graduate School